Electronic and Structural Properties of Adsorbates on Nickel and Aluminium Surfaces

Andrew Bryan Hayden

A thesis submitted for admission to the degree of

Doctor of Philosophy.

Department of Physics

University of Warwick

8th July 1993

BEST COPY
AVAILABLE

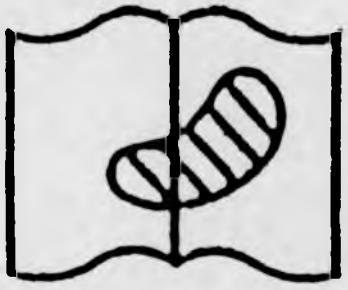

Abstract

The techniques of photoemission spectroscopy and normal incidence standing X-ray waves have been used to study the alkali-metal promoted oxidation of Al(111) and the adsorption site of methoxy on Al(111) respectively. The technique of k-resolved inverse photoemission spectroscopy has also been used to investigate the Ni(100) surface and the C, N, and O half-monolayer adsorption structures on Ni(100). The techniques of low energy electron diffraction and Auger electron spectroscopy were used in all the studies. An account of the theory for all these techniques is given before presenting and discussing the experimental results.

The Ni(100) surface has been investigated using k-resolved inverse photoemission spectroscopy (KRIPES) at two isochromat energies ($\hbar\omega$ = 10 and 11.5eV) prior to studying the C, N and O half-monolayer adsorption structures. The results from the clean Ni(100) surface are broadly compatible with previously reported studies, although no evidence for the previously reported surface resonance feature is observed. Both C and N induce a (2 × 2) $p4g$ 'clock' reconstruction of the Ni(100) surface, as opposed to the $c(2 \times 2)$ overlayer structure formed by a half-monolayer of O. KRIPES results for the C and N-induced reconstructions of Ni(100) show new adsorbate states that show little energy dispersion with the component of momentum parallel to the surface; this represents the first such study of this surface. The O adsorbate structure study shows evidence for an oxygen induced antibonding state that has a dispersion similar to that observed for the bulk s-p band. The adsorbate-induced states are assigned to an interaction of the adsorbate p states with the Ni d-band for C and N, and to an interaction between the adsorbate p-states and the Ni s-p band for O.

Photoemission measurements of the Al and Na 2p states using synchrotron radiation have been used to investigate the influence of preadsorbed sodium on the early stages of oxidation of Al(111). There is a strong promotion of the rate of oxygen dissociation and formation of the three-dimensional oxide induced by the presence of sodium. For the Al(111)($\sqrt{3} \times \sqrt{3}$)$R30°$-Na phase (corresponding to θ_{Na} = 0.33ML), the Al 2p chemically shifted states characteristic of the chemisorption precursor to oxidation seen on the Na-free surface are no longer observed. However, in the Na 2p spectra obtained at lower Na predoses and lower oxygen exposures, an intermediate chemically shifted peak is observed and this appears to characterise a new oxidation precursor.

Finally, normal incidence standing X-ray waves have been used to investigate the adsorption site of the methoxy (CH_3O-) species on Al(111) using synchrotron radiation. The X-ray absorption in the O atom of this species was recorded at both the (111) and ($\bar{1}$11) normal incidence Bragg scattering conditions (at normal and 70.5° incidence to the surface). The species was found to adsorb in a three-fold symmetric hollow site with an O-Al layer spacing of 0.70 ± 0.10Å, (as found for chemisorbed oxygen), but the site occupied is the 'hcp' hollow directly above an Al atom in the second layer, and not the 'fcc' hollow directly above an Al atom in the third layer which is occupied by chemisorbed oxygen. This clear preference for the hcp hollow site on Al(111) appears to be the first example for an adsorbate on an otherwise clean fcc(111) surface.

Contents.

1 Introduction **1**

1.1 Introduction 2

1.2 Aims of this thesis 5

1.3 Thesis layout 7

2 Supporting experimental techniques **10**

2.1 Auger electron spectroscopy (AES) 11

2.2 Low energy electron diffraction, LEED 16

2.3 Synchrotron radiation 22

2.3.1 Introduction 22

2.3.2 Basic theory 24

2.3.3 Daresbury synchrotron radiation source 25

2.3.4 Beam line 6.1 : Core-level photoemission 28

2.3.5 Beam line 6.3 28

3 k-Resolved Inverse Photoemission Spectroscopy (KRIPES) **34**

3.1 Theory 36

3.1.1 Complementary nature of photoemission and inverse photoemission 36

3.1.2 The inverse photoemission process 39

3.1.3 Bulk states and band mapping 45

3.1.4 Surface states 56

3.1.5 Discrimination of bulk and surface features 63

3.2 KRIPES experimental system 65
3.2.1 UHV 65
3.2.2 KRIPES chamber geometry 66
3.2.3 Sample mounting, manipulation and cleaning processes . . 72
3.2.4 Magnetic field cancellation 74
3.2.5 General analytical techniques 74
3.2.6 KRIPES electron gun specifications 75
3.2.7 Isochromat detector instrumentation 85

4 k-Resolved Inverse Photoemission Study of Half-Monolayer Structures of O, C and N on Ni(100) 95

4.1 Introduction 96
4.2 Experimental details 104
4.3 Clean Ni(100) : discussion of results 107
4.4 Ni(100)(2 × 2)-C : discussion of results 120
4.5 Ni(100)(2 × 2)-N : discussion of results 125
4.6 Ni(100)c(2 × 2)-O : discussion of results 130
4.7 Discussion and conclusions 137

5 Core-level photoemission study on the sodium-promoted oxidation of Al(111) 147

5.1 Introduction 149
5.2 Theory 151
5.2.1 Background 151

5.2.2 Core level photoemission 154
5.2.3 Chemical shifts of core-levels 158
5.2.4 Energy Reference level 159
5.3 Sodium-promoted oxidation of Al(111) studied by core- level photoemission. 160
5.3.1 Previous Work 160
5.3.2 Experimental system 163
5.3.3 Experimental Results 164
5.3.4 Discussion 183
5.3.5 Conclusions 185

6 Normal incidence standing X-ray wave (NISXW) study of Methoxy on Al(111) 192

6.1 Introduction 194
6.2 Theory 197
6.2.1 Variation of incidence angle 198
6.2.2 Energy variation 200
6.3 NISXW analysis 200
6.3.1 Method of Triangulation 205
6.4 NISXW Study of Methoxy on Al(111) 207
6.4.1 Introduction 207
6.4.2 Experimental considerations 208
6.4.3 Experimental results 210
6.4.4 Oxygen atom location by triangulation 219

6.4.5 Discussion 222

6.4.6 Conclusions 227

7 Summary and conclusions **233**

Acknowledgements

Firstly, I would like to take this opportunity to thank my supervisor, Professor D.P.Woodruff for providing the possibility for me to be engaged in this project, and for his help and advice throughout the course of this work and in the preparation of this thesis.

The Science and Engineering Research Council (SERC) for providing time on the Synchrotron Radiation Source (SRS) at Daresbury Laboratory and for the financial support of this work. Vacuum Science Workshop (VSW) are also thanked for the provision of a CASE studentship.

Special thanks is given to Dr.P.Pervan for sharing his knowledge and enthusiasm during this work and for supplying the tennis rackets.

Thanks is also given to Mr.P.Thompson and Mr.R.Johnston for their technical support, and to Mr.P.Pedrick and Mr.A.Lovejoy in the Electronic workshop at Warwick University.

I would also like to acknowledge Dr.C.F.McConville, Dr.J.Robinson, Dr.R.G.-Jones and Dr.M.Kerkar for their help and collaboration with some of the work presented in this thesis (see Declaration).

Thanks are also due to:

The group in Warwick for their moral ('have you finished yet?') and technical support, and also for waiting so long for the next Falkland Arms trip.

Alan Taylor for amongst other things a bottle of whisky.

Chris and Giles for trying against all odds to get me training again.

Very special thanks to Sarah Edkins for her great patience and support, and for putting up with me during the writing of this thesis.

Finally I would like to dedicate this thesis to my parents for their support and encouragement throughout my education.

Declaration

The work contained in this thesis is my own, although that part of the work which led to the publications listed below did involve collaboration with others as indicated by the author lists. It was performed jointly in the Department of Physics at the University of Warwick and at the Science and Engineering Research Council's Daresbury Laboratory during the period October 1989 to February 1993. No part of this work has previously been submitted to this or any other academic institution for admission to a higher degree.

Publications arising from the collaborative parts of this work (as described in Chapters 5 and 6) are as follows:

C.F.McConville, A.B.Hayden, J.Robinson and D.P.Woodruff, **J. Phys.: Condens. Matter 5, p1-10 (1993)**

M.Kerkar, A.B.Hayden, D.P.Woodruff, M.Kadodwala and R.G.Jones, **J. Phys.: Condens. Matter 4, p5043 (1992)**

The work in Chapter 4 has been accepted for presentation at ECOSS 13, Warwick 1993. The work in Chapter 5 has been presented at CMMP 91, Birmingham 1991.

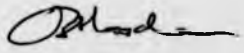

A.B.Hayden.

Chapter 1

Introduction

Contents

1 Introduction **1**

1.1 Introduction 2

1.2 Aims of this thesis 5

1.3 Thesis layout 7

1.1 Introduction

If one looks through history texts and encyclopedias, there is plenty of evidence for the observation and study of surface related phenomena in ancient times. However, only in the last 30 years has there been a rapid expansion in the quantity of work applied to studies of the properties of surfaces. In order to understand the importance of surfaces it helps first of all to define the term *surface*, which the Chambers dictionary cites as meaning *the outer boundary or face of anything.* This implies a very wide field of study with surfaces influencing and partaking in a diversity of events that surround us and which are often taken for granted.

Recent interest in surfaces has developed from an increased need to understand surface processes in technological fields such as materials science, semi-

conductor device physics and heterogenous catalysis. The surface of a solid is generally viewed as comprising the top few atomic layers of a solid, which due to the reduced two-dimensional periodicity have properties that differ from those of the relatively better understood bulk solid. Furthermore, the expansion of surface science has been greatly facilitated by the development of ultra-high vacuum (UHV) technology mainly as a result of the space program; a UHV environment with a pressure less than $10^{-9} torr$ is essential to keep a surface free from contamination by impinging gas molecules for the time taken to conduct an experiment ($1 torr = 1.33 mbar = 133 Pa$).

Surface science has many techniques (sometimes confusing with their great number of abbreviations) which are applied to probe the chemical, structural and electronic properties of the surface; but before introducing the techniques relevant to this study, it is necessary to first mention the sample itself.

To understand any problem on a large and complex scale it is desirable to investigate it first of all on a much smaller and simpler scale. For this reason most surface science is applied to low index single crystal surfaces – the 'ideal' surfaces. By determining the properties of the clean crystal surface and observing the effects of physisorption and chemisorption on those properties, it may then be possible to apply that knowledge in understanding the more complex processes that occur on real surfaces; for example, in industry where reactions are often controlled by expensive catalysts based on elements such as platinum, it is clear that resources and money can be saved if alternative or more efficient catalysts can be developed.

Prior to utilising one of the many techniques to study the surface properties, the surface must be cleaned whilst in the vacuum. This is normally achieved by bombarding the surface with argon ions to remove the top few atomic layers (leaving a disordered surface) and then annealing the crystal to re-order the surface structure. Once clean, the long range periodicity of the crystal surface can be determined by low energy electron diffraction (LEED) which is one of the oldest and most widely used surface characterisation techniques. The technique of Auger electron spectroscopy (AES) is used to establish the chemical composition of the surface, and is also used alongside LEED in characterising a surface following adsorption.

With LEED, the other main structural technique applied in this thesis is normal incidence standing X-ray waves (NISXW), which is used here to determine the adsorption site of methoxy on the Al(111) surface. Other methods of obtaining structural information mentioned in this thesis are surface-extended X-ray absorption fine structure (SEXAFS), near-edge XAFS (NEXAFS), scanning tunnelling microscopy (STM) and photoelectron diffraction (PhD).

To study the electronic structure of the surface, techniques can be divided into those investigating the occupied states and those investigating the unoccupied states. Perhaps the most widely used technique for the investigation of the occupied states is that of photoemission spectroscopy (PES). It is used as a probe of core levels (as in X-ray photoemission spectroscopy (XPS)), valence levels (ultraviolet photoemission spectroscopy (UPS)), and as a probe of the band structure (angle-resolved photoemission spectroscopy (ARUPS)). Originally a distinction

was made between UPS and XPS due to the limitations in photon energy of early laboratory sources. This has recently been made superfluous by the introduction of synchrotron radiation sources [1, 2].

For a complete understanding of the electronic structure, the unoccupied structure above the Fermi level also has to be probed. This information is obtained by employing the technique of inverse photoemission spectroscopy (IPES) which is very simply the reverse of the photoemission process. If the electron incidence angle (i.e. momentum) is well defined, then the dispersion of the unoccupied states can be obtained in a similar way to the use of the ARUPS technique for the occupied states – this technique is known as k-resolved inverse photoemission spectroscopy (KRIPES).

Since the structural and electronic properties of a surface are interdependent, there is a need to combine several techniques together with theoretical models, in order to fully understand the surface mechanisms. Good reviews on the surface science techniques used or mentioned in this thesis can be found in references [3]-[8]

1.2 Aims of this thesis

(1) To use k-resolved inverse photoemission to investigate the clean Ni(100) surface and then the half-monolayer coverage adsorption structures of C, N and O on Ni(100). Carbon and nitrogen are known to behave very differently from oxygen when adsorbed on Ni(100), the former causing a (2×2) $(p4g)$ 'clock' reconstruction of the surface and the latter forming a simple $c(2 \times 2)$ overlayer structure.

The clean Ni(100) surface and the oxygen adsorption phase have been previously studied using KRIPES at a photon energy of $9.7eV$, with no prior KRIPES study for the carbon and nitrogen phases. For all three adsorption systems the antibonding states above the Fermi level and their energy dispersion with change in wavevector parallel to the surface are probed using KRIPES, in order to determine better the bonding mechanisms involved and give some 'fingerprint' as to why the different surface reconstructions occur. For the oxygen adsorption structure in particular, it has been postulated that the oxygen induced antibonding state previously observed on the (111) and (110) nickel surfaces appears at the same energy as a direct transition between bulk states on the (100) surface at the $9.7eV$ isochromat energy (used in previous studies) [8]. The Ni(100)$c(2 \times 2)$-O system is investigated using the KRIPES technique at higher isochromat energies with the aim of observing the oxygen-induced antibonding state.

(2) To investigate the alkali-promoted oxidation of Al(111) using the technique of core-level photoemission from the Al(2p) and Na(2p) levels at varying sodium and oxygen coverages. The oxidation of Al(111) is known to involve several intermediate chemical shifts of the Al(2p) state prior to multilayer oxide formation, which are explained as precursors to the final oxidation. By repeating a previous study on the oxidation of Al(111), but with various predoses of sodium (a well known oxidation promoter), new information has been obtained concerning the promoting influence of the sodium together with the nucleation of the oxide itself.

(3) To determine the adsorption site of the methoxy species on Al(111) using the technique of normal incidence X-ray standing waves (NISXW) from the (111)

and ($\bar{1}11$) normal incidence Bragg conditions and employing real space triangulation.

1.3 Thesis layout

Each chapter in this thesis describes different techniques and presents studies discussed in the light of previous work. For convenience the references cited in each chapter are collected together at the end of each chapter, although this does lead to some repetition.

Chapter 2 provides a brief description of the LEED and AES techniques together with an introduction to synchrotron radiation and the Daresbury Synchrotron Radiation Source (SRS) which has been used for the photoemission and NISXW studies in Chapters 5 and 6.

Chapter 3 describes KRIPES theory and several models in use to predict the existence and dispersion of surface and bulk states. This chapter also details the KRIPES experimental system at Warwick University, and the KRIPES experimental technique. Chapter 4 then presents the results of a KRIPES investigation of clean Ni(100) and of the C, N and O half-monolayer structures on Ni(100). These results are discussed in relation to the different structural behaviour of the three adsorption systems previously observed using other techniques.

Chapter 5 presents a core-level photoemission study of the sodium promoted oxidation of Al(111), first introducing the theory behind the technique, then the photoemission results, and finally discussing these results with reference to recently reported information regarding this system and other similar adsorption

systems.

Chapter 6 presents the theory and experimental technique of the normal incidence standing X-ray wave process (NISXW) before describing a NISXW study to determine the adsorption site of methoxy on the Al(111) surface using geometrical triangulation. The determined adsorption site is discussed with reference to the oxygen adsorption site on Al(111), and to other related systems.

The main conclusions from this thesis are summarised in chapter 7 together with some final comments and a discussion of possible experiments arising from this work.

References

[1] *Synchrotron Radiation Research* Eds. H.Winick and S.Doniach (Plenum Press, New York. 1980)

[2] *Handbook on Sychrotron Radiation* Eds. G.S.Brown and D.E.Moncton (North-Holland, Amsterdam. 1991)

[3] J.F.O'Hanlon, *A User's Guide to Vacuum Technology* (John Wiley and sons, New York. 1989)

[4] D.P.Woodruff and T.A.Delchar, *Modern techniques of surface science* (Cambridge University Press, Cambridge. 1986)

[5] A.Zangwill, *Physics At Surfaces* (Cambridge University Press, Cambridge. 1988)

[6] *Emission and Scattering Techniques* Ed. P.Day, (D.Reidel Publishing Company, Dordrecht: Holland. 1980)

[7] *The Chemical Physics of Solid Surfaces and Heterogenous Catalysis* series, Volumes 1–6. Eds. D.A.King and D.P.Woodruff, (Elselvier, Amsterdam.)

[8] N.V.Smith and D.P.Woodruff, Progress in Surf. Sci. **21**(4), p295-370 (1986)

Chapter 2

Supporting experimental techniques

Contents

2 Supporting experimental techniques **10**

2.1 Auger electron spectroscopy (AES) 11

2.2 Low energy electron diffraction, LEED 16

2.3 Synchrotron radiation 22

2.3.1 Introduction 22

2.3.2 Basic theory 24

2.3.3 Daresbury synchrotron radiation source 25

2.3.4 Beam line 6.1 : Core-level photoemission 28

2.3.5 Beam line 6.3 28

2.1 Auger electron spectroscopy (AES)

During an experiment in which X-rays were used to ionise inert gas atoms in a Wilson cloud chamber, Pierre Auger observed a pair of electron tracks and identified their origin [1]. One track was due to the photoelectron with a length proportional to the energy of the X-ray source, and the other track of constant length resulted from the radiationless double ionisation of the atom. The ap-

plication of Auger emission as a surface technique was proposed by J.J.Lander in 1953, after identifying Auger transitions as small features on the secondary electron background. He proposed that since most elements had distinct Auger transitions occuring at low energy where the escape depth was small, the process could be used as a highly sensitive tool for surface analysis [2]. With the introduction of electronic differentiation (using a reference signal and lock-in techniques) by Harris in 1967, which converted the small features in the background into distinct lineshapes [3], the technique became extensively used.

When atoms in a crystal are ionised using X-ray radiation or high energy electrons (2-3 keV), core level holes are created with the emission of an electron. An outer electron can then decay into this hole, with the energy of the transition emitted as a photon (in the case of X-ray fluorescence) or by the transference of energy to another electron. If this energy is sufficient, the electron can escape the surface, leaving the atom doubly ionised. Fig(2.1) shows this process of Auger emission from a silicon crystal ionised by an electron. The incident electron is of high enough energy to dislodge a core electron (in this case from the K level), this core electron then escapes the atom adding to the secondary electron background. An electron in the L_1 level undergoes a transition to fill this K primary vacancy with the energy released to another electron in the $L_{2,3}$ level. If the energy released in the transition is greater than the binding energy of the $L_{2,3}$ (which in this case is so) then this Auger electron is emitted from the atom with energy E_A.

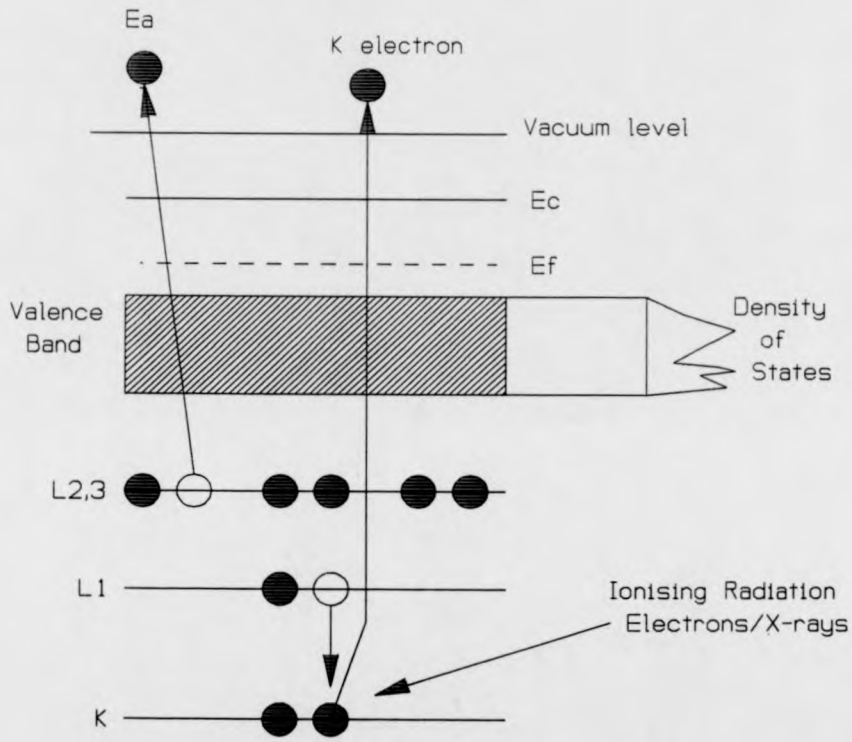

Fig 2.1: Schematic of the process of Auger emission from a Silicon crystal ionised by an electron.

$$E_A = E_K - E_{L1} - E_{L2,3} \tag{2.1}$$

This is only a first approximation, and does not take into account any relaxation effects accompanying both the initial ionisation and the transition of the electron to the K level vacancy. This Auger transition is specifically the $KL_{L1}L_{L2,3}$. The first letter specifies the shell containing the initial vacancy and the last two letters are the shells containing the electron vacancies created by the Auger emission [4]

Equation(2.1) is not an exact description of the Auger energy, since the double ionisation of the atom is not taken into consideration (the energy should lie between that of a one-hole and a two-hole binding energy state) [4]. A better approximation can be obtained if the binding energy of the Auger electron ($L_{L2,3}$ in Fig(2.1)) is substituted by the corresponding binding energy for an atom with atomic number $Z + \Delta$ ($\Delta = 1$ to account for this extra positive charge). Experimental values put Δ between $\frac{1}{2}$ and $\frac{3}{4}$ [5]. Generally, using the terminology of $WXY = KLL$, LMM etc. the kinetic energy of the Auger electron is given by equation(2.2).

$$E_A = E_W^Z - \frac{1}{2}(E_X^Z + E_X^{Z+1}) - \frac{1}{2}(E_Y^Z + E_Y^{Z+1}) \tag{2.2}$$

The electrostatic force between 'electron clouds' of unfilled shells is responsible for the Auger transitions, filled shells are symmetric and do not produce a net force. The positions of these 'clouds' are determined by the magnetic fields produced by the spin and orbital angular momentum (quantised by LS coupling and jj

coupling, dominant for light and heavy elements respectively), and determine the energy and number of possible transitions.

The two possible recombination processes possible following ionisation are dependent on the atomic number of the atom and the ionisation energy. At ionisation energies of approximately 2keV, atoms of a low atomic number (i.e $Z < 30$) have a greater possiblity of Auger emission than X-ray fluorescence. For higher atomic numbers and increased ionisation energies, X-ray fluorescence becomes the dominant recombination process [3, 6].

The Auger spectrum is dominated by a large secondary electron background. The Auger electrons are generated at depths up to the limits of primary beam penetration (600 to 1000 Å), and as the Auger electrons travel towards the surface (along with the removed core electron and initial ionising electron), they undergo inelastic collisions with other electrons and also lose energy to excitations of the valence electrons [2, 3, 7]. The mean escape depths of Auger electrons in a solid are 4 to 8 Å (mean free path)[8] and those which do not lose energy appear as weak peaks against the inelastic background. Any Auger electrons created below this depth will generally lose energy to become part of the background making the process very surface sensitive [6, 9]. Electronic differentiation using reference signal and lock-in methods (Harris 1968,[3]) has allowed great enhancement of these Auger features against the large background, making Auger electron spectroscopy a powerful tool in the chemical analysis of surfaces.

In the work detailed here, peak to peak height ratios are used as a direct probe of contaminants on the surface (the sensitivity limited by the Auger cross section

of the contaminant in question), this method enables the detection of 1–5% of a monolayer. For more accurate quantitative analysis necessary in the chemisorption experiments, the Auger signal amplitude has to be compared to pure elemental standards (taking into account instrumental factors together with such effects as ionisation cross section differences between various elements) [4, 10]. In experiments where the chemisorbed species produces a definite overlayer periodicity at a known coverage (the periodicity being checked with low energy electron diffraction, LEED), then the Auger signal of the adsorbate can be calibrated allowing estimations of adsorbate coverage at other Auger signal levels.

2.2 Low energy electron diffraction, LEED

Diffraction techniques are generally viewed as the best way of determining the structure of periodic systems, and in the case of solid surfaces LEED is by far the most widely used tool [11]. The experiments of Davisson and Germer in 1927 [12, 13], showed the wave nature of electrons, previously predicted by de Broglie [14] with the relation for the electron wavelength (in $\dot{A}$) as

$$\lambda = \sqrt{(150.4/E)} \tag{2.3}$$

energy E being in eV.

Since the surface atomic layers can differ in structure and periodicity from that of the bulk due to relaxation effects and/or absorbed species, knowledge of the surface structure is greatly valued. LEED is very surface sensitive, since the incident energies used are in the 30–300 eV range, with only the elastically

backscattered electrons being detected (mean free path around $5\mathring{A}$). This, together with elastic scattering from the top atomic layers (resulting in a smaller flux to each successive atomic layer), effects the sampling of only the first 2 or 3 atomic layers [10, 11]. As a consequence of its surface specificity, only translational symmetry in the 2-dimensions parallel to the surface are accounted for in the general theory (as opposed to the 3-dimensional case for X-ray diffraction). Therefore the wave vector parallel (and not perpendicular) to the surface is conserved with the addition of a reciprocal net vector (similar to the reciprocal lattice vector of the 3-D case) [10, 11, 15]. If the incident wavevector is k and the emerging wavevectors are k', then conservation of energy gives

$$(k)^2 = (k')^2 \tag{2.4}$$

Equation(2.4) can be re-written splitting into the components perpendicular and parallel to the surface (eqn(2.5)).

$$(\mathbf{k}_{||})^2 + (\mathbf{k}_{\perp})^2 = (\mathbf{k}'_{|})^2 + (\mathbf{k}'_{\perp})^2 \tag{2.5}$$

Applying conservation of momentum to the system:

$$\mathbf{k}'_{||} = \mathbf{k}_{||} + \mathbf{g}_{hk} \tag{2.6}$$

the perpendicular component of the wave vector not being conserved, and the reciprocal net vector being given by the relation:

$$\mathbf{g}_{hk} = h\mathbf{a}^* + k\mathbf{b}^* \tag{2.7}$$

a^* and b^* are the primitive translation vectors of the reciprocal net, and are

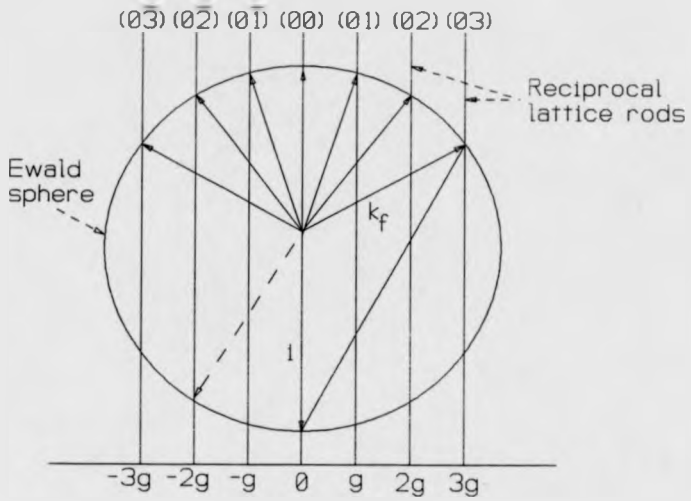

Fig 2.2: Ewald sphere construction for an electron beam incident normal to the surface. Seven backscattered beams are shown. The dashed line shows one beam not backscattered but propagating into the crystal. [15]

related to the real net vectors (a and b) by:

$$\mathbf{a}^* = 2\pi\frac{\mathbf{b}\times\mathbf{n}}{A}, \mathbf{b}^* = 2\pi\frac{\mathbf{n}\times\mathbf{a}}{A}, A = \mathbf{a}.\mathbf{b}\times\mathbf{n} \tag{2.8}$$

where **n** is the unit vector normal to the surface. Similar to the Ewald sphere construction used to describe the X-ray diffraction conditions from a 3-D lattice, a slightly different construction is used to describe the equations (2.4 - 2.8). Although maintaining the same 3-D Ewald sphere (incident and diffracted beams lie in 3 dimensions), the reciprocal lattice of the bulk is replaced by infinite reciprocal lattice rods that are perpendicular to the surface and which pass through the reciprocal net points (see Fig(2.2)) [10, 11, 15]. The diffracted beams can be denoted by 2 numbers (hk) which are determined by the 2-D reciprocal net vector. The construction is arranged in this way because it relaxes the conditions necessary for the formation of diffracted beams, so for the surface case, the variation of energy or wavevector would only mean the slight movement of the diffracted beams as opposed to the gain and loss of beams found in the bulk Ewald construction. From Fig(2.2), it can be seen that there are two beams which are associated with each lattice rod (or reciprocal net point), although only half of these are backscattered (the rest denoted by dashed lines, propagate into the crystal and are not detected).

The diffracted elecrons which are of importance are those which have undergone elastic scattering (or have energy very close to that of the incident electrons). The vast majority of the scattered electrons will be those that have been involved in energy loss events such as inelastic collisions and secondary scattering, as can be seen in the electron energy distribution graph (Fig(2.3) [11]).

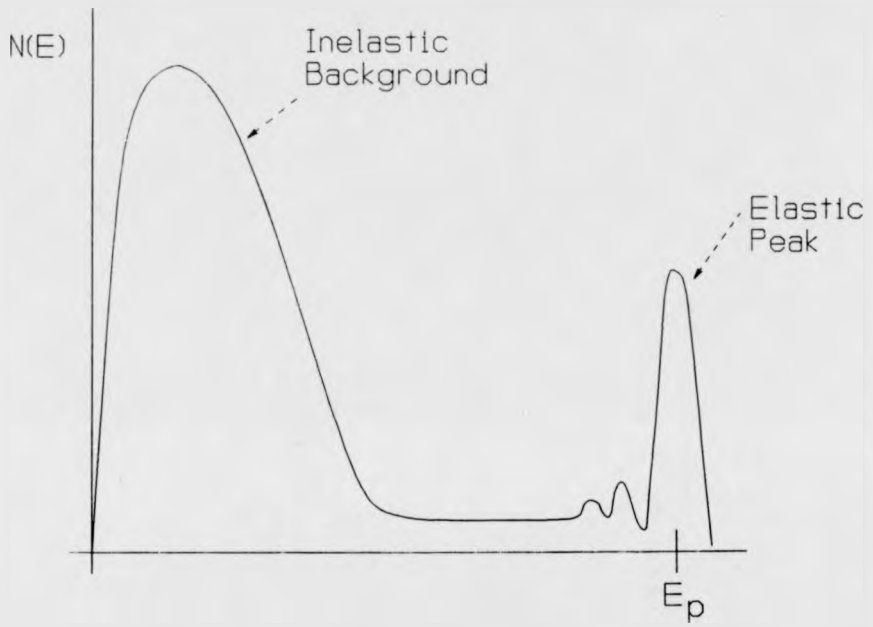

Fig 2.3: Typical energy distribution of secondary electrons in LEED. E_P is the primary energy of the incident electrons, with the peak at this value due to elastically backscattered electrons. The small features just below E_P are due to losses of discrete amounts of energy due to excitations of plasmons and interband transitions [11].

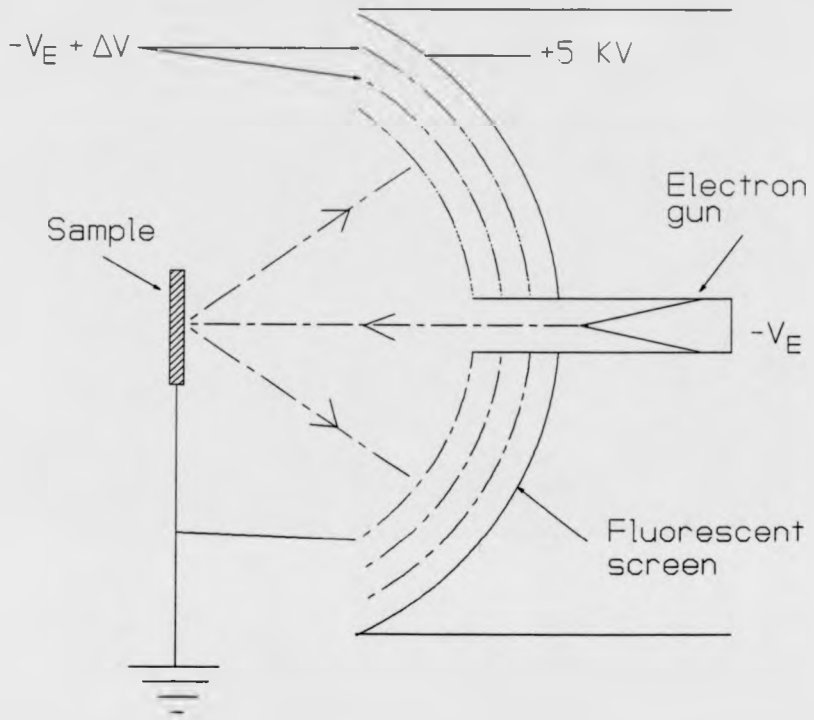

Fig 2.4: Schematic of LEED optics. Electrons that have undergone energy loss events are stopped by the second and third grids, with only the elastically backscattered electrons being allowed to propagate before accelerating onto the fluorescent screen.

To obtain a LEED pattern therefore, a series of grids are placed in the path of the diffracted electrons which are set to potentials which will retard electrons below the incident energy to allow only the elastically diffracted electrons to pass, before accelerating them onto a fluorescent screen. Fig(2.4) shows LEED optics similar to those on the k-resolved inverse photoemission spectroscopy (KRIPES) chamber used in the work reported in this thesis.

The information obtainable from the LEED pattern is given in terms of the translational symmetry and the periodicity of the surface. In order to determine details of the relative atomic positions within the unit mesh, measurements of the intensities of the diffracted beams need to be taken (as is the case for X-ray diffraction), but the calculations needed to analyse these measurements are a great deal more complicated than the equivalent in X-ray diffraction. Full reviews of the methodolgy of LEED can be found in references [16, 17].

2.3 Synchrotron radiation

2.3.1 Introduction

When electrons are either accelerated or deccelerated they lose energy in the form of electromagnetic radiation. If these electrons are accelerated in a circular orbit at relativistic velocities using magnets, the emitted radiation (the energy of which covers a broad continuous range from infra-red to hard X-rays) is known as synchrotron radiation [18, 19], and has become a powerful light source for a wide range of applications including surface-specific investigations. There are

many advantages associated with using synchrotron radiation over the normal laboratory light sources, the most important of which concern intensity, spectral range and polarisation [20]. In the u.v range, the intensity of the synchrotron radiation is several orders of magnitude greater than the typical He gas discharge line sources, although after monochromating the radiation to a similar resolution to that found with the HeI and HeII lines, the intensity of the gas disharge source is comparable to that of the synchrotron source [10]. It is often the case that a trade off between resolution and intensity is made with experiments taking synchrotron light. For the higher X-ray range however, the synchrotron source even after monochromating the beam is still at least two orders of magnitude greater than the best laboratory sources (such as Al and Mg K_α sources) [10]. The main advantage therefore lies in the tunability of the radiation. One example of this is in the use of photoemission, which prior to synchrotron radiation was distinctly grouped into ultra-violet or X-ray photoemission techniques (UPS or XPS), and can now be performed in the energy range from several eV to several hundred eV especially on core levels [10], see for example the core level photoemission investigation in chapter **5**. Another example of the advantage of tunable radiation is shown in the normal incidence standing X-ray wave study in chapter **6**, where the radiation is monochromated to match the Bragg energy of the reflecting Al(111) Bragg planes to obtain an X-ray standing wave, and subsequently varied to allow an energetic sweep of the Bragg condition. Another advantage mentioned is the high degree of polarisation from a synchrotron source, with the emitted radiation polarised with the electric vector parallel to the acceleration vector. In the direc-

tion of motion of the electron, the radiation is 100% polarised within the orbital plane [20]. This high degree of polarisation can be of value in determining the orientation of adsorbed or surface bonded molecules [19]. The polarisation of the radiation emitted out of the orbital plane decreases as the wavelength and the out-of-plane angle increase [22].

2.3.2 Basic theory

Detailed reviews on synchrotron radiation theory can be found in references [19, 20, 21]. Electrons travelling at relativistic velocities of energy E in a magnetically constrained orbital path in an accelerator will emit radiation in a narrow cone about a tangential direction with half angular spread of approximately mc^2/E radians. The time averaging effect of the motion means that the observed angular distribution in the orbital plane will be independent on the wavelength (λ). Since most experiments are performed using monochromatic incident radiation, the relevant intensity parameter is defined as the intensity of the flux collected by a monochromator within a narrow wavelength bandwidth [22]. A reasonable value to take in practice is $\delta\lambda$, where $\delta\lambda/\lambda = 10^{-3}$, or $1\dot{A}$ at $\lambda = 1000\dot{A}$ for example. The units used for the photon flux from a radiation source are therefore *No. of photons emitted per second, per milliradian of horizontal angle in bandwidth* $\delta\lambda$. If the circulating electron flux is normalised to $1mA$, then the photon flux (in photons/s/mrad/mA in 0.1% bandwidth) can be written:

$$N(\lambda) = 2.46 \times 10^{10} \left(\frac{\lambda}{\lambda_C}\right)^2 EG\left(\frac{\lambda}{\lambda_C}\right) \tag{2.9}$$

with E being the energy of the electrons in GeV and λ_C being the characteristic wavelength of the spectrum where

$$\lambda_C = \frac{4\pi R}{3}\left(\frac{m_o c^2}{E}\right)^3 = \frac{5.6R}{E^3} = \frac{18.6}{BE^2}\dot{A} \tag{2.10}$$

with the field strength of the bending magnets B in Tesla and the radius of electron bending orbit R in meters (R=5.55m from the Daresbury 'Synchrotron Radiation Source' (SRS)). $G(\lambda/\lambda_C)$ is the universal function defined by a modified Bessel function. From eqn(2.9) it can be seen that $N(\lambda)$ depends only on λ/λ_C and electron energy [22]. This relationship defines the universal curve, which is a plot of $N(\lambda)/E$ against λ/λ_C, as shown in Fig(2.5) [23].

2.3.3 Daresbury synchrotron radiation source

The experimental results presented in chapters **5** and **6**, were obtained at the S.E.R.C Synchrotron Radiation Source (SRS) at Daresbury Laboratory, Warrington, UK. The source utilises a storage ring system; a schematic of the laboratory is shown in Fig(2.6), with the linear accelerator (LINAC) and the storage ring labelled [24]. Synchrotron radiation produced by storage rings has many advantages over radiation produced by synchrotrons, including better stability, ultra-high vacuum (UHV) environment and a much reduced source spot size [20]. The first stage in the process of obtaining synchrotron radiation at the SRS is the linear accelerator (LINAC) which produces electrons (from a hot cathode) and accelerates them to 12 million electron volts (12 MeV) before sending them to a booster synchrotron where they are accelerated to energies of 600 MeV.

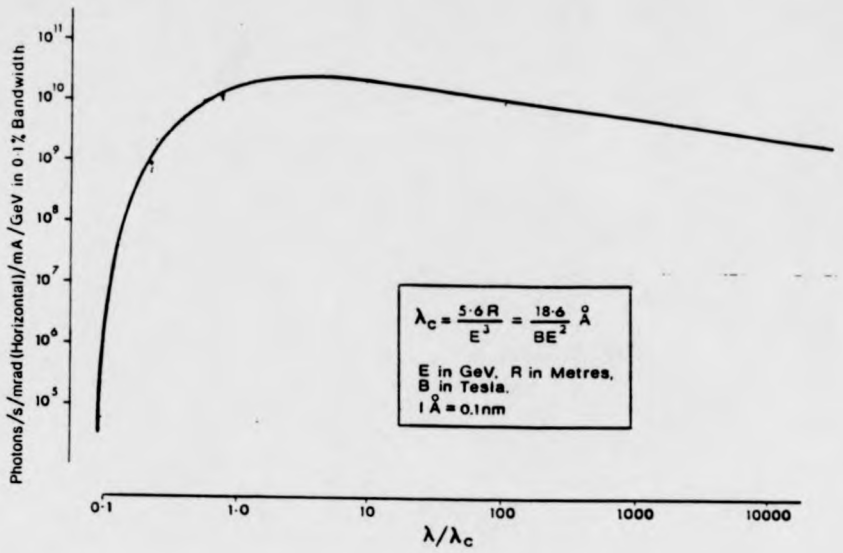

Fig **2.5**: Universal Synchrotron radiation spectral curve for an electron storage ring [22].

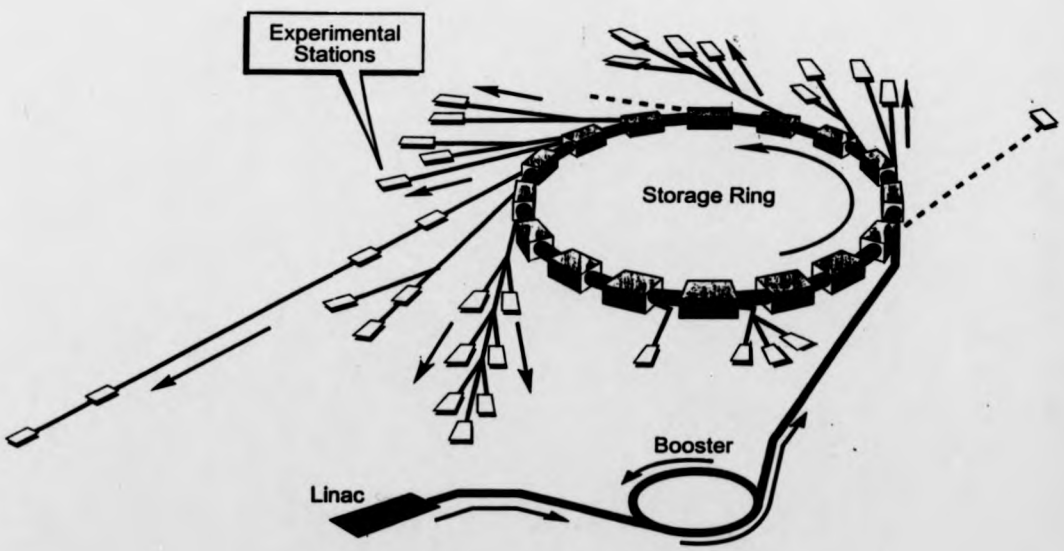

Fig **2.6**: Daresbury Synchrotron radiation source [24].

The electrons are then injected into the storage ring, where they are accelerated to 2 GeV (traversing the 96 m circumference 3.12 million times a second). The main elements of the storage ring itself are

- **16 bending magnets** to constrain the electrons to travel in a circular orbit.
- **Radio frequency (rf) accelerator** to accelerate the electrons to 2 GeV and to replace the energy lost by the electron beam in the process of emitting radiation.
- **Vacuum pumps** to achieve UHV.
- **Quadrupole magnets** to focus the circulating electrons.
- **Other specialist magnets** such as wiggler magnets to produce a higher magnetic field to obtain lower wavelength radiation.

The lifetime of the beam once achieved is very sensitive to the vacuum conditions of the ring. Generally it is not uncommon to have a usable beam for greater than 20 hours, with the injection process taking 10% of this time [20] In Fig(2.6), it can be seen that light is taken from points around the ring at beam ports, with some ports supplying several experimental stations. The experimental stations used in the studies of chapters 5 and 6 are 6.1 and 6.3, with the beam port 6 taking 28 mrad of horizontal angular acceptance [25].

2.3.4 Beam line 6.1 : Core-level photoemission

The beam line 6.1 experimental station takes 8 mrad of the 28 mrad horizontal acceptance of beam port 6. A platinum coated glass mirror is used for focusing the beam, with a tungsten mesh placed prior to the monochromator for monitoring beam intensity (for subsequent normalisation of data). The monochromator is a Miyake-West plane grating grazing incidence monochromator [26] which operates in the photon energy range $95 \rightarrow 135eV$ at a resolution of approximately $150meV$ [27, 28] (see Fig(2.7)). Detection of the photoelectrons and Auger spectroscopy was achieved using a Physical Electronics double-pass cylindrical mirror analyser (CMA) operated at pass energies of 5eV and 10eV [33]. The CMA is positioned such that its axis is in the horizontal plane of the electron storage ring, and at an angle of 90° to the direction of incident radiation; in the chemisorption study of chapter 5, the aluminium sample was mounted at 45° to these directions [27]. The main chamber is also equipped with LEED optics for structure analysis.

2.3.5 Beam line 6.3

Beam line 6.3 is generally used for surface extended X-ray absorption fine structure (SEXAFS) experiments but is also ideal for normal incidence X-ray standing wave experiments (NISXW)[30]. The line is equipped with a prefocusing mirror and a water cooled double crystal monochromator [31, 32], with a low energy cut-off of 2 keV, (see Fig(2.8)). A double path CMA was used for Auger electron and photoelectron detection, with a LEED optics also positioned on the experimental chamber.

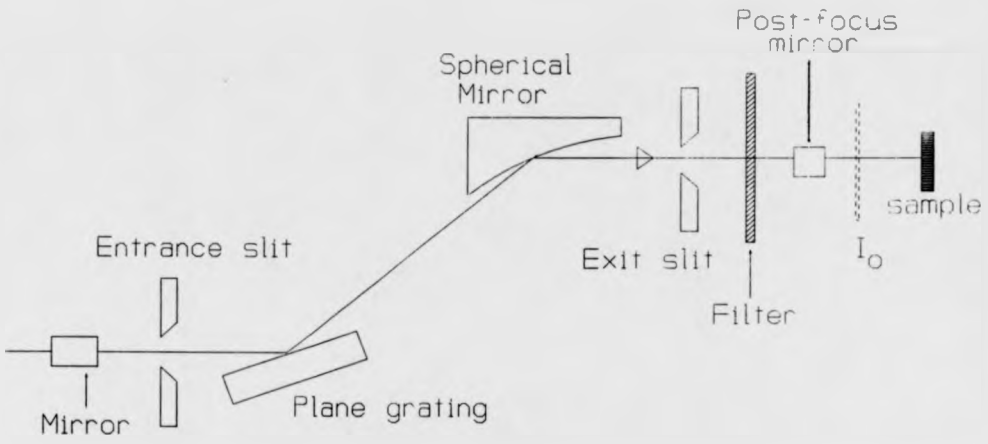

Fig 2.7: Miyake-West plane grating grazing incidence monochromator installed on beamline 6.1 [28].

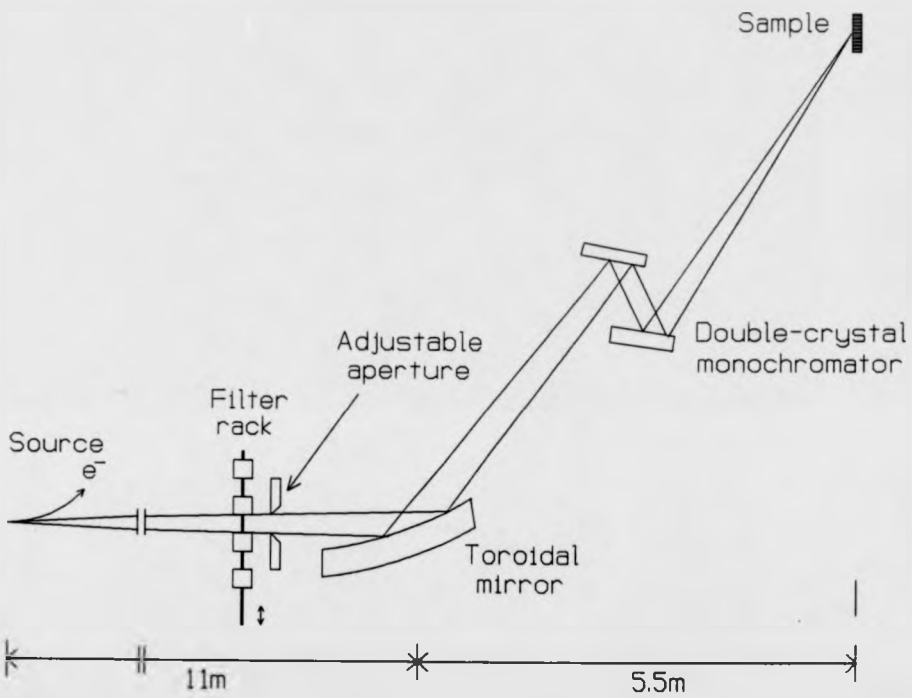

Fig 2.8: Double crystal monochromator installed on Beam line 6.3 [32]

References

[1] P.Auger, J. Phys. Radium **6**, p205 (1925)

[2] J.J.Lander, Phys. Rev. **91**, 6 p1382 (1953)

[3] L.A.Harris. J. Appl. Phys. **39**. 3 p1419 (1968)

[4] J.T.Grant, Applic. Surf. Sci. **13**, p35 (1982)

[5] I.Bergstrom and C.Nordling, *Alpha, Beta and Gamma Ray Spectroscopy*, Vol.2, Ed. K.Siegbahn (North-Holland, Amsterdam, 1965) p1523

[6] Chuan C.Chang, Surf. Sci. **25**, p53 (1971)

[7] D.Chattarji, *The Theory of Auger Transitions* . (Academic Press, 1976)

[8] P.W.Palmberg, T.N.Rhodin. J. Appl. Phys. **39**, 5, p2425 (1968)

[9] S.R.Morrison, *The Chemical Physics of Surfaces*, (Plenum Press, New York and London, 1977) Chpt.3

[10] D.P.Woodruff and T.A.Delchar, *Modern techniques of surface science*, (Cambridge University Press, 1986)

[11] *Emission and Scattering Techniques* Chpt.8 ed. P.Day (D.Reidel Publishing Company, 1981)

[12] C.Davisson and L.Germer, Nature **119**, p558 (1927)

[13] C.Davisson and L.Germer, Phys. Rev. **30**, p705 (1927)

[14] L. de Broglie, Phil. Mag. **47** p446 (1924)

[15] A.Zangwill, *Physics at Surfaces*, (Cambridge University Press. 1988)

[16] J.Pendry, *Low Energy Electron Diffraction*, (Academic Press, London. 1974)

[17] M.A.Van Hove and S.Y.Tong, *Surface Crystallography by LEED*, (Springer-Verlag Berlin,Heidelberg,New York. 1979)

[18] *Practical Surface Analysis* ed. D.Briggs and M.P.Seah, (John Wiley and sons, Chichester. 1983)

[19] *Handbook on Synchrotron Radiation Vol.3* ed. G.S.Brown and D.E.Moncton, (North-Holland, Amsterdam 1991)

[20] *Synchrotron Radiation Research* ed. H.Winick and S.Doniach, (Plenum Press, New York and London. 1980)

[21] G.Margaritondo, *Introduction to Synchrotron Radiation*, (Oxford University Press, Oxford. 1988)

[22] Daresbury Laboratory report DL/SRF/R2

[23] V.P.Suller, Daresbury Laboratory technical memorandum DL/TM 118

[24] Daresbury Laboratory information booklet (January 1990).

[25] C.F.McConville, PhD thesis, University of Warwick, 1984.

[26] M.R.Howells, D.Norman, G.P.Williams and J.B.West, J. Phys. E : Sci. Instrum., vol**11**, p199 (1978)

[27] C.F.McConville, D.L.Seymour, D.P.Woodruff and S.Bao, Surf. Sci. **188**, p1 (1987)

[28] P.Bailey and F.Quinn, Daresbury Laboratory Technical Memorandum DL/SCI/TM 94E (1993).

[29] C.F.McConville, A.B.Hayden, J.Robinson and D.P.Woodruff, submitted to J. Phys. Condensed Matter.

[30] M.Kerkar, A.B.Hayden, D.P.Woodruff, M.Kadodwala and R.G.Jones, J. Phys. : Condens. Matter **4**, p5043 (1992)

[31] A.A.MacDowell, D.Norman, J.B.West, J.C.Campuzano and R.G.Jones, Nucl. Inst. Meths. **A246**, p131 (1986)

[32] A.A.MacDowell, D.Norman and J.B.West, Rev. Sci. Instrum. **57**, p2667 (1986)

[33] P.W.Palmberg, J. Elect. Spec. Rel. Phenom. **5**, p691 (1974)

Chapter 3

k-Resolved Inverse Photoemission Spectroscopy (KRIPES)

Contents

3 k-Resolved Inverse Photoemission Spectroscopy (KRIPES) 34

3.1 Theory 36

3.1.1 Complementary nature of photoemission and inverse photoemission 36

3.1.2 The inverse photoemission process 39

3.1.3 Bulk states and band mapping 45

3.1.4 Surface states 56

3.1.5 Discrimination of bulk and surface features 63

3.2 KRIPES experimental system 65

3.2.1 UHV 65

3.2.2 KRIPES chamber geometry 66

3.2.3 Sample mounting, manipulation and cleaning processes . . 72

3.2.4 Magnetic field cancellation 74

3.2.5 General analytical techniques 74

3.2.6 KRIPES electron gun specifications 75

3.2.7 Isochromat detector instrumentation 85

3.1 Theory

The technique of inverse photoemission (or Bremsstrahlung spectroscopy) is a method of exploring the unoccupied electronic states of solid surfaces, and has particular importance in that it accesses the energy range between the Fermi level and the vacuum level (a range inaccessible in ordinary photoemission).

The relationship between the incident light frequency and the maximum electron kinetic energy in photoemission was developed by Einstein [1], with the demonstration of the inverse relation to the process (determining the maximum emitted X-ray frequency from a sample bombarded with electrons) following a decade later [2]. Although photoemission became an important spectroscopic tool for studying electronic states in solids and at their surfaces in the 1960's (and later with angle resolved photoemission spectroscopy, ARPES), the inverse technique had received little attention until the early 1980's [3].

The process of k-resolved IPES (in the ultra-violet range) and the information obtainable using this technique are discussed in this section together with comparisons to PES.

3.1.1 Complementary nature of photoemission and inverse photoemission

As its name suggests, inverse photoemission is basically the reverse of ordinary photoemission. In the photoemission process, a photon of energy $\hbar\omega$ is incident upon a sample surface and the photon energy is absorbed by an electron. This

excited electron may then have energy enough to escape from the surface into the vacuum. Inverse photoemission, on the other hand, involves an electron of known energy incident upon the sample surface, which couples to an evanescent state decaying via a radiative transition to an unoccupied state with the release of a photon of energy $\hbar\omega$, see Fig(3.1). A main reason for the delayed application of ultra-violet IPES as an experimental technique can be seen by comparing the cross sections for photoemission and inverse photoemission processes [4, 5, 6]. If it is assumed that the two processes are the exact reverse of each other, the ratio of the cross sections can be shown to be given by

$$r = \frac{\sigma_{IPES}}{\sigma_{PES}} = \left(\frac{\lambda_e}{\lambda_p}\right)^2 \tag{3.1}$$

where λ_e and λ_p are the electron and photon wavelengths respectively. Typically for the ultra-violet energy range: $\lambda_e = 4\dot{A}$, $\lambda_p = 1200\dot{A}$, at electron and photon energies of $10eV$, resulting in a ratio of $r \approx 10^{-5}$ [4]. The expected signal levels in a photoemission experiment are therefore some five orders of magnitude greater than for an inverse photoemission experiment, hence the necessity for highly sensitive detection in the latter.

Generally in PES, the incident photon energy is kept constant and the emitted electron energy measured, the resulting spectra showing the density of states. In contrast, the IPES system at Warwick University relies on varying the incident electron energy and monitoring the emitted photons in fixed energy (or isochromat) mode. The spectra produced in this manner then provide a measure of the density of unoccupied states.

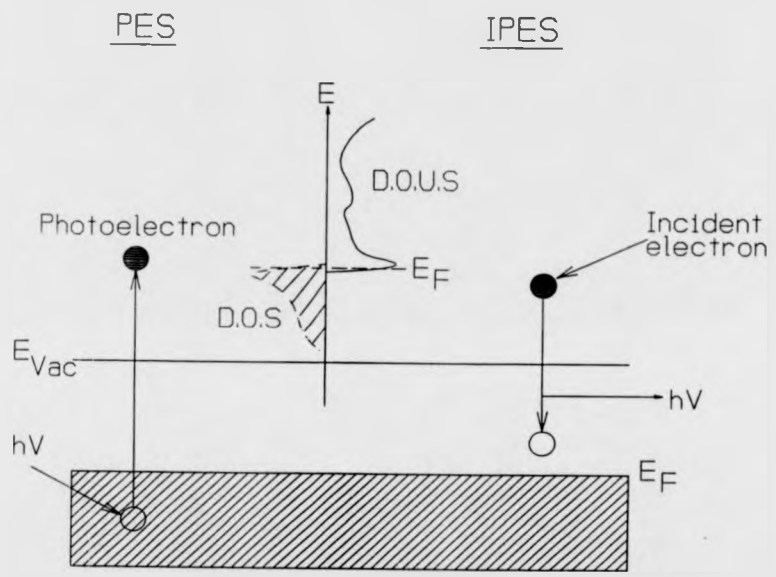

Fig 3.1: Schematic of photoemission and inverse photoemission processes. The spectra of the former depict the density of states (DOS), and the latter the density of unoccupied states (DOUS).

By using a combination of the two techniques, it can be seen that a full picture of occupied states and unoccupied states can be realised (see Fig(3.1)). Using ARPES, the angle of emission is measured and hence the momentum of the photoelectron deduced, enabling the mapping of the dispersion of occupied states [4, 7, 8, 9]. Similarly, by defining the incidence angle of the electrons in IPES, and hence defining the momentum, it is also possible to map the dispersion of the unoccupied states. This latter technique is generally known as k-resolved inverse photoemission spectroscopy (KRIPES).

3.1.2 The inverse photoemission process

The theory of inverse photoemission from solid surfaces has been thoroughly detailed by Pendry [10] . This theory treats inverse photoemission as a time reversed version of photoemission, the theory for which is well established [11, 12, 13, 14]. The theory incorporates the three steps of inverse photoemission, namely:

- wave function matching at the surface for an incoming electron plane wave.
- the attenuation of the electron wave due to inelastic electron-electron interactions.
- the radiative decay of the electron.

in a coherent quantum mechanical way (or as 'one step'). This approach was successful in that both surface and bulk derived features in the spectra could be generated along with predicted intensities and polarisation sensitivity. Further

changes to this general theory have been mainly to the shape of the surface barrier [4, 15]. Originally the barrier was represented by a potential step, and later by a more realistic image potential asymptotic form of barrier.

Although this 'one step' theory is good at reproducing bulk and solid surface IPE spectra [16], it does assume the process is almost the time reversed version of photoemission. What is not taken into account is the difference between the final states of the two systems. In photoemission, there is a decrease of the number of electrons in the system, whereas in inverse photoemission there is an increase, hence producing a difference of two electrons between final state densities [4]. Although this is of little concern in IPES from delocalised electrons and states in solid metal surfaces, it is very important in the IPES from the more localised valence states of molecules (both free and adsorbed). Johnson and Davenport presented a theory which accounted for this discrepancy [17], but this is not detailed in this thesis which concentrates on strongly bonded atomic species on metal surfaces.

3.1.2.1 Conservation of energy and momentum

In a KRIPES experiment, an electron of energy E_i and known momentum is incident on the sample surface. This electron may then undergo a radiative (direct) transition (from an evanescent initial state) to a previously unoccupied final state of energy E_f with the emission of a photon of energy $\hbar\omega$. The final state energy can be calculated by conservation of energy

$$E_f = E_i - \hbar\omega \tag{3.2}$$

As the final state has to be unoccupied before the transition, it has to lie above the Fermi level.

The intensity distribution of the emitted radiation, as in the photoemission case, is determined by a matrix element [16, 18].

$$H_{if} \propto A_\sigma < E_f, k_f, 1 \mid \exp^{iq.r} \Delta V a^+_{q\sigma} \mid E_i, k_i, 0 > . \tag{3.3}$$

This characterises the energy and momentum of the electrons in the solid, and defines the number of photons of polarization σ and wave vector q in the radiation field. V represents the bulk potential of the solid, and A_σ the vector potential amplitude. $a^+_{q\sigma}$ is the photon creation operator (similar to the annihilation operator in photoemission). The bulk potential of the solid (V) can be expressed in terms of a Fourier series summing over reciprocal lattice vectors **G**, for a monocrystalline solid [19].

$$V(r) = \sum_G V_G \exp^{iG.r} \tag{3.4}$$

Finally the initial and final wave vectors are denoted by k_i and k_f. If free electron states are used to denote the initial and final electronic states, then H_{if} becomes

$$H_{if} \propto A_\sigma \sum_G V_G \int \exp^{-ik_f.r} . \exp^{iq.r} . \exp^{iG.r} . \exp^{ik_i.r} d\tau \tag{3.5}$$

This vanishes unless eqn(3.6) (stating momentum conservation) is satisfied.

$$k_f - k_i = G + q \tag{3.6}$$

Since only the part of the wavevector parallel to the surface is conserved in the optical transition and in the matching of the wave-function at the surface, eqn(3.7) is more strictly written

$$(k_{||})_f = (k_{||})_i \pm g_{||} \tag{3.7}$$

Here the momentum parallel to the surface is conserved in the process, with the exchange of a reciprocal lattice vector $g_{||}$ necessary for a direct transition to occur [7, 20]. The momentum of the emitted photon is negligible in the energy range considered here (below approximately 40 eV) and is omitted from the momentum balance [19]. Fig(3.2) shows the dispersion of a nearly free electron in a periodic potential in the extended zone scheme, and in the reduced zone scheme, illustrating the direct transition across a bulk band gap. This direct transition forms the basis of band mapping [7]. In the experimental situation, the energy of the incident electrons is varied whilst only photons of a fixed energy are detected. This isochromat energy then limits the transitions that can be observed to direct transitions between initial and final states separated by this energy (see Fig(3.3) [21]). If spectra are acquired over many incident angles (i.e varying $k_{||}$), then the dispersion of these final states can be plotted as an $E_f(k_{||})$ relation [21, 22, 23]. The low energies ($E_{KE} < 20eV$) used in KRIPES, make the penetration depth of the incident electrons very small ($\approx 10\AA$), hence the technique is very surface sensitive. Even in such thin layers, however, the bulk electronic structure is largely developed, so KRIPES spectra show contributions from both the bulk and the surface.

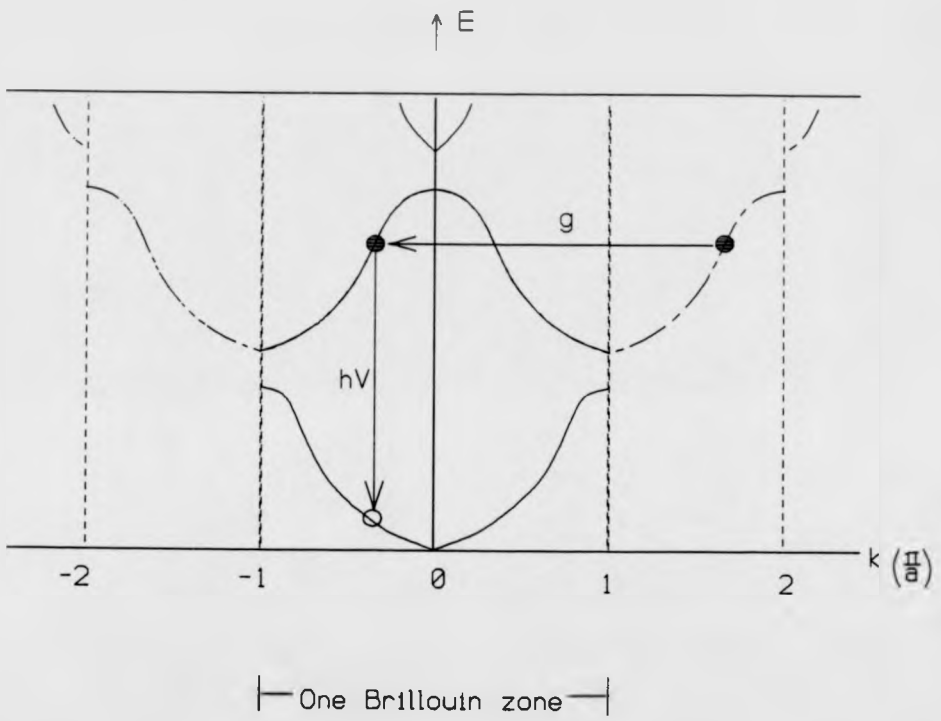

Fig 3.2: The dispersion of an electron in a periodic potential in an extended zone scheme, and with the folding back of the zones to show the direct transition in reduced zone scheme.

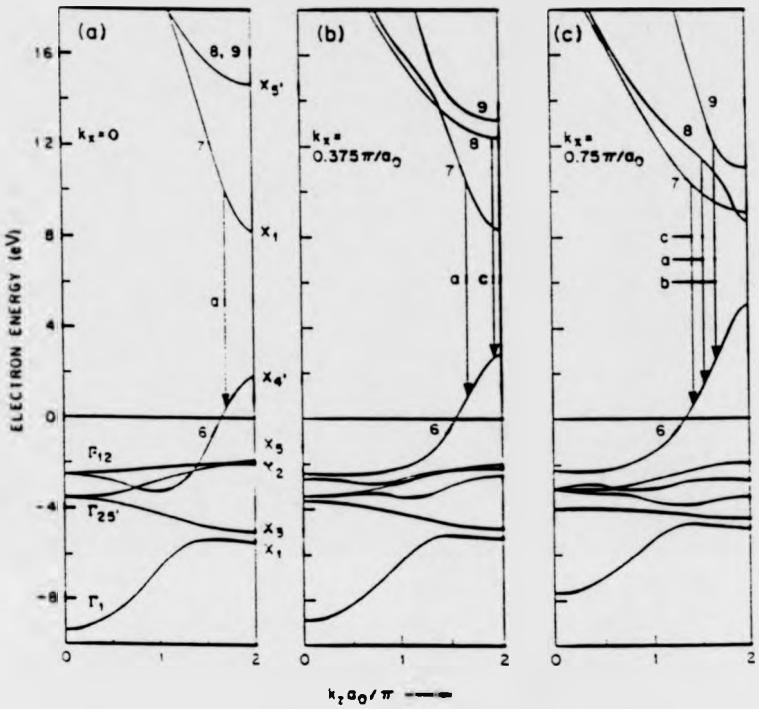

Fig 3.3: Series of sections of the band structure of copper, with the vertical lines showing allowed (or direct) transitions at a constant isochromat energy of $hV = 9.7eV$.

(a) along ΓX direction (normal incidence)

(b) parallel to ΓX but at 20° with respect to normal incidence (i.e $k_{||} = 0.375(\pi/a_o)$)

(c) parallel to ΓX but at 40° with respect to normal incidence (i.e $k_{||} = 0.75(\pi/a_o)$.

a_o is the bulk lattice parameter ($\approx 3.615\mathring{A}$) for Cu.

3.1.2.2 Secondary emission

The possibility of the energetic decay being inelastic has so far been ignored. Not all the incident electrons will follow the elastic route, some will undergo inelastic electron-electron scattering possibly decaying through a lower energy radiative transition that will add a background to the IPE spectra [24, 21]. If the probablility of a non-radiative decay is $\Upsilon(E)$ then it follows that the probability for a radiative decay is $(1-\Upsilon(E))$. In Fig(3.4), two possible paths are shown for a radiative decay (of energy $\hbar\omega_o$), on the left is the 'elastic' route (E_i to E_f) and on the right is the 'inelastic' route (E_i to E^* to E_{f_2}) for which the probability can be written as $\Upsilon^*(E_i, E^*)$. The inelastic background can be calculated from eqn(3.8)

$$N^*(\hbar\omega, E_i) = \int_{E_F+\hbar\omega}^{E_i} N(\hbar\omega, E^*)\Upsilon^*(E_i, E^*)dE^* \tag{3.8}$$

The probability of the 'inelastic' partial radiative decay is related to the total probability of a non radiative decay (occuring through electron-electron scattering) by eqn(3.9)

$$\Upsilon(E) = \int_{E_F}^{E_i} \Upsilon^*(E_i, E^*)dE^* \tag{3.9}$$

Dose and Reusing have described procedures for adding this background to theoretical predictions [24].

3.1.3 Bulk states and band mapping

In order to describe best the features that can be observed and the different techniques used to predict their dispersion, some published KRIPES data from Cu(111) are used as an example in this section [25].

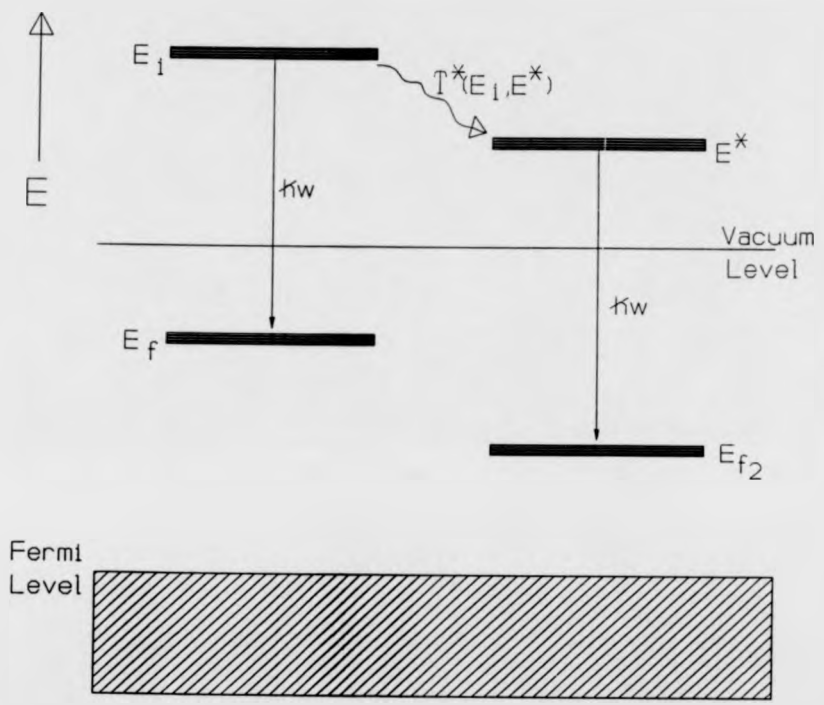

Fig 3.4: Normal transition $E_i - E_f$, together with an alternative possibility of inelastic partial radiative decay $E^* - E_{f2}$ (of the same isochromat energy) that would add to the IPES background.

Fig **3.5:** (a) Experimental KRIPES data from Cu(111) [25], at $\hbar\omega = 10.2eV$ as a function of angle of electron incidence θ.

(b) Experimental and theoretical $E(k_{\|})$ dispersion curves for Cu(111) in the $\bar{\Gamma}\bar{K}$ azimuth. Filled and open circles correspond to data taken at 10.2 eV and 11.0 eV photon energies respectively.

(a)

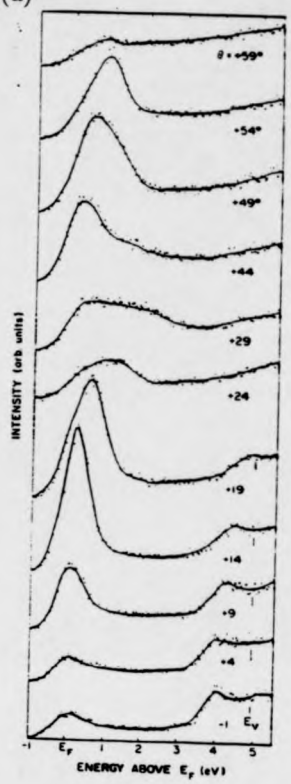
θ = +59°
+54°
+49°
+44
+29
+24
+19
+14
+9
+4
-1
E_V
INTENSITY (arb units)
-1
E_F
1
2
3
4
5
ENERGY ABOVE E_F (eV)

(b)

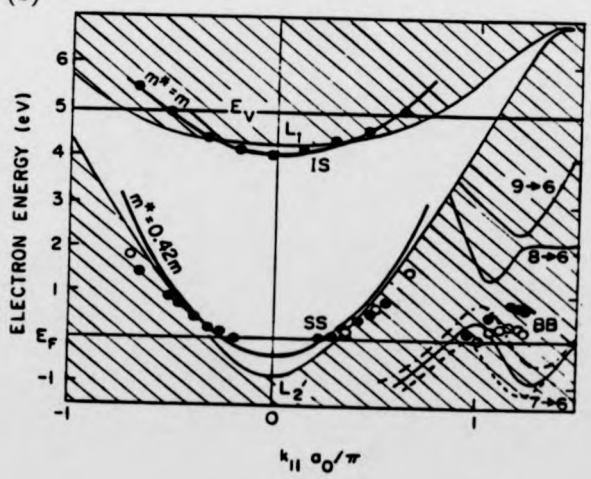
ELECTRON ENERGY (eV)
6
5
4
3
2
1
E_F
-1
m* = m
E_V
L_1
IS
m* = 0.42m
SS
9→6
8→6
BB
7→6
L_2'
-1
0
1
k_∥ a_0/π

The spectra in Fig(3.5a) were taken over varying incidence angles using an isochromat energy of 10.2 eV. The spectra taken at incidence angles up to $\theta = +19°$ show two distinct features. A peak just above the Fermi level is seen to increase in intensity and disperse to higher energy with increase in angle; this is attributed to a Shockley surface state. The second feature can be seen just below the vacuum level which also disperses up in energy with increase in angle; this state is an image state and its origin is discussed along with other surface state features in section(3.1.4). At the higher angles of incidence, a second peak close to the Fermi level can be seen, and this can be assigned to direct transitions occuring between s-p bands of the bulk band structure. The information regarding the dispersion of the three features in Fig(3.5a) is shown in the $E_f(k_{\|})$ plot in Fig(3.5b).

3.1.3.1 Mirror planes and symmetry considerations

Since the band structure of even simple crystals can be complicated at general points in k-space, it is more advantageous to perform experiments in mirror planes. Fig(3.6) shows the ΓXWK and ΓXUL mirror planes in the Brillouin zone of a face centred cubic (fcc) crystal. In these planes, different bands may become degenerate, reducing the complexity of the observed spectra. Symmetry requirements also mean that the bands cross the mirror planes with zero slope, allowing KRIPES peaks to be used for proper crystal positioning and absolute k-space location [19, 26]. The number of energetically possible transitions are also reduced due to special selection rules that apply to experiments in mirror

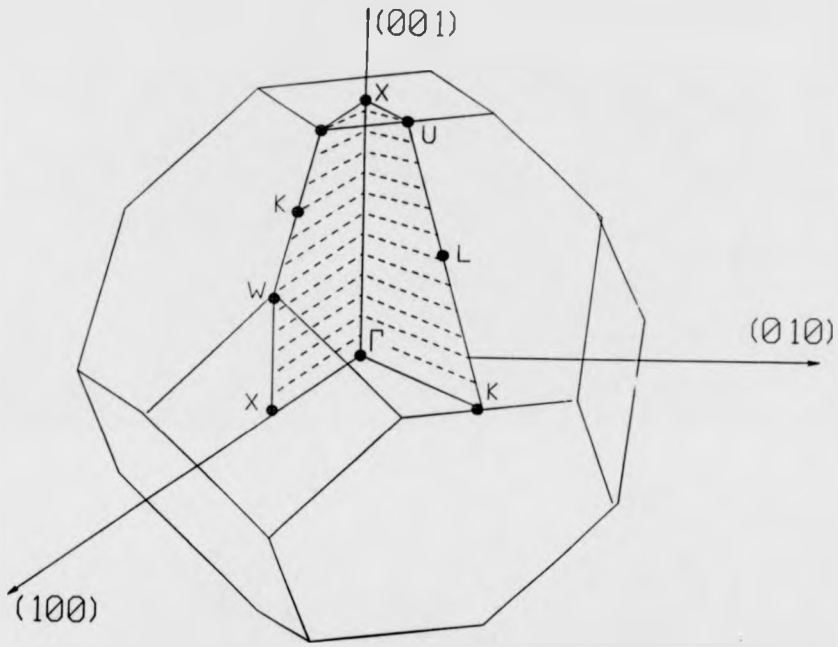

Fig 3.6:Brillouin zone of a face centered cubic (fcc) crystal with ΓXWK and ΓXUL mirror planes shaded.

-planes, and this has the effect of simplifying the final spectra.

Returning to the matrix element H_{if} of eqn(3.3), we can write:

$$H_{if} \approx A_\sigma < \Psi_f \mid (\nabla V) \mid \Psi_I > \tag{3.10}$$

$$\approx A_{\parallel} < \Psi_f \mid (\nabla V)_{\parallel} \mid \Psi_i > + A_{\perp} < \Psi_f \mid (\nabla V)_{\perp} \mid \Psi_i > \tag{3.11}$$

with $\parallel$ and $\perp$ referring to parallel and perpendicular to the mirror plane. In a mirror plane, the solution of Schrödingers equation must be of even (+) or odd (-) parity under mirror plane reflection. The wavefunction of an electron in an IPE experiment approaching the crystal surface in a mirror plane will have even parity and can only couple to states of the solid surface which also have even parity. The matrix element vanishes unless the integrand is even under reflection, so finite values can only occur if operator and final state have the same parity. The parallel and perpendicular components of the momentum operator (i.e. $(\nabla)_{\parallel}$ and $(\nabla)_{\perp}$) in equation(3.11) have even and odd parity respectively. Equation(3.11 can be written identically as

$$H_{if} \approx A_{\parallel} < (+) \mid (+) \mid (+) > + A_{\perp} < (-) \mid (-) \mid (+) > \tag{3.12}$$

Emission with light polarisation vector in the mirror plane is thus the result of transitions into final states with even parity, and similarly emission with polarisation perpendicular to the mirror plane will be a result of transitions into final states of odd parity.

It is possible then, from the angular distribution of the emitted radiation (which is influenced by the polarisation of the radiation) to obtain information concerning the symmetry of the unoccupied bands in the observed transitions

[26, 19].

3.1.3.2 Mapping the band structure

The value of $k_{||}$ is determined by the incident energy and angle of the electron, given by eqn(3.13)

$$k_{||} = \left[\frac{2m(E_i - E_V)}{\hbar^2}\right]^{1/2} \sin\theta \tag{3.13}$$

where E_i is the initial state energy and E_V the vacuum level. The kinetic energy of the electron is $(E_i - E_V)$, so eqn(3.13) simplifies to

$$k_{||} = \left[\frac{2mE_{KE}}{\hbar^2}\right]^{1/2} \sin\theta \tag{3.14}$$

The corresponding values of E_f can be found by finding the isochromat surface given by

$$E_i(\vec{k}) - E_f(\vec{k}) - \hbar\omega = 0 \tag{3.15}$$

The features in Fig(3.5a) are shown in the $E_f(k_{||})$ dispersion plot of Fig(3.5b). The shaded region represents the projection of the bulk band structure, the unshaded region the bulk band gap in this direction.

The electrons in the s-p part of the conduction band are itinerant, experiencing only small potentials due to ion cores and can therefore be treated as free-electron-like in character. There are two main reasons why the strong electron-electron interaction and the electron interaction with the positive ion cores give the net effect of a weak potential. Firstly, the electron interaction with the ion cores is strong at small separation, but the electrons are forbidden to get into close neighbourhood with the ion due to Pauli's exclusion principle. Secondly, the conduction electrons are highly mobile reducing the net potential on any single

electron by screening of the ion potential. The dispersion of these states (of the form shown in eqn(3.16)) can be closely predicted theoretically using the two band model [21], which assumes the transition occurs between free-electron like bands.

$$E(k_{\|}) = E_o + (\hbar^2 k^2/2m) \tag{3.16}$$

This approach has been considered by several authors for photoemission studies [27, 28, 29], and has been applied to the case of inverse photoemission [4, 19, 21] predicting the $E_f(K_{\|})$ dispersion of sp-bulk states adequately .

3.1.3.3 Two band approximation

The two band approximation is based on the two plane waves $\exp(i\vec{k}.\vec{r})$ and $\exp[i(\vec{k}+\vec{G}).\vec{r}]$, $\vec{G}$ being an appropriate reciprocal lattice vector. Let V_G represent the pseudopotential coefficient through which the two waves interact, then

$$V(r) = V_G \left[\exp(i\vec{G}.\vec{r}) + \exp(-i\vec{G}.\vec{r})\right] \tag{3.17}$$

Using the trial solution (eqn(3.18))

$$\psi_{trial}(r) = a\exp(i\vec{k}.\vec{r}) + b\exp\left[i(\vec{k}+\vec{G}).\vec{r}\right] \tag{3.18}$$

the following matrix equation can then be obtained

$$\begin{pmatrix} (\hbar^2k^2/2m) - E & V_G \\ V_G & \left[\hbar^2(\vec{k}+\vec{G})^2)m\right] - E \end{pmatrix} \times \begin{pmatrix} a \\ b \end{pmatrix} = 0 \tag{3.19}$$

This equation(3.19) has a solution when the secular determinant is zero, see

eqn(3.20)

$$\left(\frac{\hbar^2 k^2}{2m} - E\right)\left[\frac{\hbar^2(\vec{k}+\vec{G})^2}{2m} - E\right] - V_G^2 = 0 \tag{3.20}$$

Writing $E_{\vec{k}} = \hbar^2 k^2/2m$ and $E_{\vec{k}+\vec{G}} = \hbar^2(\vec{k}+\vec{G})^2/2m$ (free electron dispersion) we obtain the solutions

$$2E_i(\vec{k}) = (E_{\vec{k}+\vec{G}} + E_{\vec{k}}) + \left[(E_{\vec{k}+\vec{G}} - E_{\vec{k}})^2 + 4V_G^2\right]^{1/2} \tag{3.21}$$

and

$$2E_f(\vec{k}) = (E_{\vec{k}+\vec{G}} + E_{\vec{k}}) - \left[(E_{\vec{k}+\vec{G}} - E_{\vec{k}})^2 + 4V_G^2\right]^{1/2} \tag{3.22}$$

The isochromat surface previously mentioned (eqn(3.15)), can then be determined, giving the following plane in $\vec{k}$ space

$$(\hbar^2/m)\vec{k}\cdot\vec{G} = \left[(\hbar\omega)^2 - 4V_G^2\right]^{1/2} - E_G \tag{3.23}$$

where $E_G = \hbar^2 G^2/2m$. Contours of constant E_i or E_f form circles on the isochromat plane from the cylindrical symmetry about the direction of $\vec{G}$, shown in Fig(3.7). To obtain the dispersion of the final energy E_f in terms of the the component of $\vec{k}$ in the isochromat plane (i.e $k_{||}$), the simultaneous equations (3.22 and 3.23), are solved leaving the relationship eqn(3.24)

$$E_f(k_{||}) = \hbar^2 k_{||}^2/2m + \left[(E_G - \hbar\omega)^2 - 4V_G^2\right]/4E_G \tag{3.24}$$

This approximation to the $E_f(\vec{k_{||}})$ dispersion is free-electron-like, in agreement with experiment [21]. For constant E_i and E_f, the electron states are distributed around a cone (the axis of which is in the direction of $\vec{G}$) [29].

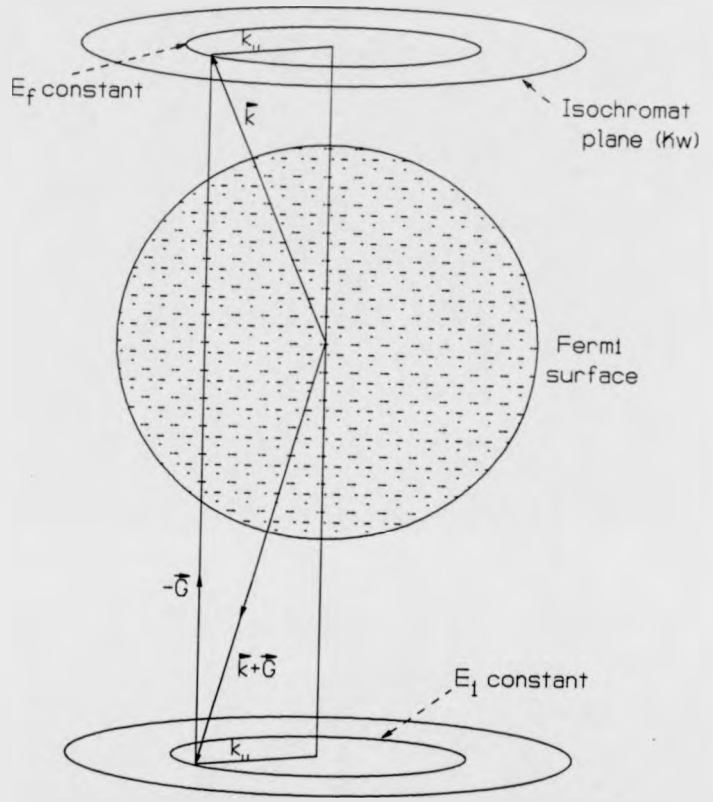

Fig 3.7:Geometry of the two-band approximation. Electrons of energy E_i decay through a direct transition emitting a photon of energy $\hbar\omega$ with the exchange of reciprocal lattice vector $-\vec{G}$ in the process.

3.1.3.4 k-space location techniques

Although it is possible using the two-band model to obtain values of $k_\perp$ when dealing with free-electron-like bulk states, different methods are necessary when generalising the problem for k-space location of other states. For example, the information obtainable from Fig(3.5) does not disclose the three-dimensional E(k) information, only the location in $k_{||}$. In order to determine the k-space location, information from more than one experiment is necessary to obtain the unknown momentum component $k_\perp$. One location technique which was originally proposed by Kane [30] involves the use of triangulation or energy coincidence using two independent measurements of an interband transition from two differently orientated surfaces [7]. Using this approach, two momenta $k_{||}$ are obtained with respect to the two different surface normals for the same point in k-space. Generally when using this approach, the technique of k-space location using the nearly free electron initial state approximation is first used to roughly identify the three-dimensional k-space location [31].

3.1.4 Surface states

The electronic structure at the surface of a solid will show a variation from that of the bulk due to the very different environment in this region. The coordination number of atoms at the surface, for example, will be much less than that of the bulk atoms, and together with changes to bond lengths (in atomic relaxation) and reconstructed atomic layers can cause the appearance of surface states that have wavefunctions that are not periodic in the direction normal to the surface.

The bulk states are still visible in the surface region, undergoing reflection at the vacuum barrier. The surface states occur in regions of $E(K)$ space where no bulk states of the same symmetry or quantum number are allowed to exist (i.e. in the band gaps). The surface resonance that can often occur in the bulk band, as a result of the mixing of surface and bulk state wave functions, is generally viewed as a modification of the bulk state near the surface [32, 34].

Since the KRIPES technique is very surface sensitive (probing only the first few atomic layers of the solid) the resulting spectra yield information not only on the dispersion of the bulk states, but also on the dispersion and character of the surface states. The surface states that are visible with ARPES are similar in character to the surface state in Fig(3.5) near the Fermi level (indeed this same state is seen (occupied) in ARPES very close to the Brillouin zone centre) [7, 33]. The second surface state close to the vacuum level in Fig(3.5) has no counterpart in ordinary photoemission and is known as an image state [35, 36, 37]. The wavefunctions of these states at the solid/vacuum interface are depicted in Fig(3.8)

3.1.4.1 Tamm states

These are usually d-like in character, having atomic like localisation of their wavefunctions [38]. Their origin can be visualised as a band bending effect, with the state being split off from the bulk bands into the band gap due to the surface potential [19].

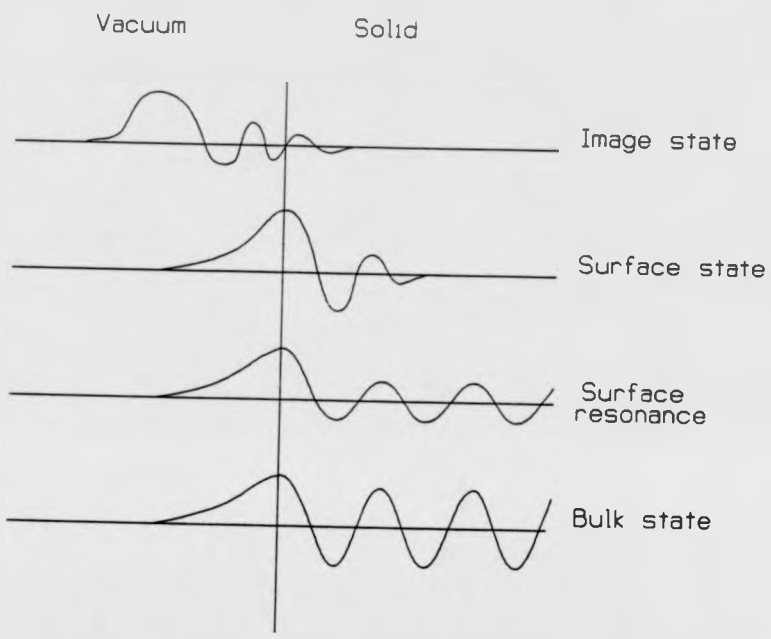

Figure 3.8: Schematic representation of the wave functions of final states involved in inverse photoemission transitions.

Tamm states can be observed in transition metals [39] and in semiconductors (for example, the dangling bonds in Si(100)) [5], and have been linked with the driving force behind surface reconstruction [40].

3.1.4.2 Shockley states

These sp-like surface states are far more free-electron-like in character and occur due to the new boundary conditions introduced by the surface [41]. The energies of these states occur within a bulk band gap which is the result of hybridisation of crossed bands (i.e the upper band edge has s-symmetry and the lower p-symmetry) the Shockley states extend generally deeper into the solid than the Tamm states, but similarly decay exponentially into the vacuum.

3.1.4.3 Image states

A great deal of attention has been paid to the image state effect, both theoretically [4, 35, 42, 43, 44] and experimentally [4, 45]-[49] since they were first observed using LEED (McRae [36]). They occur as a result of the self trapping of an electron in its own image potential induced by the electron approaching a conductive surface. The electron becomes trapped (providing the crystal reflectivity is high as it is in a band gap), between the crystal barrier and the image potential surface barrier giving rise to a Rydberg type series of states converging on the vacuum level [35] The image states are pinned to the vacuum level with binding energies of less than 1 eV, and the most tightly bound states are located about 1 Å outside the surface [4, 48]. Adsorption on the surface can cause these states to be quenched [50], shifted [51, 49], or even in some cases enhanced [48]; shifts

induced by adsorption have sometimes been used as a rough measure of workfunction change [49]. The dispersion of image states is generally free-electron like with effective masses close to unity [46], although flatter dispersion has been observed [52, 53]. The lifetimes of these states are long compared to ordinary surface states having line widths of 20-80 meV [48]. The image potential states are most simply described using the multiple reflection approach [4, 16, 19, 35, 42, 43] which also predicts the Shockley states.

3.1.4.4 Multiple reflection theory

The multiple reflection approach was first applied to explain surface state occurrence by Echenique and Pendry [35]. The systematics of this model are portrayed in Fig.(3.9). An electron incident on the crystal will, in the energy range of a bulk band gap, be reflected by the crystal. If the electron has an energy below the vacuum level E_V, it will be reflected back towards the crystal by the surface potential barrier. In Fig.(3.9), the crystal is terminated at $Z = Z_C$, with Z being the direction perpendicular to the surface. The surface potential barrier is defined at $Z = Z_B$, and between the two barriers the potential is flat with electrons propagating freely. In this region, the motion perpendicular to the surface (Z direction) is characterised by a "perpendicular energy" $E_\perp$, and is defined in eqn(3.25).

$$E_\perp \equiv \frac{\hbar^2 k_\perp^2}{2m} \equiv E - \frac{\hbar^2 k_\parallel^2}{2m} \qquad (3.25)$$

E is the energy of the electron measured from the bottom of the potential well.

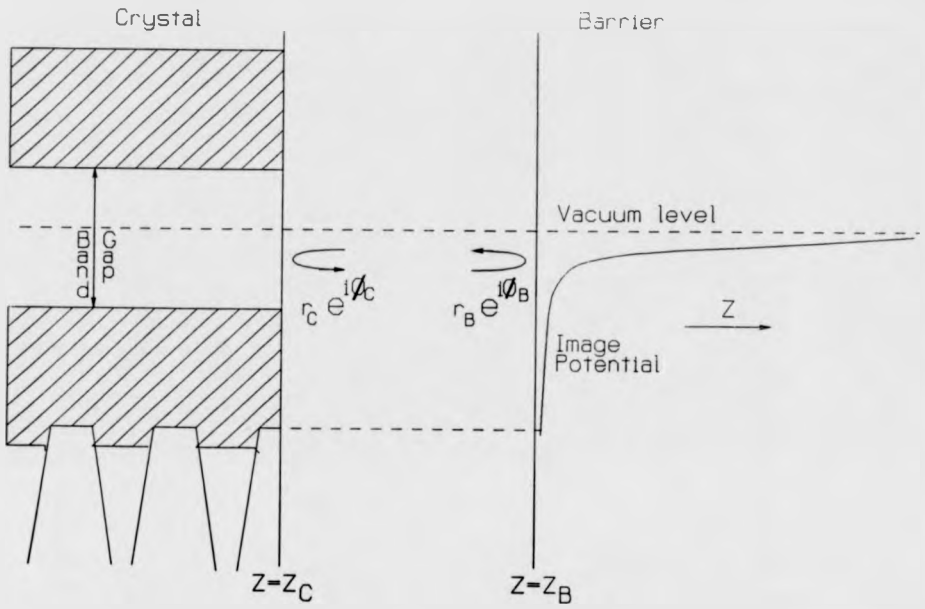

Fig 3.9:Multiple-reflection model for surface state formation. Z is defined as the direction perpendicular to the surface, the diagram showing the Z-dependence of the electron potential near the crystal surface. The crystal is taken to end at Z_C, with the surface barrier reference plane at Z_B. Surface states arise through multiple reflections between these two planes (and hence are standing wave solutions between Z_C and Z_B).

At the planes Z_C and Z_B, the reflectances are given by $r_C \exp^{i\phi_C}$ and $r_B \exp^{i\phi_B}$ respectively, with the conditions for a bound state being that $r_C = r_B = 1$ and

$$\phi = \phi_C + \phi_B = 2\pi n \tag{3.26}$$

where n is an integer.

Consider now the phase dependencies at the barriers.

(i) Barrier phase change ϕ_B

The phase change at Z_B is determined by the shape of the barrier. For a pure image potential, the barrier phase change will be a simple function of $E_\perp$ and E_V:

$$\phi_B/\pi = \left[\frac{3.4eV}{E_V - E_\perp}\right]^{1/2} - 1 \tag{3.27}$$

On approaching E_V, the phase diverges as $(E_V - E_\perp)^{-1/2}$. If however, an abrupt step potential barrier is assumed, then the form of ϕ_B becomes:

$$\tan(\phi_B/2) = -\left[(E_V - E_\perp)/E_\perp\right]^{1/2} \tag{3.28}$$

In this case, ϕ_B varies as $(E_V - E_\perp)^{1/2}$. The phase divergence associated with the image potential form, allows eqn(3.26) to be satisfied *ad infinitum*, so generating a Rydberg series of states that converge on E_V. The step barrier case does not generate the image state solutions, but does define the crystal induced state (or shockley surface state) which corresponds to the '$n = 0$' solution in the image potential barrier case is not so for the step barrier, with the '$n = 0$' solution being the only possible solution [4].

(ii) Crystal phase change ϕ_C

Since the '$n = 1$' and higher (image state) solutions are compressed into a narrow energy range, ϕ_C is generally treated as constant for the purposes of calculating these states [6] (although the total phase change across the band gap is π). Therefore, over the range of the Rydberg series, the image state energies (e_n) are given by:

$$E = E_V - e_n + \frac{\hbar^2 k_{||}^2}{2m} \tag{3.29}$$

where

$$e_n = \frac{1}{16[(n+a)^2]}.Ry. = \frac{0.85}{(n+a)^2}eV. \tag{3.30}$$

it follows that the quantum defect 'a' is also constant since

$$a = \frac{1}{2}\left(1 - \frac{\phi_C}{\pi}\right) \tag{3.31}$$

3.1.5 Discrimination of bulk and surface features

There are several methods employed in order to determine whether a feature observed in an IPE spectra is derived from bulk or surface electronic structure effects.

3.1.5.1 Adsorption test

Generally the surface derived features are a great deal more sensitive to surface contamination than the bulk features. By observing the changes in the spectra over a period of time after cleaning, or by observing the effects of deliberate adsorption of a contaminant, it is possible then to draw inferences as to the

origin of a feature [4]. This is not a foolproof test however, as mentioned in section(3.1.4.3) for example, image states have been shown to be enhanced by certain adsorbates on some surfaces [48].

3.1.5.2 Temperature increase

Although electron-phonon scattering is quasi-elastic, there is generally an electron momentum change associated with the interaction. These interactions therefore have the effect of randomising the momentum and hence attenuating the direct transition features, the higher the temperature means more interaction and greater attenuation [54].

3.1.5.3 $k_\perp$ dispersion

A much more definitive technique [4, 19, 34] is available if the isochromat energy is tunable. Surface features show two-dimensional dispersion parallel to the surface ($k_{||}$ conserved) with no dispersion perpendicular to the surface ($k_\perp$ not conserved). If $k_\perp$ is varied at normal incidence (i.e the isochromat energy is changed), then the $E_f(k_{||})$ relation of surface states will be unaffected. For bulk states however, which show dispersion perpendicular to the surface (hence $k_\perp$ conserved) the $E_f(k_{||})$ dispersion will be shifted energetically [34]. This energy shift can be utilised to study some surface features that may possibly be hidden at one isochromat energy by a bulk feature, but may be observable when the bulk feature is shifted at a different isochromat energy [34]. This effect can be seen in Fig(3.5b), where the bulk state (BB) dispersion is plotted at three isochromat energies.

3.2 KRIPES experimental system

The KRIPES experiments reported here have been conducted in a non-magnetic stainless steel ultra-high vacuum (UHV) chamber, equipped with Helmholtz coils to cancel the effect of the Earth's magnetic field. The chamber geometry, analytical instrumentation and crystal cleaning procedures are described in this section, together with the specifications of the KRIPES source and detection system.

3.2.1 UHV

In an experiment that is very surface specific, it is extremely important that over the period of study the surface conditions are exactly controlled. For example in the case of an experiment on a clean well ordered surface at $\approx 10^{-9}$ torr, it is possible to form a monolayer of CO in one hour assuming a unity sticking factor [7]. In order to maintain a clean surface in practice (contamination of no more than a few percent of a monolayer) over this same time period, a working pressure of $< 3 \times 10^{-10}$ torr is necessary. To obtain these UHV conditions, the KRIPES chamber has a combination of pumping systems. The main chamber is pumped by a polyphenyl ether diffusion pump (Edwards EO4) backed by a two stage rotary pump (Edwards two stage) fitted with a molecular sieve trap, which is also used to rough the chamber on initial pumping from atmospheric pressure. A small (50 l/sec) ion pump (Varian triode) is situated above the detector section of the chamber, and a titanium sublimation pump is located near the base of the main cylindrical experimental chamber that houses the sample mounted on a manipulator. The gas lines (both reactive and unreactive) are pumped by

a smaller polyphenyl ether diffusion pump (Edwards EO2) backed by a trapped rotary pump (Edwards EDM2). At these low pressures, gas molecules (H_2O, CO etc) desorbing from the internal walls of the chamber are a limiting factor determining the maximum vacuum attainable. To reduce these contaminants, the the chamber is 'baked' (i.e. heated to temperatures greater than 450K) for more than 12 hours to greatly increase the rate of desorption. In addition, a cold trap located above the main diffusion pump is filled with liquid nitrogen (77K) in order to provide a cold surface to trap residual water and hydrocarbons together with other low molecular weight contaminants from the pump, hence decreasing the attainable pressure still further and reducing the level of reactive gas species.

3.2.2 KRIPES chamber geometry

The top view of the KRIPES chamber is shown in Fig(3.10). At one end of the chamber is the cylindrical multi-level chamber that houses the sample manipulator, electron guns and various analysis instrumentation. Fig(3.11a) shows a side view and has been separated into five levels for simplicity (Fig(3.10) shows the top view of level 2). The other end of the system seen in Fig(3.10) consists of the LiF lens and isochromat detector housing, this being connected to the sample chamber by a stainless steel bellows.

Level 1 houses an ion gun (VG Scientific AG2) used for sample cleaning and is positioned at an incident angle of 25° with respect to the horizontal plane in which crystal surface normal can be swept. An Argon line with leak valve is connected to the ion gun flange. See Fig(3.11b).

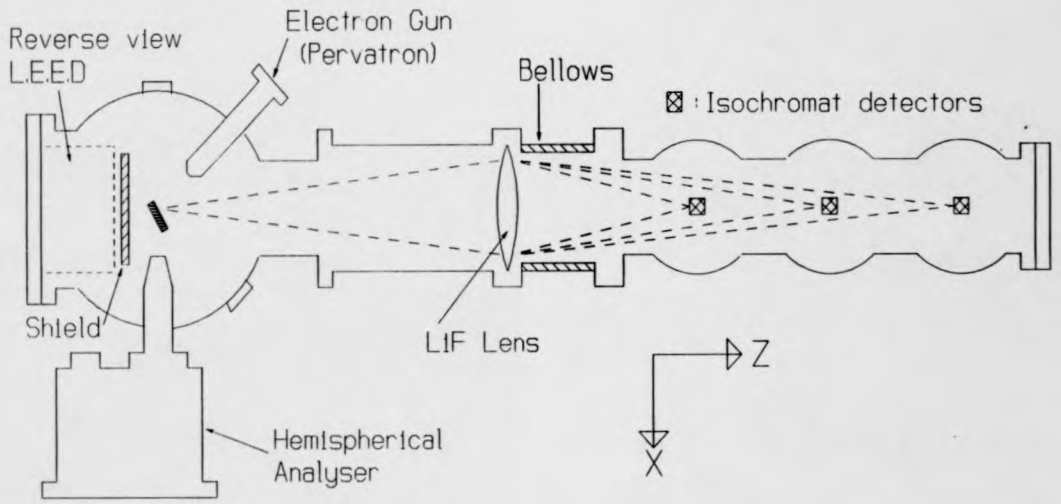

Fig **3.10**:Schematic of KRIPES chamber showing low energy, high perveance electron gun together with detector assembly. This diagram corresponds to level 2 of the chamber.

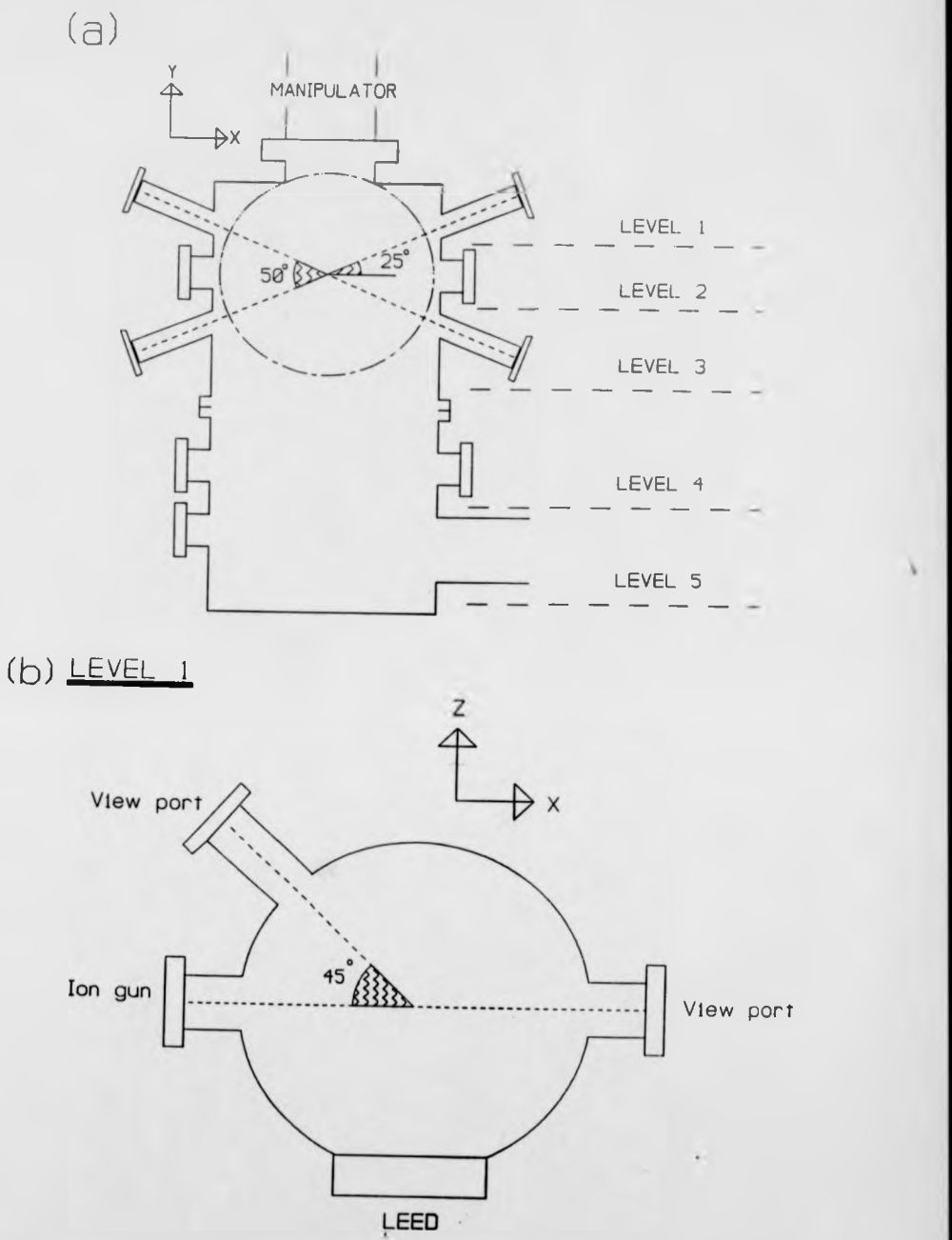

Fig 3.11:(a) View of chamber from LEED optics end, showing the series of levels of the main chamber. **(b)** Plan of level 1.

Level 2 comprises of a high perveance low energy electron ('pervatron') gun mounted at an angle of 45° to the optical axis of the photon detectors, and a hemispherical analyser (VSW HA50) used for Auger electron spectroscopy is located in the X-axis, directly opposite a viewport (used to aid detector-sample alignment). Also in the optical axis, opposite the LiF lens are the reverse view low energy electron diffraction (LEED) optics (Omicron Spectaleed optics). See Fig(3.12a).

Level 3 houses a high energy electron gun providing electron energies up to $4keV$ for use in Auger electron spectroscopy (AES), and is positioned at an angle of 25° to the horizontal axis of the hemispherical analyser above it, see Fig(3.12b).

A mass spectrometer (VG Q7 quadrupole residual gas analyser) is positioned 'out of line of sight' of the chamber in the Z-axis port in level 4 (shown in Fig(3.13a)). An ion gauge and reactive gas line leak valve are also on this level together with the shield control (to raise and lower a metal shield over the LEED optics during crystal cleaning).

In level 5, the titanium sublimation pump (TSP) and roughing valve to the rotary pump are located. In the X-axis is the outlet to the main diffusion pump and cold trap, see Fig(3.13b).

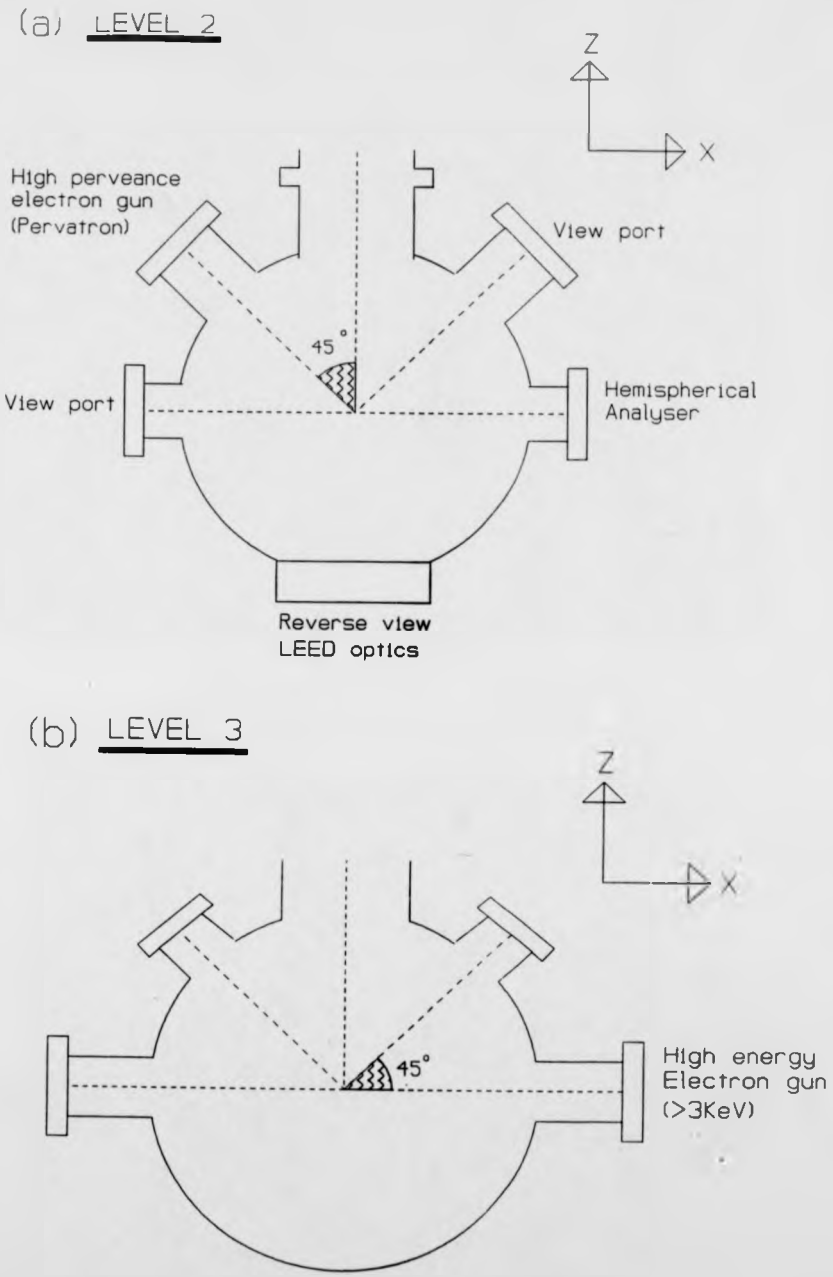

Fig 3.12:(a) Plan of level 2, and (b) level 3.

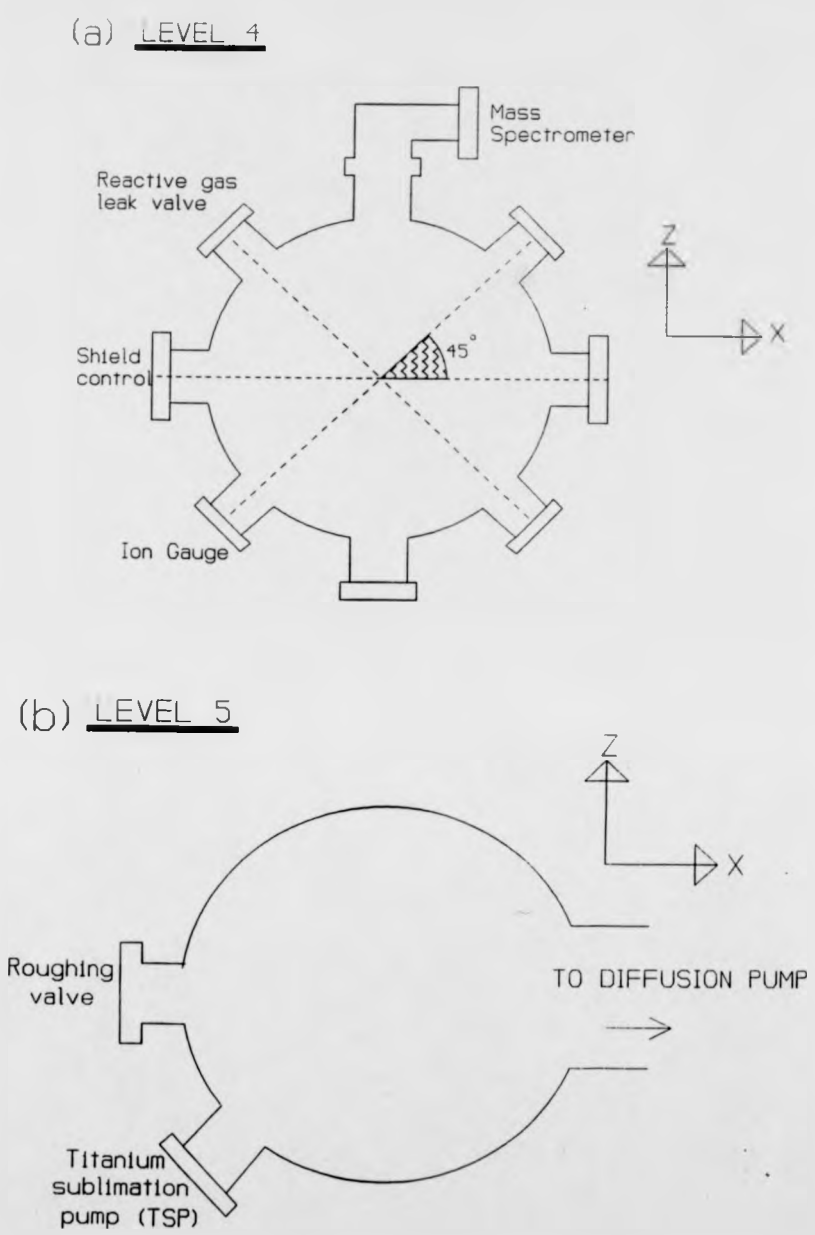

Fig 3.13:(a) Plan of level 4, and (b) level 5.

3.2.3 Sample mounting, manipulation and cleaning processes

3.2.2.1 Manipulator

The manipulator used (VG HPT 040) has drives in the Z, X and Y axis, and has four mini-Conflat ports fitted with two high voltage feedthroughs and two ports for thermocouple and Faraday cup connections. The crystal samples have grooves cut at the top and bottom in which 0.125 mm diameter tungsten wires run, the ends being spot welded to the supporting rods (see Fig(3.14)). The thermocouple wire is connected directly through a hole in the sample to which it is hooked. Above the sample is located a Faraday cup with pin hole aperture ($1mm$ diameter) for use in obtaining beam profiles of the 'pervatron' gun (see section(3.2.6.5)).

3.2.2.2 Sample cleaning

The crystal sample can be cleaned *in situ* using cycles of argon ion sputtering and annealing. The process of sputtering directly removes atoms from the surface via collisions, the energy of the ions used depending on the crystal (typically $0.5keV \rightarrow 3keV$). The process of annealing (being conducted by direct resistive heating through the tungsten wires) is then used to anneal the sample and restore the periodicity of the crystal surface, with the maximum temperature attainable being approximately 1100K. Prior to mounting on the manipulator, the crystals were prepared by the standard process of spark eroding and alignment using Laue X-ray diffraction.

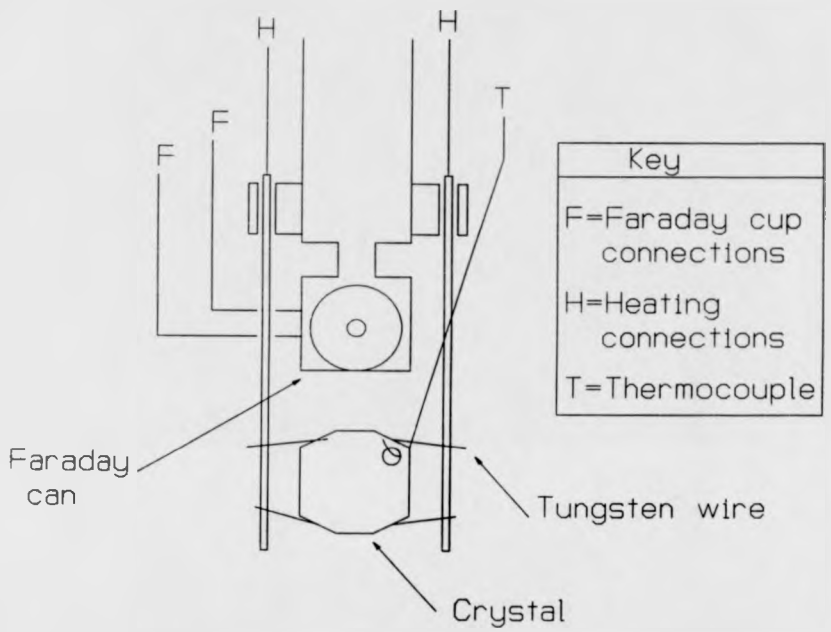

Fig 3.14:KRIPES manipulator head arrangement, with the Faraday cup located 1 cm above the crystal.

3.2.4 Magnetic field cancellation

Magnetic field cancellation is achieved by using a three directional field probe connected to a gaussmeter (Bell 640 incremental gaussmeter) to assess the field strength. The probe is first zeroed in a field free container, then placed through the manipulator port to locate it in the normal sample position. The voltages applied to the three Helmholtz coils are adjusted to achieve as near to zero field strength as is possible in the three probe directions. This countering of the Earth's magnetic field (and any other stray fields) in the chamber is vital, considering the low energy of the electrons ($5 \rightarrow 30eV$) used and the emphasis on k-determination.

3.2.5 General analytical techniques

3.2.5.1 Low energy electron diffraction, LEED

The theory of this technique together with the geometry of the LEED optics has already been detailed in chapter 2. The LEED instrument is used to characterise the long range order of the surface of the crystal after cleaning and prior to a KRIPES study. In addition, it is often the case that due to the varying geometry of other UHV systems, the exposure required to achieve certain adsorbate structures varies and simple recipes from earlier publications cannot be relied on [49, 56]. The LEED pattern provides a definite *in situ* method of determining if the required surface phase has been achieved. During crystal cleaning cycles, the LEED optics are protected by raising a metallic shield.

3.2.5.2 Auger electron spectroscopy, AES

The theory of AES is described in section(2.1), and the technique was used in the present work to determine the state of cleanness of the crystal surface. An electron gun is used to ionise atoms in the surface of the crystal, and a hemispherical analyser (VSW HA50) was used to analyse the intensity vs energy distribution of the Auger electrons. The crystal potential is modulated and the monitored signal differentiated to obtain the Auger spectrum in the usual derivative form. The ratio of the peak heights of the various contaminants to the main peak corresponding to the crystal substrate species was used as a guide to the state of cleanness of the surface, and was checked after the cleaning cycles. During experiments involving chemisorption, AES together with LEED were used to check whether the desired surface phase had been obtained.

3.2.6 KRIPES electron gun specifications

The electron gun used is based on a design by Stoffel and Johnson for a high perveance, low energy electron gun (pervatron) [55].

3.2.6.1 Gun geometry

The gun lens arrangement is shown in Fig(3.15) with the copper lenses separated by ceramic spacers. Fig(3.16) shows in more detail the mounting of the BaO cathode. At the energies at which the gun is designed to operate ($5 \rightarrow 25eV$), the maximum possible crystal current obtainable before being limited by space charge effects is determined not by the cathode source, but by the refocusing

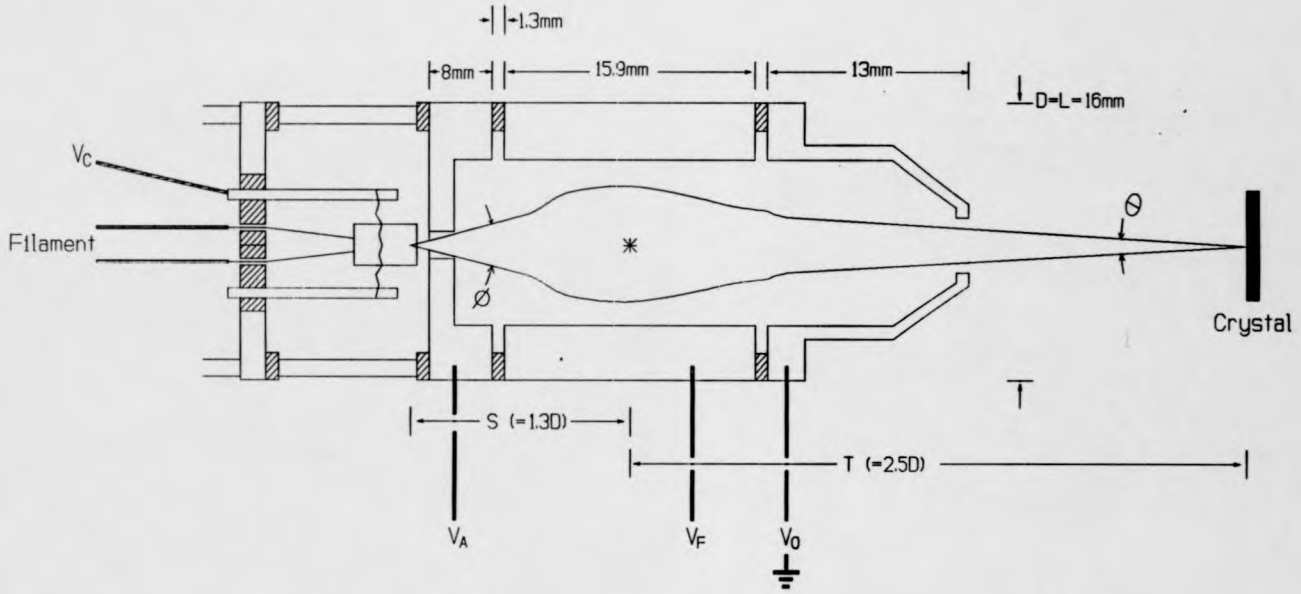

Fig **3.15**:High perveance, low energy electron gun (pervatron) [55]. The shaded areas represent the insulating ceramics.

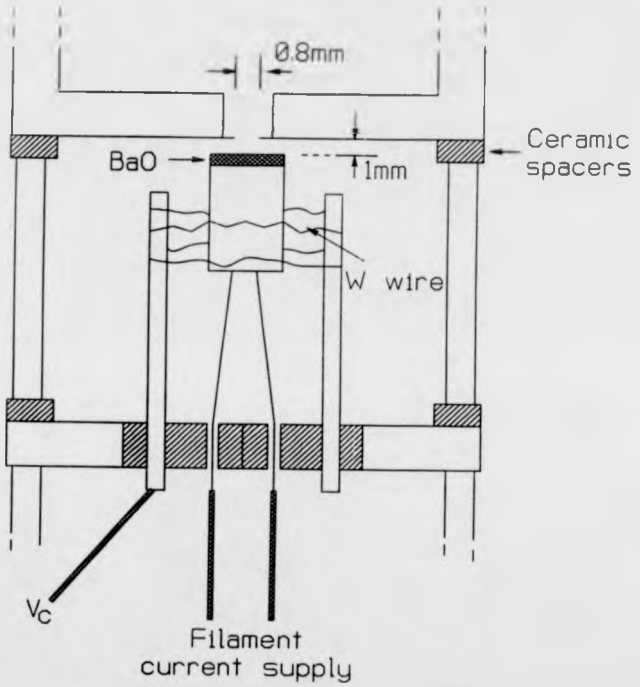

Fig 3.16:Geometry of cathode section of pervatron.

-stage of the gun [55, 57]. From the lens calculations of Harting and Read [58], the spherical aberration coefficient can be reduced if the gun is tubular in design with the focus lens length equal to the diameter of the gun ($D = L = 1.59cm$). The gun is designed to focus the electron beam between $0 \rightarrow 3cm$ from the last lens, the crystal usually being placed at a distance of approximately $2cm$ to allow some focusing range and correction for crystal movement. The cathode section of the gun is surrounded by a copper sheath, allowing emission only along the axis of the gun.

3.2.6.2 BaO cathode

The cathode material used is barium oxide impregnated with Osmium ('M' type, manufactured by Spectra-Mat Inc.). The cathode is thermally activated by a potted internal filament, the current to which is controlled by the gun supply unit. Due to the high temperatures at which the cathode operates (maximum temperature $\approx 1350K$), the stabilising of the gun including thorough outgassing of the assembly after exposure to atmosphere takes greater than a week of constant running. This is due to the high local pressures created at the cathode section and also to the degassing of the copper lenses. Typically, once stabilised the activation was achieved after approximately $5 - 10mins$ at a filament current of $I_H = 1.2A$. After this, the cathode was operated at a filament current of $I_H = 0.75 \rightarrow 0.8A$ for optimum focusing conditions with negligible space charge effects. The cathode is supported by tungsten wire (one of the few metals that does not cause contamination of the BaO cathode emission) that is spot-welded

to stainless steel screws on either side (see fig(3.16)). The cathode is biased via an electrical connection to one screw by a voltage V_C, which determines the kinetic energy of the emitted electrons. The cathode is separated from the anode aperture by $1mm$ with the diameter of the aperture being $0.8mm$, the anode aperture acting as a diverging lens with a focal length of three times the anode-cathode separation.

3.2.6.3 Gun supply characteristics

The gun supply unit is interfaced to a computer (Cambridge workstation) via a AD/DA interface unit (CUBE. Control Universal Ltd.). The computer is used to calibrating the supply (supplying $0 \rightarrow 10volts$) and to ramp the lens voltages. After initial calibration (see section(3.2.6.4)), the focus voltage (V_F) can still be varied manually; once the gun is focused, V_F maintains a constant ratio to V_C as the anode and cathode voltages are varied. Focusing of the gun occurs at approximately $V_F \approx 3/5V_C$, where $V_C \approx 1/6V_A$; the ratio of the anode-cathode voltage can also be adjusted on initial calibration. The schematic diagram of the circuit is shown in Fig(3.17). A work function offset supply is used to compensate for the difference between the low work function of the BaO cathode and the gun lenses. This offset value is typically between $1 \rightarrow 2V$, and is necessary to maintain the correct voltage ratios when ramping the gun at low energies. Without this offset, incorrect voltage ratios would have a defocusing effect limiting performance.

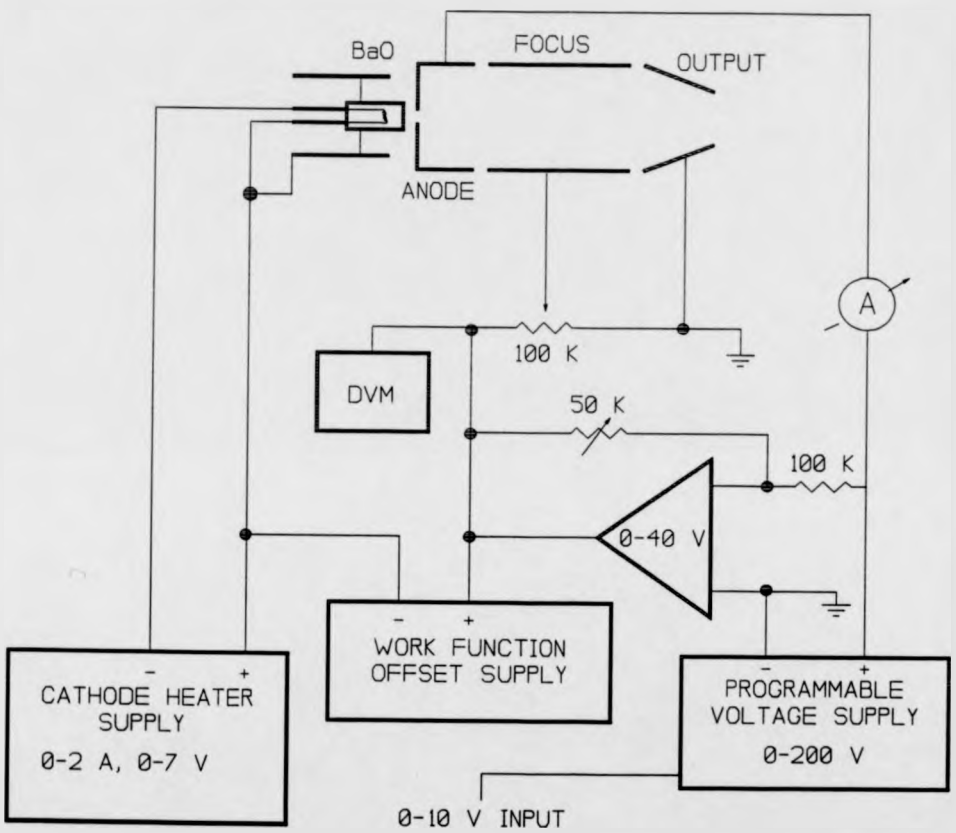

Fig 3.17:Circuit plan for pervatron.

3.2.6.4 Gun calibration and operation

As mentioned briefly in section(3.2.6.2), there is some considerable time involved in outgassing the electron gun when the chamber has been open to atmosphere. Following this outgassing, the BaO cathode was fully activated by setting the filament current at approximately $1.2A$ for five to ten minutes. After this time, the filament current was reduced (to $\approx 0.8A$) with emission stabilising after approximately ten minutes. On initial calibration, the computer sets the input voltage to the supply at zero volts, setting to zero V_C, V_F and V_A in the process. At this stage it is possible to vary the work function offset voltage, with this value input in the computer as the cathode voltage. For the second stage of the calibration, the computer sets the input voltage to the supply at 10 volts. The anode voltage is directly linked to the input voltage set by the computer, with $V_A = 196$V at 10V input. The cathode voltage was manually adjusted to $V_C \approx 1/6 V_A \approx 31$V, the cathode/anode voltage ratio being defined and stipulated by the gun geometry. This cathode voltage was then input in the computer as the maximum cathode voltage. If the program is then set to ramp the cathode voltage between two values (i.e in the range: workfn.offset $< V_C < 31V$), the anode voltage will also ramp, hence maintaining a constant ratio with cathode voltage.

3.2.6.5 Focusing and beam profile measurement

Once calibrated, it is necessary to vary the focus voltage in order to focus the electron beam on the sample. Since the detection system is optical in design

(relying on the focusing abilities of the LiF lens), and the angle of incidence of the electrons at the sample surface needs to be well defined. the spectral and $k_{||}$ resolution of the experiment are both determined by the gun focussing conditions. The energy resolution of the lens being determined by the size of the focus, and the $k_{||}$ resolution is determined by the parallelism of the incident electrons. In order to obtain the optimum focus, the beam profile needs to be monitored constantly using the Faraday cup located above the crystal sample on the manipulator. The cup has a pinhole aperture ($1mm$ diameter), and the current arriving at the back of the cup is measured via a picoammeter. The pinhole aperture is located in the center of a $1cm$ square face, from which the current is also monitored (this provides a close match to the crystal current produced if the crystal were to be moved in line with the gun). The cathode voltage is held constant (e.g 10 V) and the electron gun focused to obtain a maximum current through the pinhole. The beam profile can then be measured by moving the Faraday cup in x, y and z directions. This procedure is repeated while decreasing the cathode emission in order to obtain the optimum focus and beam current. These conditions are generally met when the cathode has low emission (typically when the current measured from the anode is less than $0.7mA$). Fig(3.18) shows the beam profile for a kinetic energy of 10eV together with the voltages at which the profile was measured. Once the finest focus is achieved, the gun voltages maintain the same ratio with respect to each other as the energy of the gun (i.e cathode voltage) is ramped. The beam current increases rapidly between $3eV$ and approximately $5eV$ before flattening over the energy range of interest, see Fig(3.19).

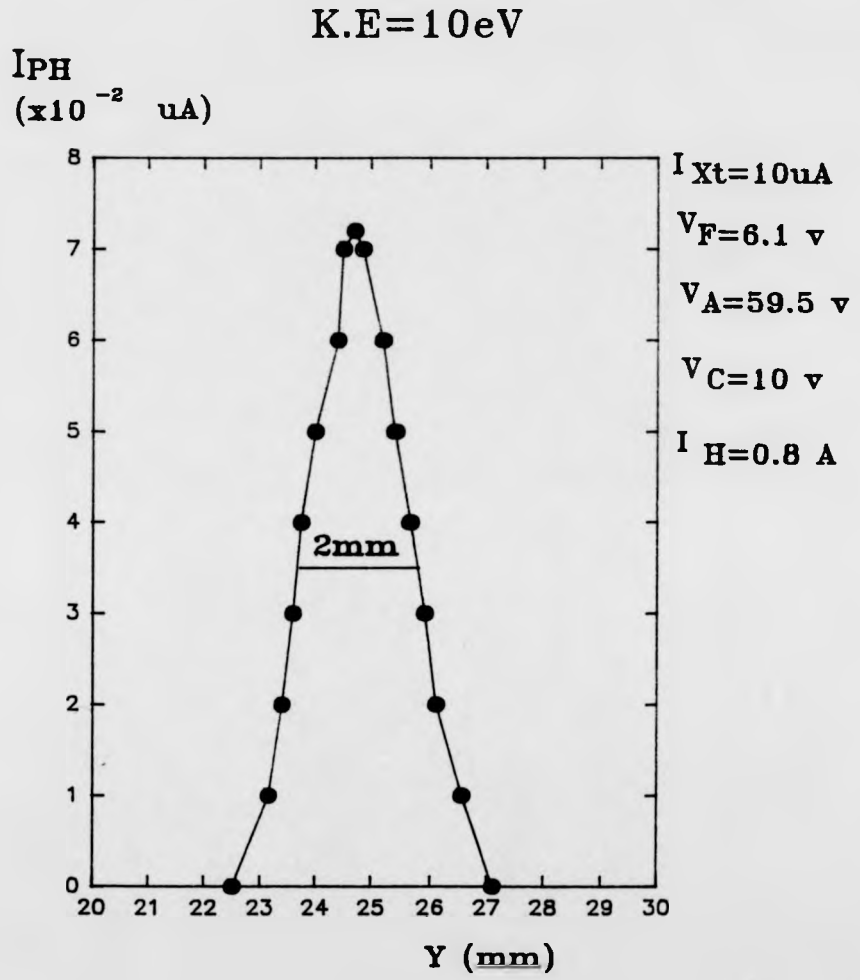

Fig 3.18:Beam profile from pervatron, measured with pin-hole (1mm diam.) Faraday cup. Full width at half maximum is approximately 2 mm.

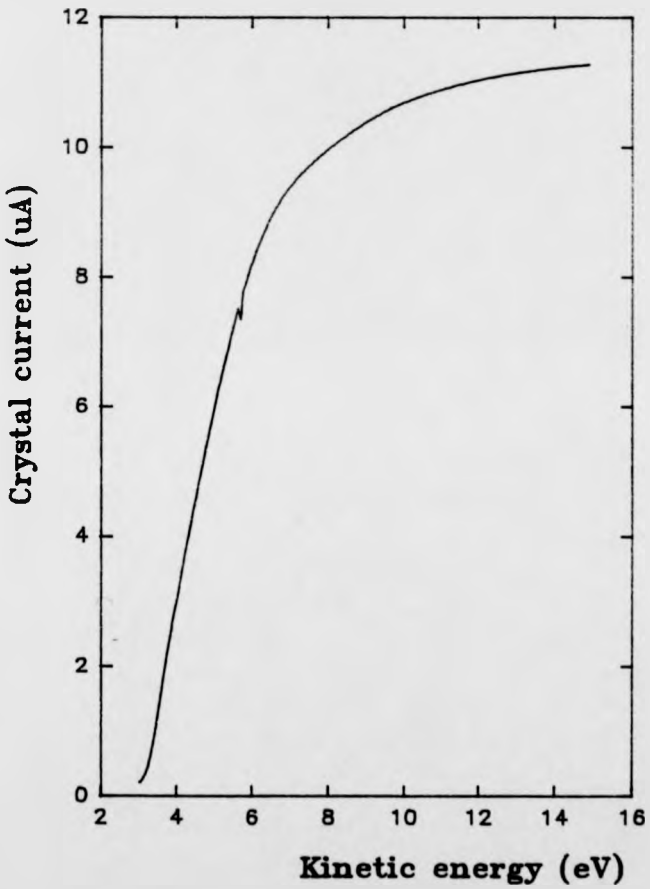

Fig **3.19**:Plot of crystal current (μA) vs kinetic energy (eV), following gun focussing at $10eV$ kinetic energy.

3.2.7 Isochromat detector instrumentation

Photons emitted from the crystal sample during the inverse photoemission process are focused as a function of their wavelength along the Z-axis by a LiF lens [59, 60, 61]. Three isochromat detectors are placed along this axis, whereby three different photon energies can be detected. Although these detectors are fixed relative to each other (210mm spacings) with detection energies of (a)front (nearest the LiF lens) 11.5 eV, (b)middle 10 eV and (c)back 8.5 eV, the bellows next to the LiF lens allow the movement of the whole detector assembly which permits a possible ± 0.5 eV shift about mean values for the three isochromat energies [59]. The detectors each consist of an aluminium alloy box (Fig(3.20)) with a 5mm diameter aperture. A CsI-coated steel plate is placed behind the aperture to photoemit electrons at a rate proportional to the photon intensity. The CsI plate is angled to the aperture, and to a channel electron multiplier (channeltron) which is used to detect the photoelectrons. The channeltron is insulated from the detector casing by polytetrafluoroethylene (PTFE) and the aluminium box is biased to repel any electrons arising from secondary electron emission from the sample or photoelectron conversion produced at the chamber walls. Each channeltron has its own single channel amplifier and discriminator electronics feeding into a seperate counter channel of the computer (Cambridge workstation) which is also used to control the electron gun. The detectors are each mounted on a linear wobble drive fixed to a 150mm diameter port at the side (X-axis) allowing movement during alignment, and since the cross-sectional area of the detectors visible to the lens is small, only approximately 10% of light

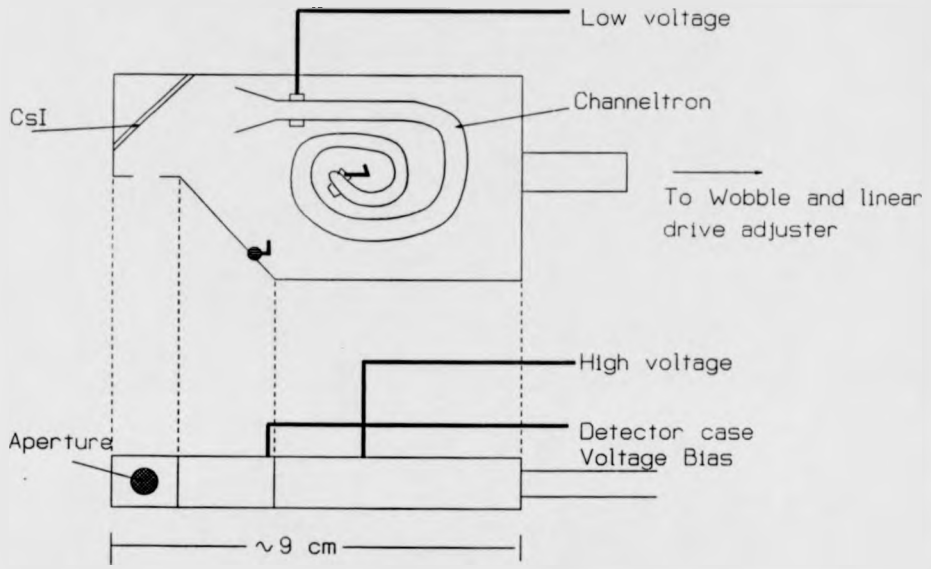

Fig 3.20:Isochromat detector schematic.

is shadowed by one detector at the next [59].

3.2.7.2 LiF lens

The LiF lens used is biconvex of total diameter $100mm$, with a stop positioned in the centre of the lens in order to prevent paraxial rays (of all energies) reaching the detectors [60, 61]. A small hole in the center of the stop is used for laser alignment purposes. LiF has a cut-off photon energy of 11.7 eV ($\lambda \approx 105nm$) and shows strong chromatic aberration below this value. The lens was cleaned using ethanol and has a transmission efficiency that is very sensitive to prolonged exposure to atmosphere.

3.2.7.3 CsI photoemitters

Cesium iodide (CsI) is used to convert the photons incident through the detector aperture into photoelectrons which can then be detected. CsI was used for its high quantum efficiency in the wavelength range at which the isochromats are recorded, and is often also used as a filter in Geiger-Müller and channelplate detectors for inverse photoemission [62, 63]. The CsI coating was obtained by the process of vacuum deposition from a tungsten boat at a pressure of $P \approx 1 \times 10^{-6}\tau$ at a temperature of $550K$ in a separate vacuum system. The CsI coating thickness was estimated to be approximately $1\mu m$, with a more compact surface achieved by the elevated temperature of the steel plate substrate during deposition. Great care was taken to keep the CsI plates in a vacuum as much as possible, since the quantum efficiency decreases quickly with exposure time to damp air (see fig(3.21) [62]). The quantum yield curve for CsI is shown in fig(3.22) [63].

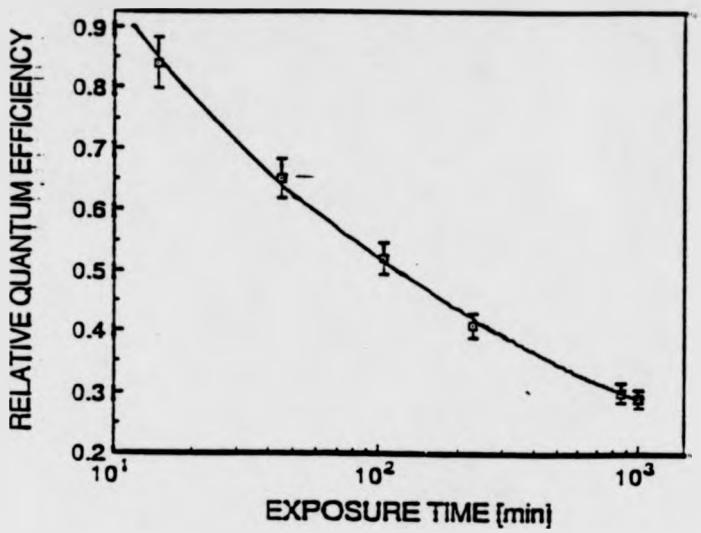

Fig **3.21**:Graph showing relative quantum efficiency of CsI against exposure time in air. [62]

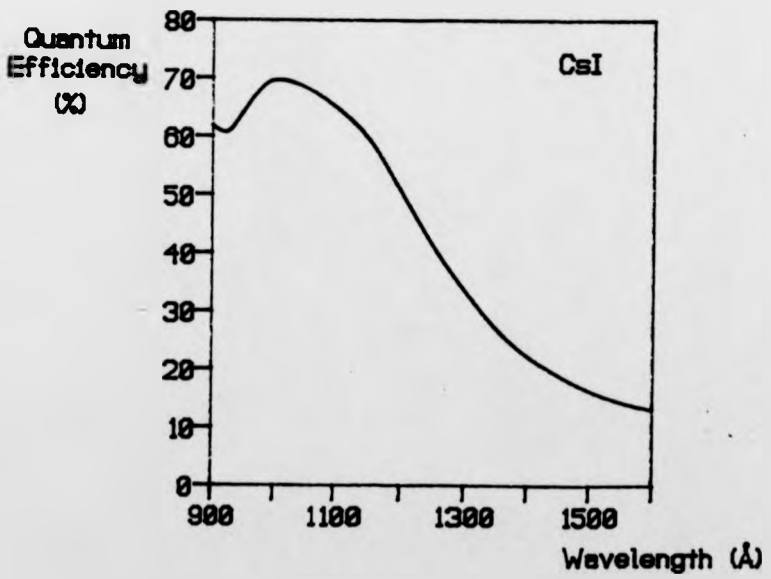

Fig **3.22**:Quantum efficiency of CsI versus wavelength [63]

3.2.7.4 Channel electron multipliers

The channel electron multipliers (Phillips X919BL), or channeltrons, convert the photoelectrons incident from the CsI into pulses by the process of secondary electron cascades. The pulses are fed via a single channel amplifier to the CUBE electronics (for counting) and finally to the computer for analysis.

3.2.7.5 Detector and crystal alignment

Alignment of the detectors and crystal was achieved using a HeNe laser operating in the visible red. The laser is aligned through the window at the end of the detector section, though the hole at the center of the LiF lens and onto the crystal sample. The crystal sample was rotated so that the laser light was reflected through the two side windows in the main chamber (level 2), one of the windows being on the HA50 analyser. Once the crystal has been centered, the laser was moved to one of the side windows of level 2, and the light reflected off the crystal through the center of the LiF lens and through the center of the end window. The positions of the detectors to block the light were then determined. Further fine changes to detector position were conducted in between initial test spectra to obtain the optimum resolution.

References

[1] A.Einstein, Ann. Phys. **17**, p132 (1905)

[2] W.Duane and F.L.Hunt, Phys. Rev.**6**, p166 (1915)

[3] D.P.Woodruff and N.V.Smith, Phys. Rev. Lett. **48**(4), p283 (1982)

[4] N.V.Smith and D.P.Woodruff, Prog. in Surface. Sci. **21**(4), p295 (1986)

[5] F.J.Himpsel, Surface. Sci. Rep. **12** p1-48 (1990)

[6] P.D.Johnson in *Angle-resolved Photoemission: theory and current applications* ed. S.D.Kevan (Elselvier, Amsterdam. 1992).

[7] D.P.Woodruff and T.A.Delchar, *Modern techniques of surface science* (Cambridge University Press, 1986)

[8] Th.Fauster and V.Dose in *Chemistry and Physics of solid surfaces vol.6* ed. R.vaneslow and R.Howe (Springer-verlag, 1986)

[9] J.E.Inglesfield and E.W.Plummer in *Angle-resolved Photoemissian: theory and current applications* ed. S.D.Kevan (Elselvier, Amsterdam. 1992)

[10] J.B.Pendry, J.Phys C **14**, p1381 (1981)

[11] J.B.Pendry, Surface. Sci **57**, p679 (???)

[12] I.Adawi, Phys. Rev. **A134**, p788 (1964)

[13] W.L.Schaich and N.W.Ashcroft, Phys. Rev. **B3**, p2452 (1971)

[14] G.D.Mahan, Phys. Rev. Lett. **24**, p1068 (1970)

[15] N.V.Smith and C.T.Chen, Surface. Sci. **247**, p133 (1991)

[16] G.Borstel and G.Thörner, Surface. Sci. Rep. **8**, p1 (1987)

[17] P.D.Johnson and J.W.Davenport, Phys. Rev. **B31**, p7521 (1985)

[18] W.Heitler, *The quantum theory of radiation* 3rd edition (Clarendon, Oxford. 1954)

[19] V.Dose, Surface. Sci. Rep. **5**, p337 (1985)

[20] D.P.Woodruff, P.D.Johnson and N.V.Smith, J. Vac. Sci. Technol. **A1**(2), P1104 (1983)

[21] D.P.Woodruff, N.V.Smith, P.D.Johnson and W.A.Royer, Phys. Rev. **B26**(6) p2943 (1982)

[22] P.D.Johnson and N.V.Smith, Phys. Rev. Lett. **49**(4), p290 (1982)

[23] N.V.Smith and D.P.Woodruff, Phys. Rev. **B25**(5), p3400 (1982)

[24] V.Dose and G.Reusing, Appl. Phys. **23**, p131 (1980)

[25] N.V.Smith, Applications of Surface Sci. **22/23**, p349 (1985)

[26] M.Donath, V.Dose, K.Ertl and U.Kolac, Phys. Rev. **B41**(9), p5509 (1990)

[27] N.V.Smith and W.E.Spicer, Phys. Rev. **188**, p593 (1969)

[28] R.Y.Koyama and N.V.Smith, Phys. Rev. **B2**, p3049 (1970)

[29] G.D.Mahan, Phys. Rev. **B2**, p4334 (1970)

[30] E.O.Kane, Phys. Rev. Lett. **12**, p97 (1967)

[31] F.J.Himpsel, Adv. Phys. **32**, p1 (1983)

[32] S.L.Hulbert, P.D.Johnson, M.Weinert and R.F.Garrett, Phys. Rev. **B33**, p760 (1986)

[33] A.Zangwill, *Physics at Surfaces* (Cambridge University Press. 1988)

[34] D.P.Woodruff, S.L.Hulbert, P.D.Johnson and N.V.Smith, Phys. Rev. **B31**(6), p4046 (1985)

[35] P.M.Echenique and J.B.Pendry, J. Phys. C. **11**, p2065 (1978)

[36] E.G.McRae, Rev. Mod. Phys. **51**(3), p541 (1979)

[37] P.D.Johnson and N.V.Smith, Phys. Rev. **B27**(4), p2527 (1983)

[38] I.Tamm, Z. Phys. **76**, p848 (1932)

[39] J.G.Gay, J.R.Smith and F.J.Arlinghaus, Phys. Rev. Lett. **42**, p332 (1979)

[40] J.E.Inglesfield, Prog. Surface. Sci. **20**, p105 (1985)

[41] W.Shockley, Phys. Rev. **56**, p317 (1939)

[42] N.V.Smith, Phys. Rev. **B32**(6), p3549 (1985)

[43] C.T.Chen and N.V.Smith, Phys. Rev. **B35**(11), p5407 (1987)

[44] M.Stęślicka, R.Kucharczyk and J.Jurczyszyn, Surface. Sci. **231**, p52 (1990)

[45] P.D.Johnson and N.V.Smith, Phys. Rev. **B27**(4), p2527 (1983)

[46] D.Straub and F.J.Himpsel, Phys. Rev. **B33**(4), p2256 (1986)

[47] V.Dose, Physica Scripta **36**, p669 (1987)

[48] M.Donath and K.Ertl, Surface. Sci. Lett. **262**, pL49 (1992)

[49] L.E.Klebanoff, R.K.Jones, D.T.Pierce and R.J.Celotta, Phys. Rev. **B36**(15), p7849 (1987)

[50] W.Altmann, K.Desinger, M.Donath, V.Dose, A.Goldmann and H.Scheidt, Surface. Sci. **151**, pL185 (1985)

[51] A.Goldmann, V.Dose and G.Borstel, Phys. Rev. **B32**, p1971 (1985)

[52] A.Goldmann, M.Donath, W.Altmann and V.Dose, Phys. Rev. **B32**, p837 (1985)

[53] W.Jacob, V.Dose, U.Kolac and Th.Fauster, Z. Phys. B. **63**, p459 (1986)

[54] V.Dose, W.Altmann, A.Goldmann, U.Kolac and J.Rogozik, Phys. Rev. Lett. **52**, p1919 (1984)

[55] N.G.Stoffel and P.D.Johnson, Nucl. Inst and Meth. **A234**, p230 (1985)

[56] H.Scheidt, M.Glöbl and V.Dose, Surf. Sci. Lett. **123**, pL728 (1982)

[57] J.A.Simpson and C.E.Kuyatt, Rev. Sci. Inst. Vol**34**(3), p265 (1963)

[58] E.Harting and F.H.Read, *Electrostatic lenses* (Elselvier, Amsterdam. 1976)

[59] M.D.Crapper, A.L.D.Kilcoyne and D.P.Woodruff, Physica Scripta **41**, p546 (1990)

[60] S.L.Hulbert, P.D.Johnson, N.G.Stoffel, W.A.Royer and N.V.Smith, Phys. Rev. **B31**(10), p6815 (1985)

[61] T.T.Childs and I.Lindau, J. Vac. Sci. Technol. **A8**(3), p2521 (1990)

[62] V.Dagendorf, A.Breskin, R.Chechik and H.Schmidt-Böcking, Nucl. Inst. Meths. **A308**, p519 (1991)

[63] G.Corruthers, Appl. Optics. Vol**14**(7), p1667 (1975)

Chapter 4

k-Resolved Inverse Photoemission Study of Half-Monolayer Structures of O, C and N on Ni(100)

Contents

4 k-Resolved Inverse Photoemission Study of Half-Monolayer Structures of O, C and N on Ni(100) 95

4.1 Introduction 96

4.2 Experimental details 104

4.3 Clean Ni(100) : discussion of results 107

4.4 Ni(100)(2 × 2)-C : discussion of results 120

4.5 Ni(100)(2 × 2)-N : discussion of results 125

4.6 Ni(100)c(2 × 2)-O : discussion of results 130

4.7 Discussion and conclusions 137

4.1 Introduction

The study of adsorbates on the (100) surface of fcc transition metal surfaces has received a great deal of attention since the first quantitative determinations of adsorbate structures on well characterised surfaces were made in the early 70's (two of the first three structures to be studied being O and Na on Ni(100)) [1]-[5]. The interest in transition metal surfaces is not surprising considering their

widespread use in industrial catalysis; the surface carbide phase is the catalytically active phase of Ni in the methanation reaction [6]. Of the low Miller index crystal surfaces, the (100) surface has a particularly high symmetry and is generally viewed as a good starting point in understanding these catalytic materials.

In this chapter, the KRIPES technique is used to study the clean Ni(100) surface and the Ni(100)(2×2)-C ($p4g$), Ni(100)(2×2)-N ($p4g$), and Ni(100)$c(2\times2)$-O adsorption systems. An introduction to the three adsorption systems is presented in this section, starting with carbon and nitrogen on Ni(100) and then detailing the oxygen chemisorption system.

At coverages greater than 0.4 ML, carbon and nitrogen induce strong $(2\times2)-p4g$ 'clock' reconstructions on Ni(100) [8]-[13], in which the adsorbate atom sits in a fourfold hollow site with the surrounding nickel atoms rotated alternately clockwise and anticlockwise with respect to the clean surface positions; Fig(4.1) shows the geometry of the reconstruction [10]. A photoelectron diffraction (PhD) study on these two adsorbate systems concluded that the magnitude of the parallel displacement of the nickel atoms was $0.55\pm0.20\dot{A}$ accompanied by a top layer expansion of $0.15\pm0.10\dot{A}$, with the adsorbate atoms positioned $0.25\pm0.05\dot{A}$ above the nickel surface layer for an unreconstructed surface, and $0.10\pm0.12\dot{A}$ above the expanded top layer [12]. The PhD results for the carbon induced reconstruction agreed with LEED [7, 8] and surface extended X-ray absorption fine structure (SEXAFS) [14] measurements, although the PhD results for the nitrogen reconstructed surface were found to be at variance with SEXAFS studies [14, 15] (which found slightly larger nickel atom displacement and

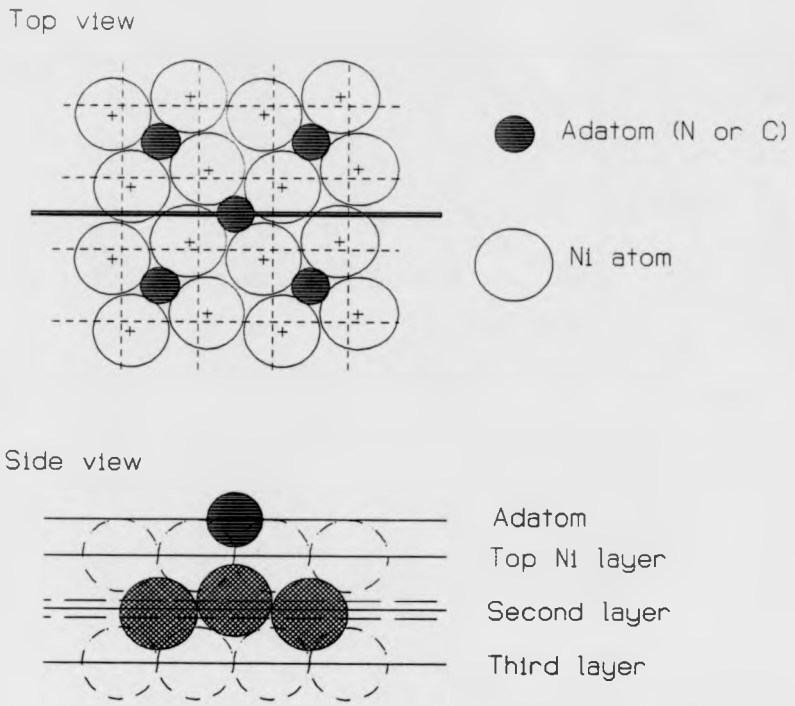

Fig(4.1) : Top view and side view (cut through solid line) of structure model for the N and C-induced *clock* reconstructions on Ni(100), corresponding to the (2×2) phase with $(p4g)$ symmetry. The adsorbate atoms occupy a four-fold hollow site with the nearest neighbour Ni atoms rotated, the underlying second layer Ni atoms being slightly buckled. The broken lines represent glide symmetry planes, their intersections being at the atomic positions of the unreconstructed Ni(100) substrate [7].

-no change in the first to second nickel layer spacing). The (2×2) structure has ($p4g$) symmetry, with strips of alternate squares and diamonds of surface layer nickel atoms; the LEED, SEXAFS and PhD results find the adsorbate to sit in the square hollow [8, 14, 16], although Szeftel *et al* [17] favour the diamond hollow (both structure assignments are consistant with the (2×2) unit cell and $p4g$ symmetry). From a physical perspective, the clock reconstruction occurs if the gain in chemisorption energy at small adsorbate height is greater than the increase in elastic energy accompanying the reconstruction and lattice distortion [11]; Reindl *et al* [11] proposed that the attraction between the adsorbate in the hollow site and second layer Ni atoms drives both C and N atoms toward the surface, and in order to decrease the repulsion energy between adatom and nearest neighbour Ni atoms, the latter adopt the reconstructed layer sites. The reconstruction however, means that pairs of surface Ni atoms come closer together, increasing the repulsion between them and the underlying second layer, which can be decreased by an outward relaxation of the surface layer and a inward contraction of the uncovered second layer. This corrugation effect of the second layer has been observed [7], highlighting the importance of the second Ni layer in the bonding process.

The results from angle resolved photoemission spectroscopy (ARUPS) [18, 10] on both C and N adsorbate induced reconstructions on Ni(100) have shown evidence of additional states in the region of the Ni d-band close to the Fermi level, and no evidence of upwardly dispersing states due to interaction involving the adsorbate p_z derived states [18]. No previous study has been made on the

unoccupied electronic structure for carbon or nitrogen on Ni(100).

The early stages of the oxidation of Ni(100) is perhaps the most studied adsorbate system [21], and although generally understood (for reviews see refs. [13, 19, 20]), there has in the past been a great deal of controversy (concerning both the geometrical and electronic structure), surrounding the chemisorption phases and the nucleation of the nickel oxide. Techniques used to study the structure of the oxygen chemisorbed phases on the Ni(100) surface include LEED [2]-[4][7]-[25]; surface extended and near-edge X-ray absorption fine structure (SEXAFS and NEXAFS) [15, 26, 27] ; electron energy loss spectroscopy (EELS) [28, 29]; photoelectron diffraction [30, 31]; medium energy ion scattering (MEIS) [32, 33] and scanning tunnelling microscopy (STM) [34].

Molecular adsorption of oxygen on Ni(100) is reported only for substrate temperatures below 100 K [20]; molecular oxygen dissociates at higher temperatures and atomic oxygen chemisorbs on the surface. At room temperature, oxygen chemisorption on Ni(100) leads to the formation of two structures: $p(2 \times 2)$ with $\theta_O = 1/4ML$ and $c(2 \times 2)$ with $\theta_O = 1/2ML$ [13, 29]. At coverages in the region $0.25 < \theta_O < 0.35ML$ the coexistance of both structures has been reported [35, 36], with the formation of nickel oxide islands also occurring prior to the complete formation of the $c(2 \times 2)$ structure at $\theta_O = 1/2ML$ [35, 37]. There has been some discussion concerning the actual adsorption site the oxygen adopts for the two structures, although it would appear that the oxygen adsorbs at a four fold symmetric hollow site for both the $p(2 \times 2)$ and $c(2 \times 2)$ surfaces [15],[20]-[23],[26, 27, 28], and not an asymmetric four fold hollow site at one pe-

riod proposed by Demuth *et al* [38] and later given some support by a DLEED investigation that determined the oxygen to be displaced by $0.4\dot{A}$ from the hollow site towards the twofold bridge position [39]. The geometries of the $p(2 \times 2)$ and $c(2\times2)$ structures are shown in Fig(4.2) [29]. The distance of the O adatom above the nickel surface has also been disputed, with early measurements indicating values of $d_O = 1.5\dot{A}$, $d_O = 0.9\dot{A}$ and coplaner with the nickel surface [28]. The later studies however point towards a d_O value of approximately $0.9\dot{A}$ above the first layer Ni atoms for both structures [15, 23, 26, 33, 40]. Some slight error in early determinations of this distance was due to neglecting the possibility of surface relaxation/contraction effects in the first two layers of the nickel substrate; Pendry *et al* have determined that on oxygen chemisorption, the clean Ni(100) surface (with first substrate layer slightly contracted $\approx -3.2\%$ [33]) relaxes such that the first substrate layer spacing expands by $0.1\dot{A}$ and the second layer buckles (amplitude $0.035 \pm 0.02\dot{A}$) but maintains a centre of gravity in the bulk position; this indicates a smaller O to Ni surface layer spacing of $d_O = 0.77\dot{A}$ [24].

Chemisorption on d-band metals is generally characterised by the formation of bonding and antibonding adsorbate-induced electronic states, lying below and above the d-band [41, 44]. Studies of the electronic structure of the O/Ni(100) system have been previously conducted using both X-ray photoemission (XPS) [42, 43] and ultra-violet photoemission spectroscopy (in angle integrated and angle resolved modes) [18, 43, 44] obtaining information regarding the occupied states, whilst studies using the inverse photoemission technique have provided knowledge of the unoccupied states [41, 45]-[48]. Although the specifics of the interaction

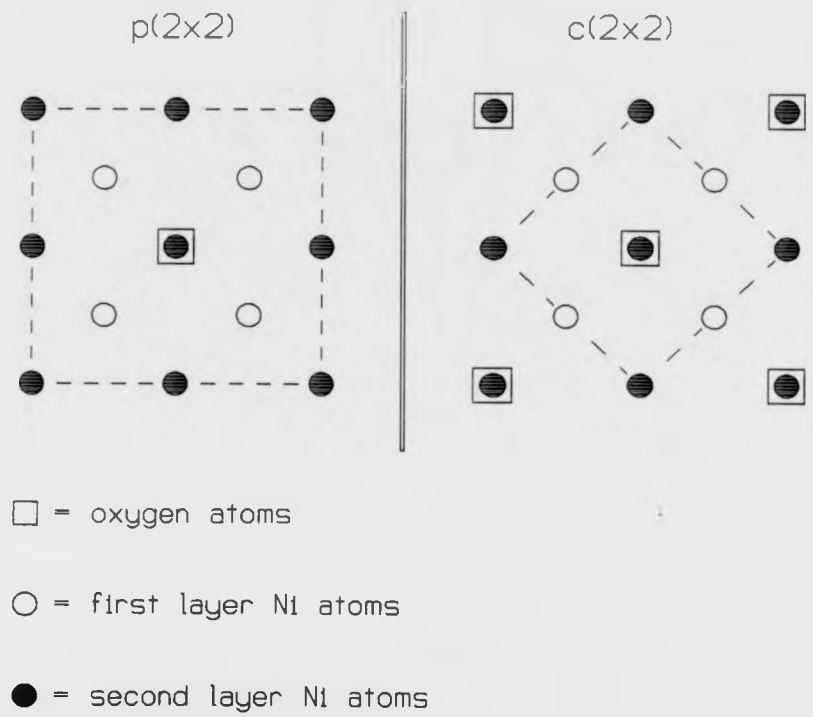

Fig(4.2) : Generally accepted structural models for the Ni(100)$p(2 \times 2)$-O and Ni(100)$c(2 \times 2)$-O adsorption phases. The dashed lines indicate the $p(2 \times 2)$ and $c(2 \times 2)$ primitive unit cells [29].

-between the oxygen overlayer and the nickel surface are not fully understood. there is evidence that the main interaction involves the O(2p) states with the Ni s-p band, with a charge transfer from Ni to O [19, 50]. Some interaction of the O(2p) with the Ni d-band has also been predicted theoretically, with the strength of the interaction increasing with oxygen coverage (at its stongest for NiO) [49]; the significance of the Ni(3d) involvement in the bonding process has however, yet to be fully established, although UPS investigations show only a slight attenuation to the Ni(3d) intensity on oxygen adsorption, which has been interpreted as indicating that any involvement with the Ni(3d) band is small [19]. The interaction between the adsorbed oxygen atoms results in an increased broadening of the oxygen induced bonding states [49] (at $\approx 6eV$ below the Fermi level [18, 51]), with an increase in dispersion of this band accompanying a change from the $p(2 \times 2)$ to $c(2 \times 2)$ structure [44, 49]. Some splitting of the O(2p) band into p_z, p_x and p_y components has been predicted and observed [43, 49, 51]; the O(2p)-induced bonding states occur at the same energy for both ordered overlayer structures, with an increase in intensity for the $c(2 \times 2)$ phase having been observed by angle-integrated UPS [19].

IPES studies on the O/Ni(110) [46] and O/Ni(111) [52] surfaces have observed oxygen induced antibonding states, which together with the information concerning the bonding states from photoemission [43, 53], provide a more complete picture of the adsorption on these two systems. Although IPES measurements on the Ni(100)$c(2 \times 2)$—O system have been previously reported [41, 45, 46, 47], the observation of the oxygen induced antibonding state that is predicted [46, 48, 52]

has not been seen. A possible reason for this concerns the isochromat energy at which these studies were conducted ($\hbar\omega = 9.7eV$), for which the oxygen induced state may be hidden by a direct transition between the bulk s-p bands. It has been previously suggested that by using different isochromat energies to study this system, causing the energetic position of the bulk contribution to be shifted, the oxygen induced antibonding state may be exposed [48].

In this chapter, the results of KRIPES measurements obtained at two different isochromat energies (10 eV and 11.5 eV) are presented for the clean Ni(100) surface and for the three half monolayer C, N and O- adsorption structures. No evidence for the existence of a previously predicted surface resonance on the clean surface, or an O-induced state close to the Fermi level for the $c(2 \times 2)$-O phase are observed in this investigation. However, clear adsorbate 2p-induced antibonding states are identified on all three surfaces, but with a clear distinction in behaviour between the $c(2 \times 2)$-O simple overlayer adsorption phase and the C and N-induced reconstructed phases being observed. The possible significance of these results is discussed, although it is stressed that proper interpretation can only be achieved with the aid of results from sophisticated calculations derived from theoretical modelling.

4.2 Experimental details

The experimental procedure is detailed in chapter 3, the KRIPES data being obtained at two isochromat energies ($\hbar\omega = 10$ and $11.5eV$). The Ni(100) sample was prepared by the usual combination of X-ray Laue alignment, spark eroding,

mechanical polishing, and in situ argon ion bombardment ($1keV$, $\approx 5\mu A\ cm^2$ for 10-15 mins.) and annealing to $\approx 950K$; with exposure to oxygen at high sample temperatures ($\approx 700K$)to reduce the level of carbon contamination. LEED and Auger electron spectroscopy (see Chapter 2) were used to verify the preparation of a well ordered clean surface (a sharp (1×1) LEED pattern being observed).

The KRIPES spectra were acquired at a pressure less than $5 \times 10^{-10} torr$, with the minimum time taken to obtain a spectrum following cleaning (including activating and focussing the pervatron electron gun) being approximately 50 mins. KRIPES spectra were acquired over a range of incidence angles from the clean Ni(100) surface before embarking on studies of the adsorption phases; the notation of incidence angle polarity with respect to sample surface normal is shown in Fig(4.3). Spectra were normalised to constant background intensity levels below the Fermi level and above the vacuum level.

The Ni(100)(2×2)-C ($p4g$) adsorption structure was obtained following exposure of the clean Ni(100) surface to ethylene (C_2H_4) at a pressure of $\approx 1\times10^{-7} torr$ for 10 minutes at a sample temperature approximately $650K$ [8]. Following cooling of the sample to room temperature, LEED showed a sharp $(2 \times 2)(p4g)$ pattern, with AES confirming this to be due to the presence of carbon on the surface. The Ni(100)(2×2)-C ($p4g$) adsorption phase was found to be very stable allowing greater spectra acquisition times.

The KRIPES manipulator lacks sample cooling facilities, so the Ni(100)(2×2)-N ($p4g$) adsorption structure could not be obtained using the process of exposing the nickel surface to ammonia at low temperatures [54].

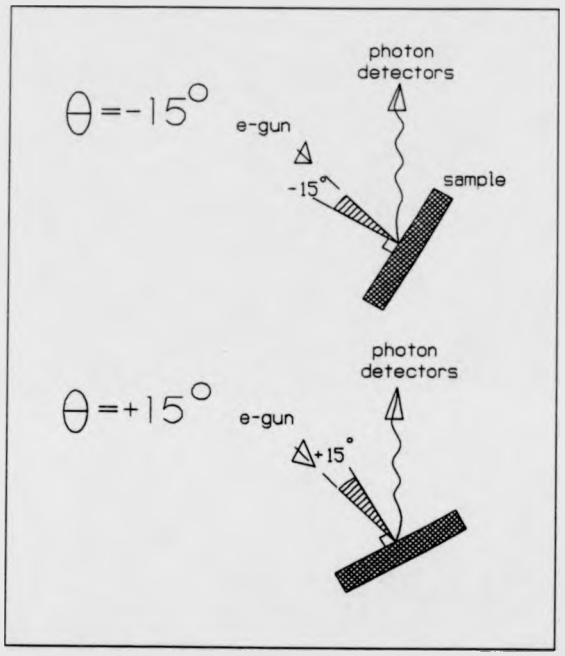

Fig(4.3) : schematic diagram defining electron incidence angle polarity for KRIPES. The electron gun is fixed at 45° to the optical axis of the detectors. Positive angles define movement of the surface normal away from the electron gun axis, towards the optical axis.

The technique of low energy bombardment with nitrogen, and subsequent annealing has been shown to be an effective method of producing this surface without requiring low temperatures [18], and was therefore used in this study. The process consisted of bombarding the clean surface with nitrogen ions at room temperature (using $500eV$ ions with a sample current of approximately $2\mu A$ for 10 mins), and annealing at $\approx 650K$ for 10 mins. LEED and AES were used to check the surface following this process, with LEED showing a sharp $(2\times 2)(p4g)$ pattern, and AES showing this to be due to nitrogen on the nickel surface; this adsorption phase was also found to be very stable.

The Ni(100)$c(2\times 2)$-O phase was obtained following exposure of the clean Ni(100) surface to approximately $25L$ molecular oxygen at a temperature of $350K$, and annealing to $450K$ for 5 to 10 mins. LEED showed a sharp $c(2\times 2)$ pattern, with AES showing only oxygen on the nickel surface. LEED was also conducted during exposure to oxygen, and the $p(2\times 2)$ pattern observed after approximately $2L$, with the $c(2\times 2)$ pattern visible after approximately $8L$ but sharpest at oxygen exposures between 20 to $30L$ (this being broadly compatible with previous studies of this surface [20, 21, 25, 27, 34, 35, 41, 46, 52])

4.3 Clean Ni(100) : discussion of results

KRIPES spectra were obtained from the clean Ni(100) surface over a range of angles set by the gun/detector geometry. The clean Ni(100) surface has been previously studied using normal incidence IPES [41, 55, 56, 45, 57, 58], k-resolved IPES [59]-[64] and spin-resolved IPES [47, 65], using isochromat energies close to

$10eV$ (mainly at $9.7eV$ using the iodine-filled Geiger-Müller tube)

KRIPES spectra from the present experiments at $10eV$ and $11.5eV$ are summarised in Fig(4.4). For both isochromat energies, the spectra from the clean Ni(100) are dominated by three main features, in agreement with previous IPES studies on this surface [47, 55, 56, 60, 61, 62, 63, 65]. Fig(4.5) shows normal incidence spectra for both $10eV$ and $11.5eV$ isochromats with the three features labelled. The peak observed close to the Fermi level (B1) is associated with a transition into the unoccupied Ni 3d-band, and shows little dispersion with increasing $k_{\|}$. A peak appearing 1-2 eV above the Fermi level in the normal incidence spectra (labelled B2) and which disperses strongly to higher energies with increasing incidence angles is associated with transitions to the Ni s-p band. The third feature (IS) observed at approximately 4-5 eV above the Fermi level at normal incidence is associated with transitions into the image potential surface states, and this also shows a dispersion to higher energies with increasing incidence angles. The KRIPES spectra obtained at $\hbar\omega = 11.5eV$ are quite similar to the $\hbar\omega = 10eV$ spectra, although they show better spectral resolution due to a characteristic of the LiF lens detection system employed. The transition to the Ni 3d-band is more intense at this isochromat energy, with the s-p band peaks displaced to a lower energy as a direct consequence of the different photon energy employed (this changes the perpendicular component of the electron momentum involved in this strongly bulk direct transition occuring between the dispersing s-p bands).

Fig(4.4) : k-resolved inverse photoemission spectra from the clean Ni(100) surface, obtained at two different isochromat photon energies : (a) $\hbar\omega = 10eV$, and (b) $\hbar\omega = 11.5eV$.

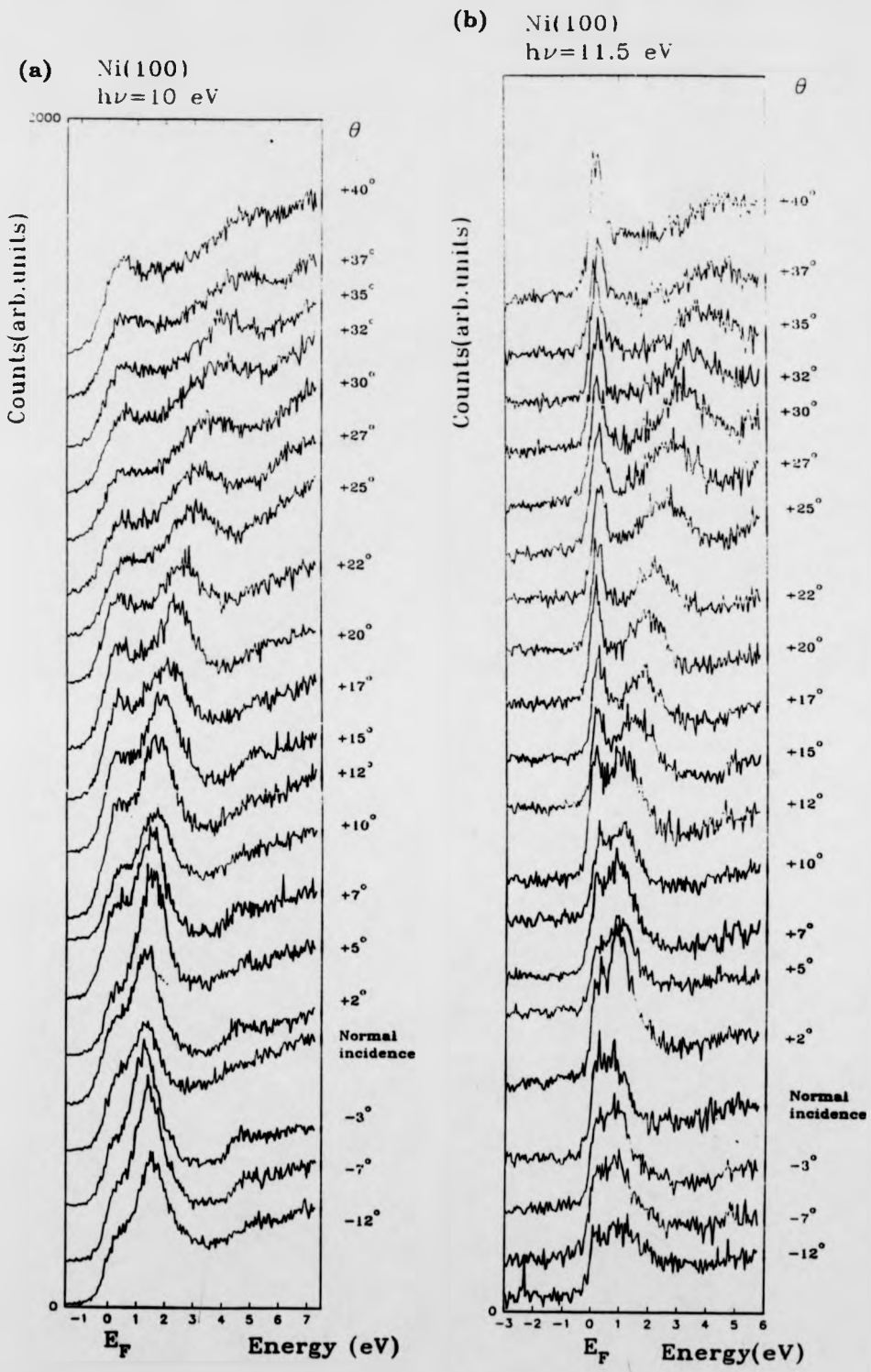
(a)
Ni(100)
hν=10 eV
θ
+40°
+37°
+35°
+32°
+30°
+27°
+25°
+22°
+20°
+17°
+15°
+12°
+10°
+7°
+5°
+2°
Normal incidence
-3°
-7°
-12°
Counts(arb.units)
E_F
Energy (eV)
(b)
Ni(100)
hν=11.5 eV
θ
+40°
+37°
+35°
+32°
+30°
+27°
+25°
+22°
+20°
+17°
+15°
+12°
+10°
+7°
+5°
+2°
Normal incidence
-3°
-7°
-12°
Counts(arb.units)
E_F
Energy(eV)

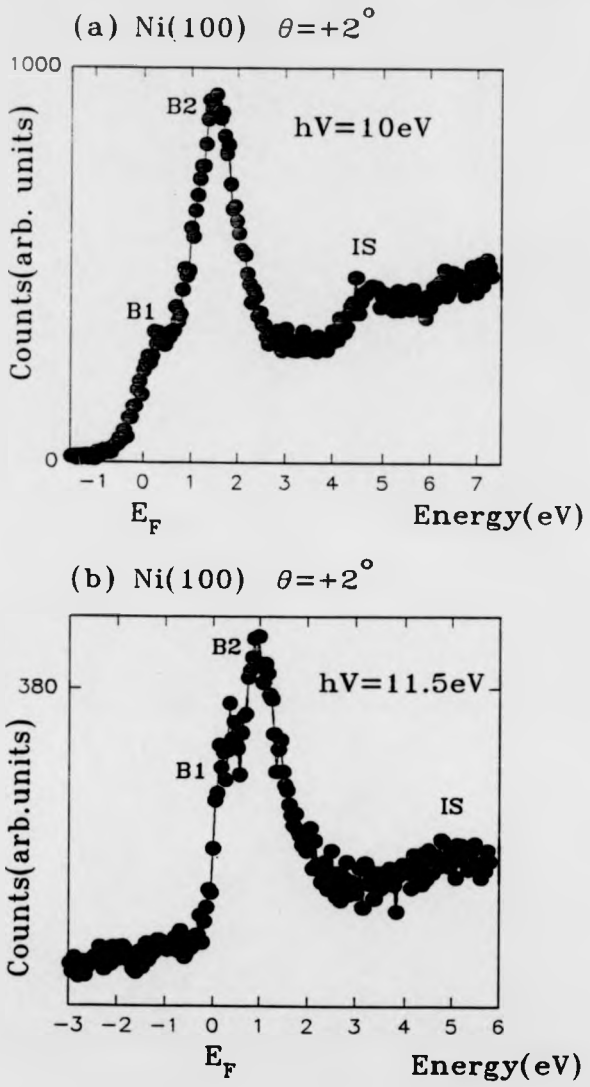

Fig(4.5) : KRIPES spectra obtained at $\theta = +2^{o}$ from the clean Ni(100) surface at (a) $\hbar\omega = 10eV$, and (b) $\hbar\omega = 11.5eV$. Three features are labelled, **B1** corresponding to a transition to the d-band; **B2** being due to a transition to the s-p band, and **IS** associated with a series of image states that converge on the vacuum level.

The change in amplitude of the d-band related peak between the two isochromat spectra can be better understood by comparing the possible direct transitions for the $10eV$ and $11.5eV$ isochromats, see Fig(4.6). The transition to the d-state for the $10eV$ photon energy must occur very close to the X point in the band structure, at which this transition is symmetry forbidden [55]. For the $11.5eV$ photon energy, this transition is moved closer to the Γ point, so the cross section associated with this transition is expected to rise.

For both the lower energy peaks (B1 and B2), the possibility that each may contain more than one feature has been previously suggested [47, 64, 66]. For the s-p band peak, the second state which has been proposed to contribute to this intensity is a Shockley surface state, or more specifically a surface resonance; this has been proposed on the basis of multiple reflection model calculations of image potential and intrinsic surface states (a similar resonance has been observed on the Cu(100) surface close to the s-p band peak using $11.0eV$ isochromat energy [67]). The possible existence of this surface resonance has been previously proposed to explain the preferential decrease in intensity of the s-p band peak (observed using $9.7eV$ photon energy isochromats at normal incidence) following small exposures of the nickel surface to molecular oxygen [47]. As the d-band related peak was observed not to attenuate as dramatically as the s-p band related peak, it was assumed that a surface feature was being attenuated by the surface contamination. For the spectral peak close to the Fermi level (which has been attributed to transitions into the Ni d-band), there has been a previous report that O adsorption can lead to an enhancement in the amplitude of this

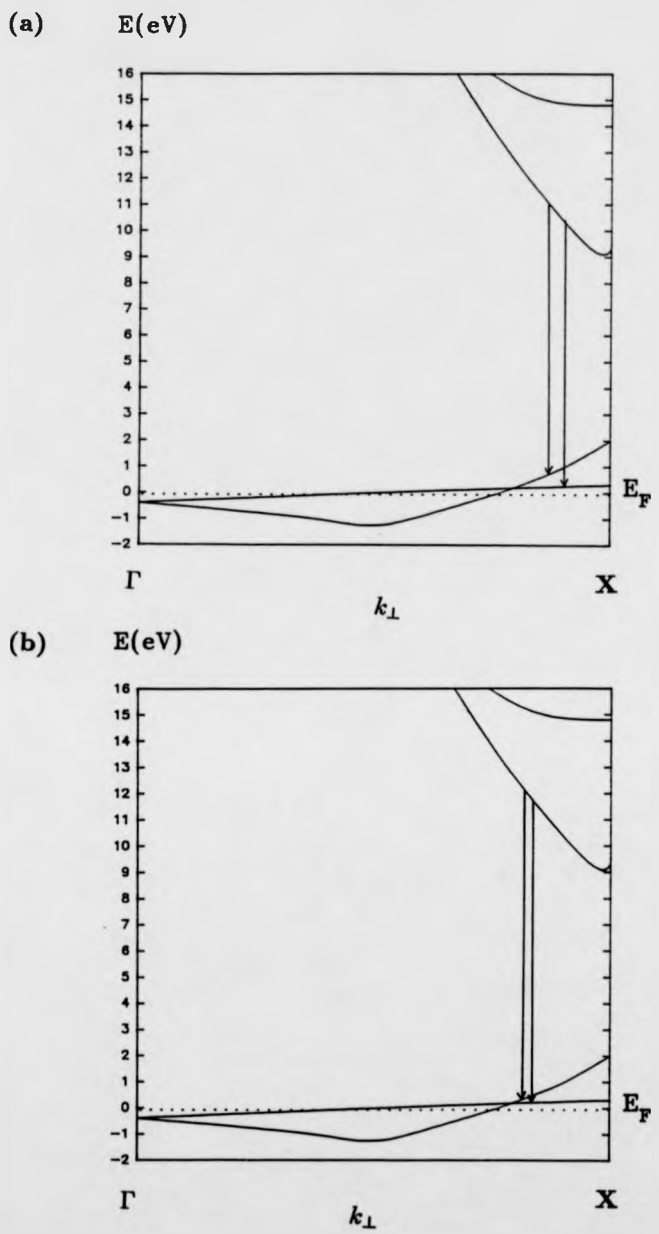

Fig(4.6) : The $k_\perp$ value of the radiative transitions **B1** and **B2** along the [100] Γ-X line near X. (a) shows allowed transitions for $\hbar\omega = 10eV$. (b) shows allowed transitions for $\hbar\omega = 11.5eV$.

-feature, implying that a new oxygen induced feature occurs close to the Fermi level [41, 45] (this is discussed in the Ni(100)$c(2 \times 2)$-O study of section(4.6)); other measurements have shown a slight attenuation of this peak with oxygen adsorption, but there is a general consensus of opinion that the B2 peak is more strongly attenuated than the B1 peak (this is the same evidence which has been used to support the idea of a surface resonance contribution to B2). The attenuation of the s-p band and image state peaks is shown clearly in Fig(4.7) for the $10eV$ isochromat energy ($\theta = +2^{o}$), following increasing exposures to O_2. In order to investigate whether the surface resonance does indeed exist, the adsorption test has been conducted for the same incidence angle at the higher photon energy ($11.5eV$), see Fig(4.8). At this higher photon energy, the energetic position of the s-p band related peak is shifted, but any surface related features should remain stationary (as previously mentioned). The surface resonance contribution should therefore be more readily visible in this series of spectra, appearing as a shoulder on the high energy side of the s-p band peak for the clean surface which would attenuate with increasing oxygen exposure. The spectra shown in Fig(4.8) show no evidence for the existence of this shoulder feature, and the s-p band related peak is still dramatically attenuated with little change in intensity of the d-band related peak.

The difference in intensity change between the two peaks can also be explained without the presence of secondary surface state features, by considering the role of surface Umklapp in the KRIPES spectra.

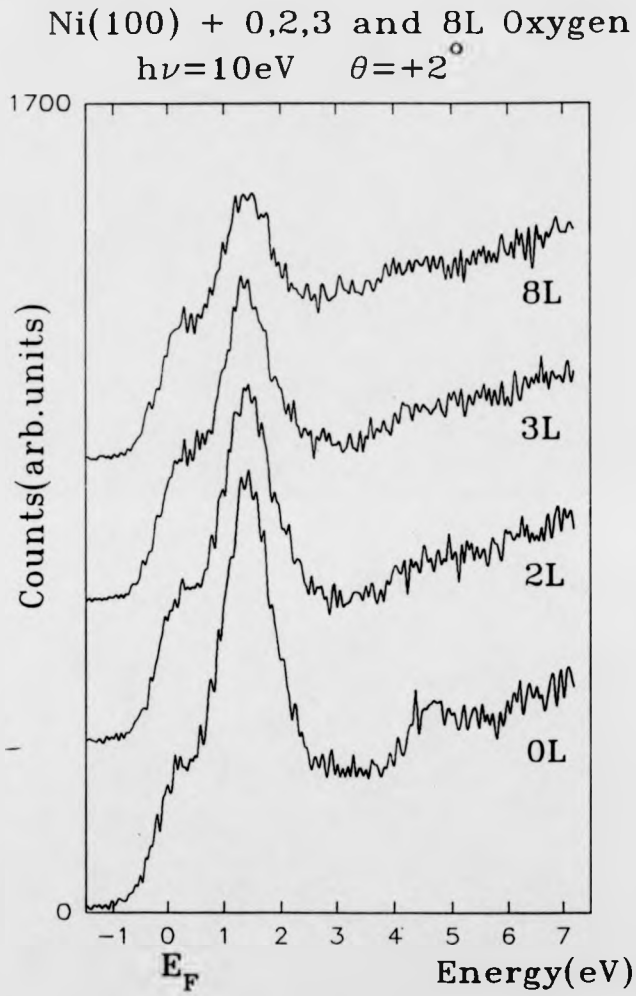

Fig(4.7) : KRIPES spectra showing the effect of increasing oxygen exposure to the clean Ni(100) surface, obtained at $\hbar\omega = 10eV$ and incidence angle $\theta = +2°$.

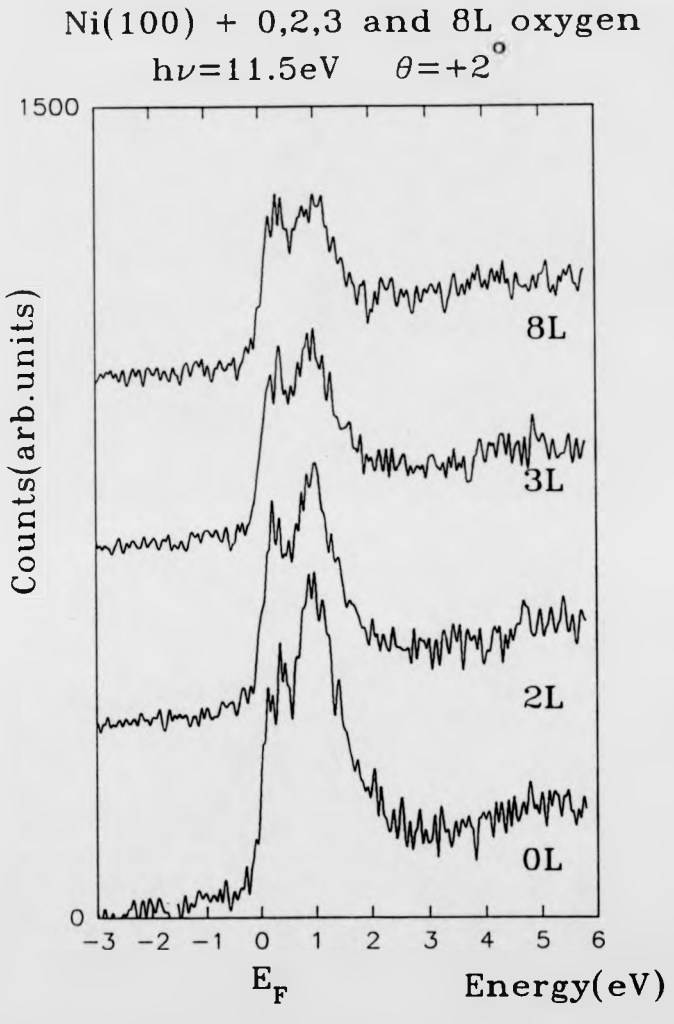

Fig(4.8) : KRIPES spectra showing the effect of increasing oxygen exposure to the clean Ni(100) surface, obtained at $\hbar\omega = 11.5eV$ and incidence angle $\theta = +2^o$.

The arguments for the existence of these states appear not to take adequate account of the problems that arise in the proper assignment of new spectral features following adsorption, due to the role of Umklapp. The problems associated with Umklapp are well recognised in ARUPS but also equally relevant to KRIPES. The different behaviour of the d-band and s-p band related peaks during oxygen adsorption (or general contamination of the surface) can be better understood by considering the effects of a disordered surface on the character of the two transitions. The loss of parallel momentum conservation that occurs with increased surface disorder, can also lead to changes in spectral intensity at different nominal values of parallel momentum. This is very relevant considering that the bulk band structure contributions come from two quite different types of state (the s-p bands which disperse strongly in both parallel and perpendicular components of the momentum, and the d-band which is localised in real space and disperses only weakly in momentum). Any loss of parallel momentum conservation or introduction of new reciprocal net vectors as a consequence of surface Umklapp, can then be expected to attenuate the s-p band transition intensities in the KRIPES spectra quite strongly, while the intensities associated with transitions to the flat d-band should experience little change. For the specific case of the $9.7eV$ isochromats on Ni(100), as has been already noted, the cross-section for inverse photoemission is weak because the k-conserving transition occurs close to the X-point at which the cross-section is zero on symmetry grounds. Any relaxation of k-conservation could therefore lead to an actual increase in the spectral intensity observed, although this is a delicate balance since the d-band passes be-

low the Fermi level at the Γ-point (the actual intensity therefore is determined by some integral over the cross section and occupation of the d-band at each value of perpendicular component of electron momentum). For the case of ordered overlayers such as the $c(2 \times 2)$-O phase, that have a real space periodicity larger than that of the substrate, new reciprocal net vectors are introduced which can effectively transfer spectral intensity (as a result of surface Umklapp) from other parts of the surface Brillouin zone not sampled on the clean surface. The $E_f(k_{\|})$ dispersion of the observed states were calculated and are shown in Fig(4.9). The energetic position of the final state relating to the sp-band transition can be see to be shifted for the two isochromat energies, with little variance for the image states and d-band transitions within the estimated error limits. The error in determining normal incidence is approximately $\pm 1^{o}$

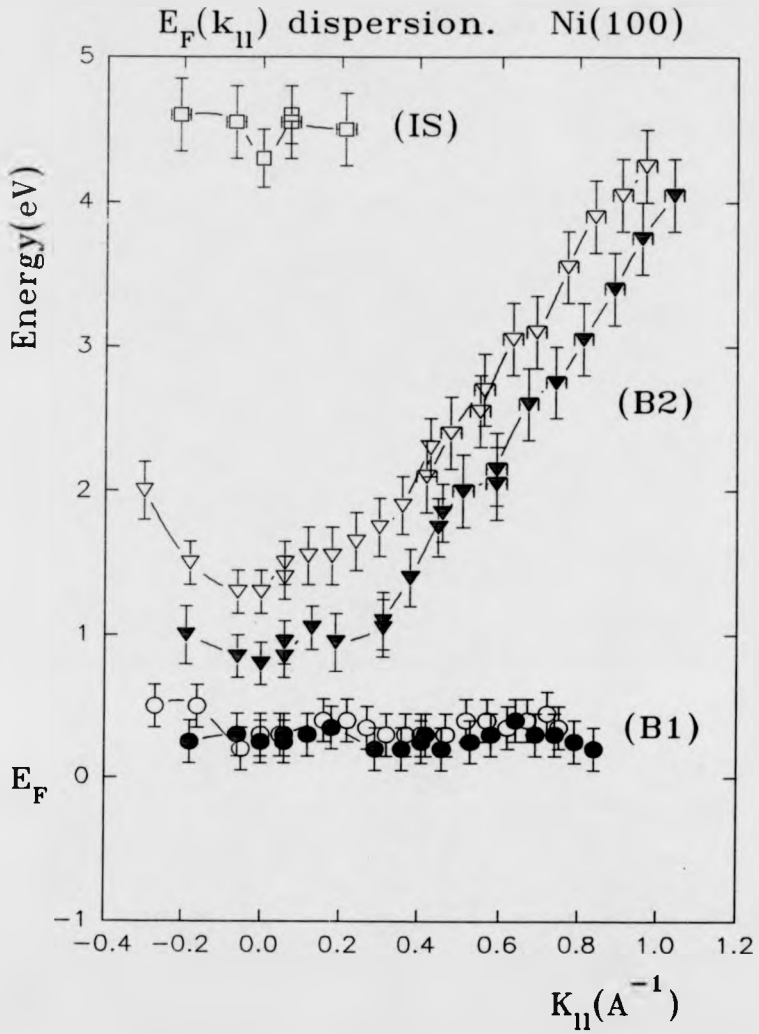

Fig(4.9) : $E_f(k_{\|})$ dispersion of the experimentally observed states from the clean Ni(100) surface (Fig(4.4a)). Open circles, triangles and squares were obtained at $\hbar\omega = 10eV$. Filled circles and triangles represent points taken from $\hbar\omega = 11.5eV$ isochromat spectra of Fig(4.4b).

4.4 Ni(100)(2×2)-C : discussion of results

Following formation of the Ni(100)(2×2)-C ($p4g$) surface, KRIPES measurements were obtained at $10eV$ and $11.5eV$ isochromat energies. The range of electron incidence angles used was similar to that of the KRIPES investigation of the clean surface.

Fig(4.10) shows the series of spectra obtained at the $10eV$ isochromat energy. At angles close to normal incidence the spectra resemble those of the clean Ni(100) surface, with an image state feature still observed at $\approx$ 4-5eV above the Fermi level. The peak relating to the transition to the s-p band (at $\approx 1.2eV$ above the Fermi level), is attenuated in comparison with the clean surface while the d-band related peak is slightly more intense. On increasing incidence angles away from normal incidence, the s-p band peak follows a similar dispersion in energy to that of the clean Ni(100) surface; this feature is only observable up to approximately $\theta = +27^o$ after which it contributes to a general flattening of the normal sloping background. At an incidence angle of $\theta = +20^o$, a new peak becomes visible at approximately $1.5eV$ above the Fermi level. This feature has a flat dispersion with increasing incidence angles, and is very clear at angles greater than $\theta = +27^o$ (at which there is little interference from transitions to the unoccupied s-p band).

The KRIPES spectra taken at the $11.5eV$ photon energy are shown in Fig(4.11), and are also similar to the clean Ni(100) spectra for electron incidence angles close to normal incidence. As in the $10eV$ isochromat spectra, an image state is observed at $\approx$ 4-5eV above the Fermi level (appearing at the same energy as for the $10eV$ isochromat spectra, as expected for a surface state), with the d-band

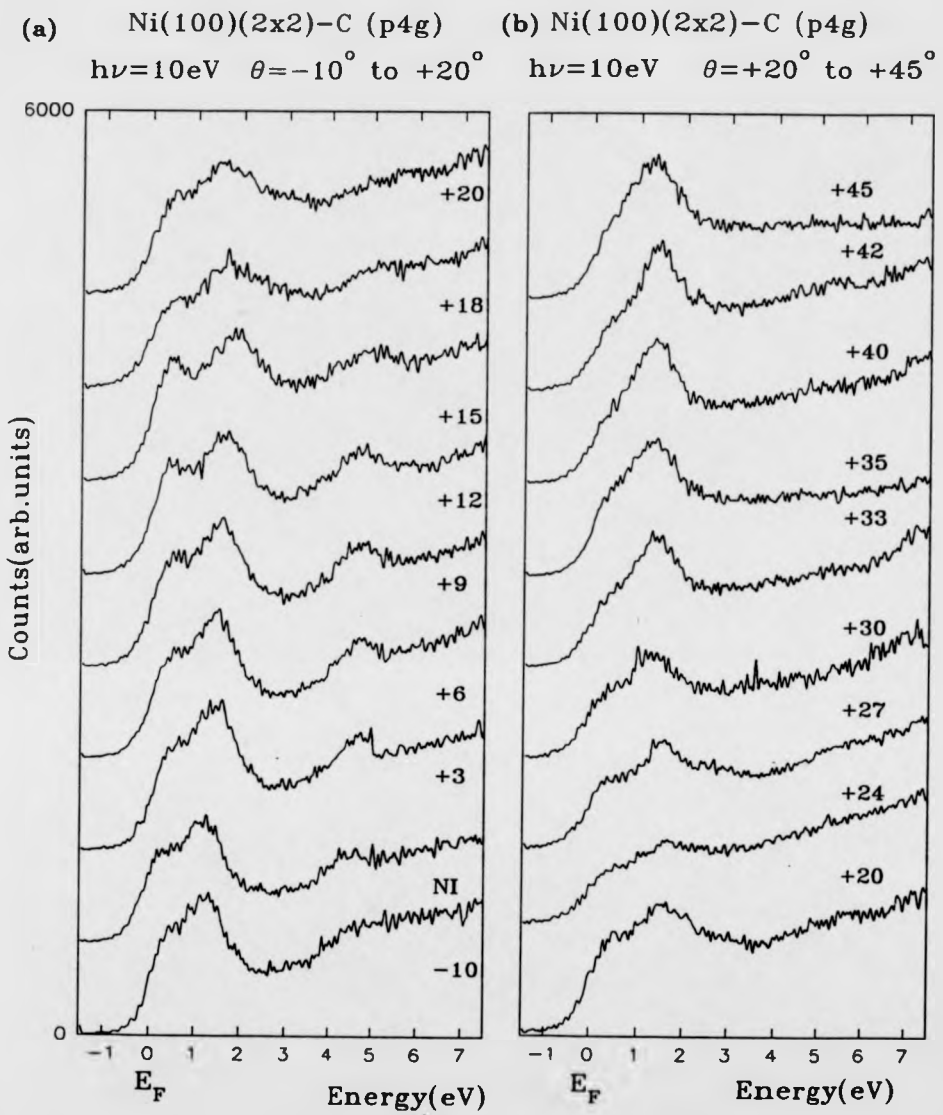

Fig(4.10) : KRIPES spectra from Ni(100)(2 × 2)-C($p4g$) at $\hbar\omega = 10eV$. (a) $\theta = -10°$ to $+20°$. (b) $\theta = +20°$ to $+45°$.

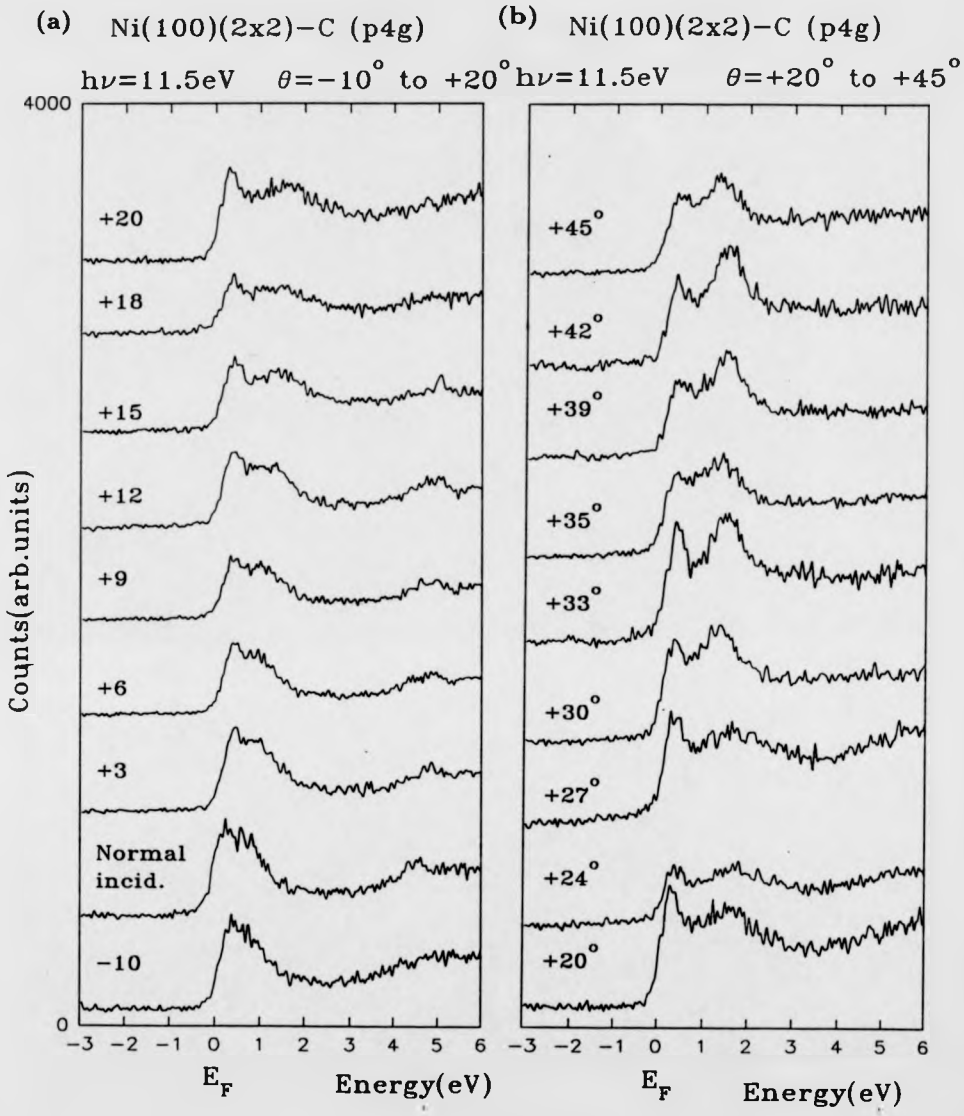

Fig(4.11) : KRIPES spectra from Ni(100)(2 × 2)-C($p4g$) at $\hbar\omega = 11.5eV$.

(a) $\theta = -10°$ to $+20°$. (b) $\theta = +20°$ to $+45°$.

-related peak (at $\approx 0.3eV$ above the Fermi level) having an intensity and dispersion similar to that observed for the clean Ni(100) surface. The peak associated with the transition to the unoccupied s-p band, disperses to higher energy with increasing incidence angles, and is visible upto $\theta = +27^{o}$, after which it contributes to a flattening of the higher energy background (as observed for the $10eV$ spectra). The carbon induced state observed in the $10eV$ isochromat spectra is also observed at the $11.5eV$ photon energy, appearing at $1.5eV$ above the Fermi level; this peak is also of a similar intensity to that seen in the lower energy isochromat and exhibits a flat dispersion in energy with increasing incidence angles.

The $E_f(k_{\|})$ dispersion plot for the Ni(100)(2×2)-C ($p4g$) surface is shown in Fig(4.12). The C-induced two-dimensional band (labelled SS) can be seen to be essentially flat, which suggests that they are a consequence of an interaction with the nickel d-band. This hypothesis is discussed with respect to the oxygen and nitrogen adsorption results in section(4.7).

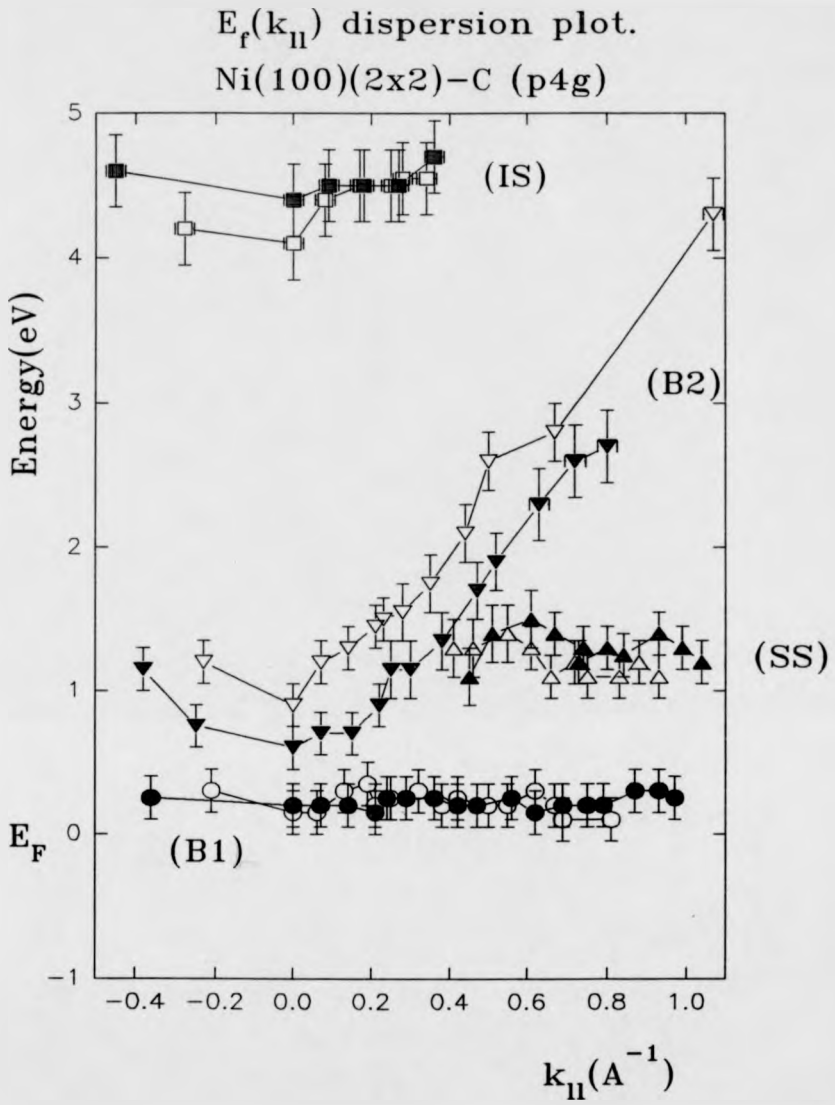

Fig(4.12) : $E_f(k_{\|})$ dispersion of the experimentally observed states from the Ni(100)(2×2)-C$(p4g)$ surface (see Figs(4.10-11)). Filled and empty symbols represent experimental points obtained at $\hbar\omega = 11.5eV$ and $\hbar\omega = 10eV$ photon energies respectively. The features **B1, B2** and **IS** are previously assigned features observable in clean spectra. Feature **SS** represents the C-induced state.

4.5 Ni(100)(2×2)-N : discussion of results

KRIPES spectra were obtained for the Ni(100)(2 × 2)-N surface at $10eV$ and $11.5eV$ isochromat energies, over electron incidence angles in the range $-15^o < \theta < +42^o$ with respect to the surface normal.

Fig(4.13) shows a series of KRIPES spectra obtained at $\hbar\omega = 10eV$, for incidence angles from $\theta = -15^o$ to $+27^o$; at angles greater than $+27^o$, only the features relating to the d-band and s-p band transitions are observed. In comparison with the KRIPES spectra from the clean Ni(100) surface, the d-band related peak and the s-p band peak follow a similar dispersion, with the intensity of the sp-band peak attenuated (the d-band peak remaining mainly unchanged). A N-induced feature is observed at approximately 2.5-4.5eV above the Fermi level in the range $-15^o < \theta < +15^o$, appearing more intense at negative incidence angles away from normal incidence (i.e crystal surface normal rotated away from detector optical axis).

This N-induced peak shows a flat energy dispersion with varying incidence angles and an increased intensity at the negative incidence angles. This increased intensity can be explained if the actual geometry of the sample to the detector is considered. Since the experiment is conducted in a mirror plane of the crystal the emission perpendicular to the surface is s-polarised and emission at grazing angles shows an enhanced contribution of p-polarised light. The increased intensity of the N-induced state at negative incidence angles where the emission is measured at angles closer to the surface parallel therefore inplies that emission from this state is p-polarised leading to the conclusion that the final state is -

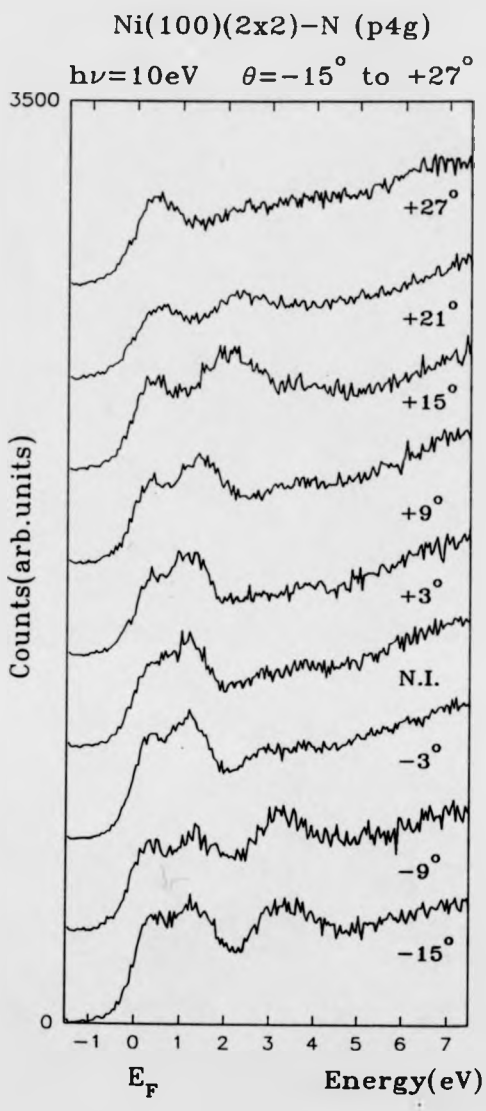

Fig(4.13) : KRIPES spectra from Ni(100)(2 × 2)-N($p4g$) at $\hbar\omega = 10eV$ for incidence angles $\theta = -15°$ to $+27°$.

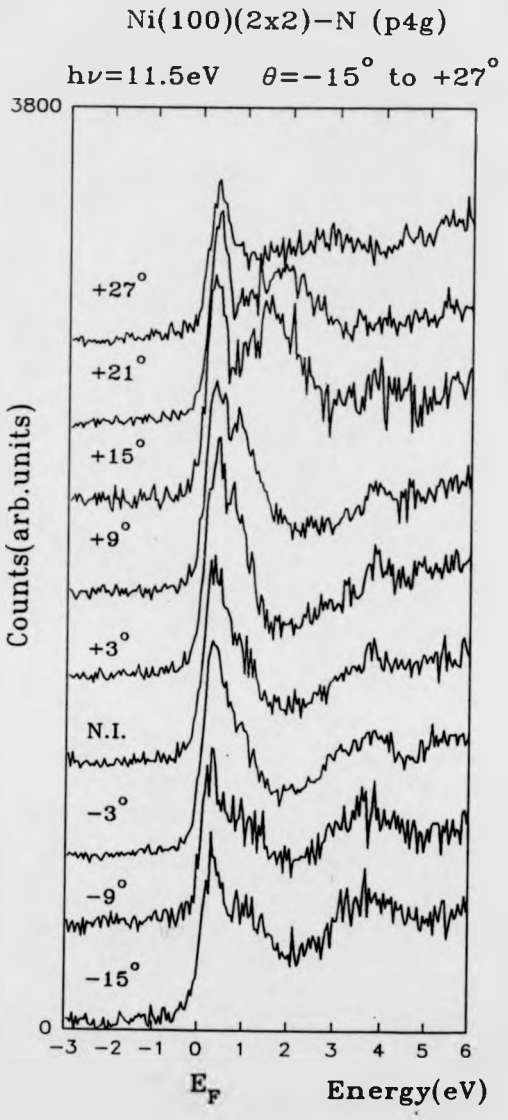

Fig(4.14) : KRIPES spectra from Ni(100)(2×2)-N($p4g$) at $\hbar\omega = 11.5eV$ for incidence angles $\theta = -15°$ to $+27°$.

-symmetric. This symmetry would be expected if the adsorbate state involved in the interaction has p_z character.

The spectra obtained at the higher photon energy ($11.5eV$) also show the N-induced feature at the same energy, and with the same angular dependence of intensity that was observed with the lower photon energy (see Fig(4.14)).

The $E_f(k_{||})$ dispersion is shown in Fig(4.15), with the N-induced band at approximately 3-4eV above the Fermi level displaying a flat dispersion in energy. This flat dispersion would suggest that (as for the C-induced band), it is a consequence of an interaction with the nickel d-bands. This possibility is discussed with reference to results from the C and O adsorption results in section(4.7).

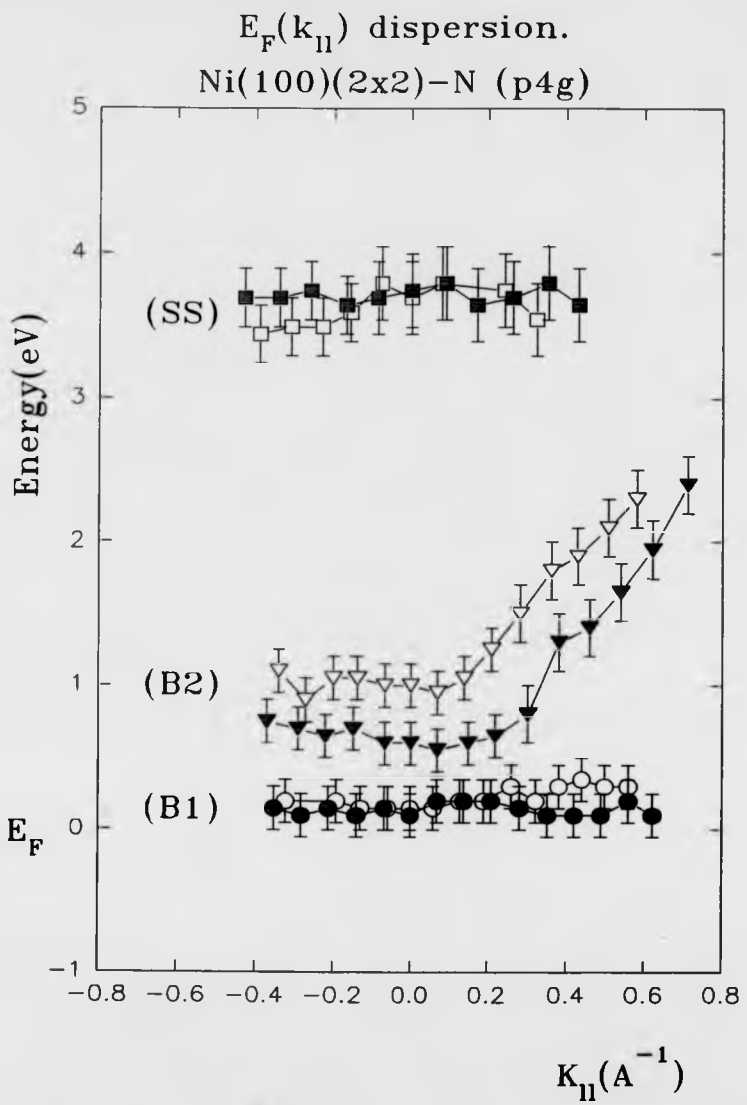

Fig(4.15) : $E_f(k_{\|})$ dispersion of the experimentally observed states from the Ni(100)(2×2)-N($p4g$) surface (see Figs(4.13-14)). Filled and empty symbols represent experimental points obtained at $\hbar\omega = 11.5eV$ and $\hbar\omega = 10eV$ photon energies respectively. The features **B1** and **B2** are previously assigned features observable in clean spectra. Feature **SS** represents the N-induced state.

4.6 Ni(100)$c(2 \times 2)$-O : discussion of results

KRIPES spectra obtained from the Ni(100)$c(2\times2)$-O surface at $10eV$ and $11.5eV$ photon energies are shown in Fig(4.16) and Fig(4.17) respectively.

For both isochromats, the image state feature observed from the clean Ni(100) surface is no longer visible. Some attenuation to the s-p band feature is also observed; the possible reasons for this have been discussed in section(4.3). The increased intensity of the feature just above the Fermi level (assigned to transitions to the unoccupied d-band) with O adsorption, has (as mentioned briefly in section(4.3)) been previously assigned to an O-induced state appearing close to the Fermi level [41, 45], although other studies have shown a decrease in amplitude of this feature [47] questioning the existence of this state. In the present study, a decrease in intensity of the d-band feature is observed in both isochromat spectra relative to those from the clean Ni(100) data, in agreement with Klebanoff *el al.* [47].

In the spectra of Fig(4.16-17), there would on first glance, appear to be little difference in comparison to the clean Ni(100) data (apart from the attenuation of s-p band peak intensity). Closer examination of the $10eV$ isochromat spectra in Fig(4.16), suggests that the peak assigned to the s-p band transitions on the clean surface occurs at a slightly higher energy in the $c(2 \times 2)$-O data. Fig(4.18) shows comparisons of spectra obtained at $\hbar\omega = 10eV$ for the clean Ni(100) and Ni(100)$c(2 \times 2)$-O surfaces at $\theta = +12^o$ and $\theta = +22^o$, normalised to constant background intensities.

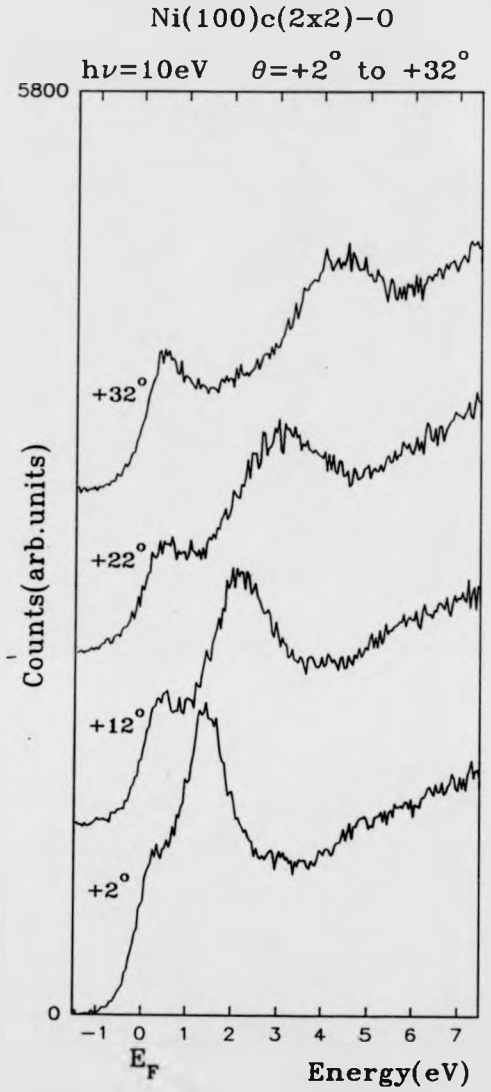

Fig(4.16) : KRIPES spectra from Ni(100)$c(2 \times 2)$-O at $\hbar\omega = 10eV$.

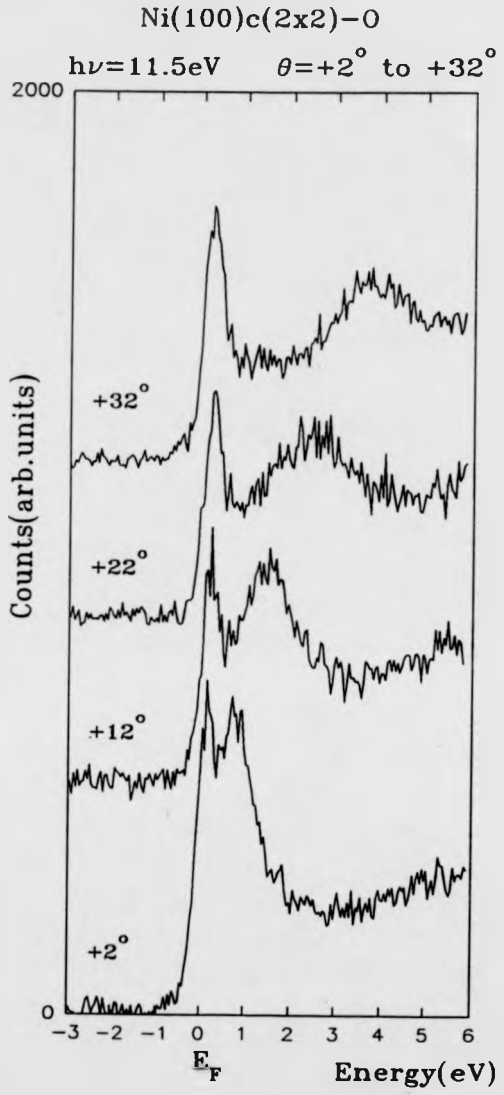

Fig(4.17) : KRIPES spectra from Ni(100)c(2 × 2)-O at $\hbar\omega = 11.5eV$.

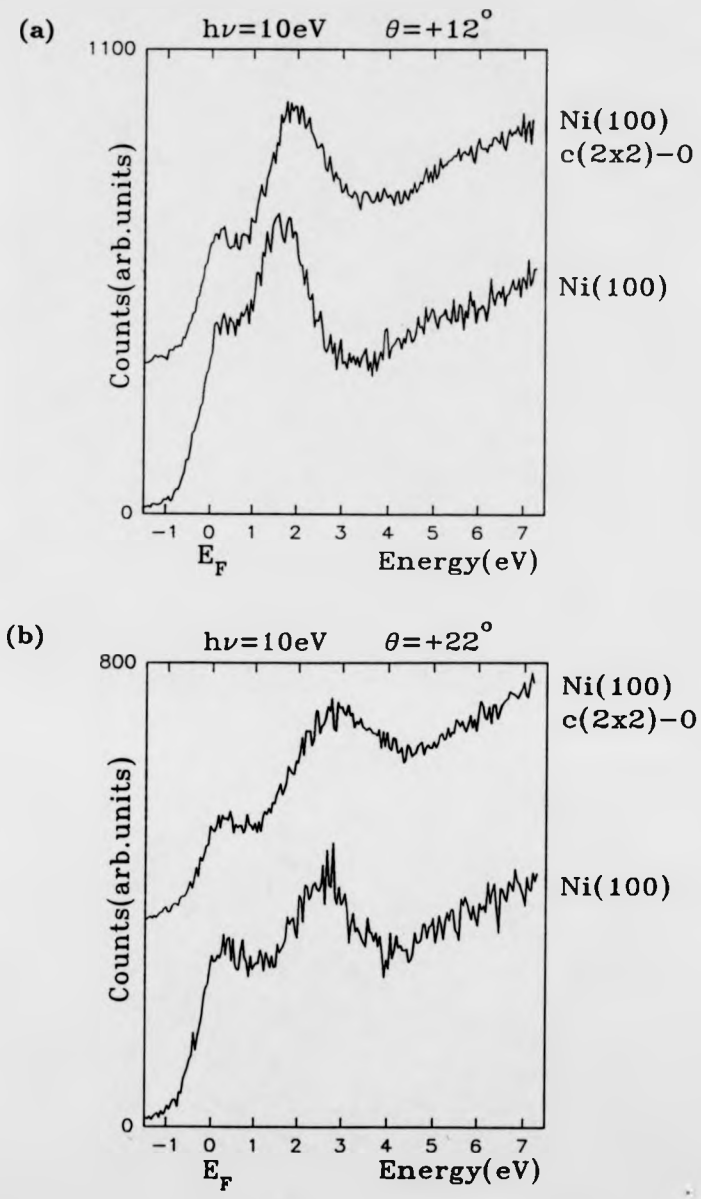

Fig(4.18) : Comparison of KRIPES spectra from clean Ni(100) and Ni(100)c(2×2)-O surfaces obtained at $\hbar\omega = 10eV$. (a) $\theta = +12^o$, (b) $\theta = +22^o$.

This energetic shift in intensity was also observed, but slighty more pronounced, for the $11.5eV$ isochromats shown in Fig(4.17); this improved clarity is an effect of better spectral resolution in the s-p band peak which occurs at slightly lower energy than inthe $10eV$ isochromat spectra (as a consequence of the s-p band dispersion in perpendicular component of electron momentum). A comparison of spectra obtained from the clean Ni(100) and Ni(100)$c(2\times2)$-O surfaces at $\hbar\omega = 11.5eV$ (at the same incidence angles used in Fig(4.18)) is shown in Fig(4.19). This energy shift is attributed to the presence of new O-induced states on the surface. The problem of surface Umklapp occurrence in connection with this observation has also been considered, but to our knowledge, on the basis of s-p band mapping of the clean Ni(100) surface, there should not be any new intensity at this final state energy as a consequence of surface Umklapp involving $c(2 \times 2)$ reciprocal net vectors.

Fig(4.20) summarises the two-dimensional band structure of the O-induced feature observed in the KRIPES data. These features show no detectable dispersion in perpendicular momentum (which is not conserved for a surface-localised state); the small difference in the apparent energy of this state obtained from the two isochromat energies is well within the precision limits of the energy determination. By comparison, the location of the s-p band mapped by the two different photon energies is shifted energetically due to different parts of the s-p band being mapped at the same values of parallel momentum.

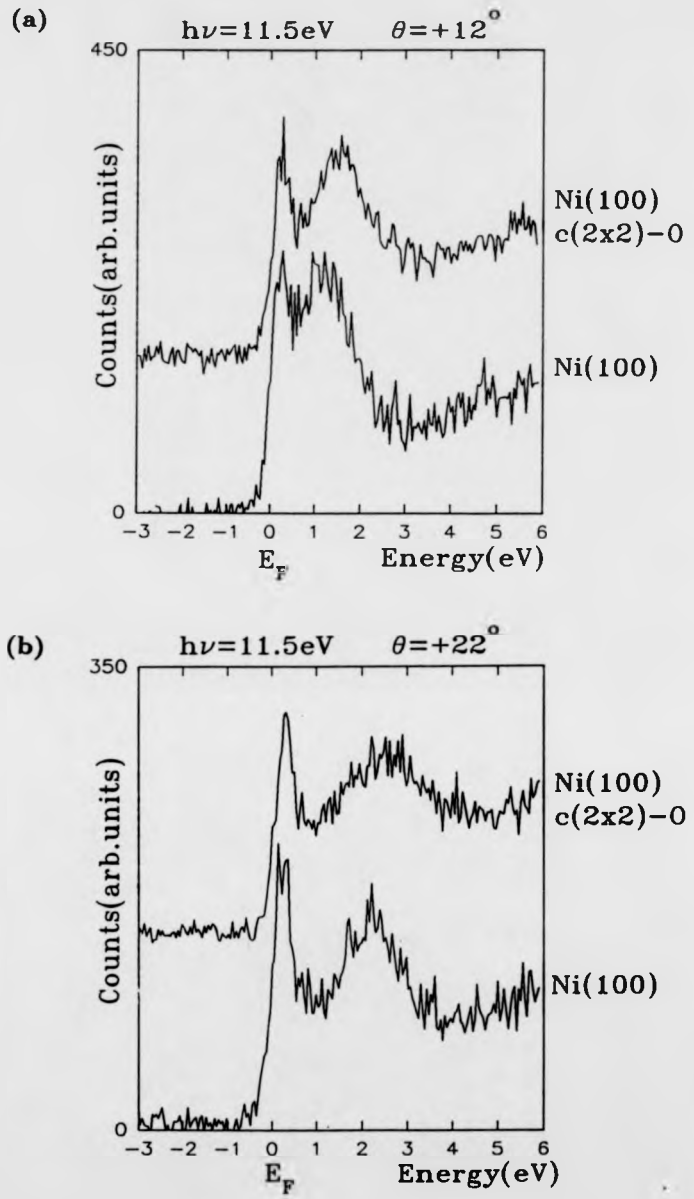

Fig(4.19) : Comparison of KRIPES spectra from clean Ni(100) and Ni(100)$c(2\times$ 2)-O surfaces obtained at $\hbar\omega = 11.5eV$. (a) $\theta = +12°$, (b) $\theta = +22°$.

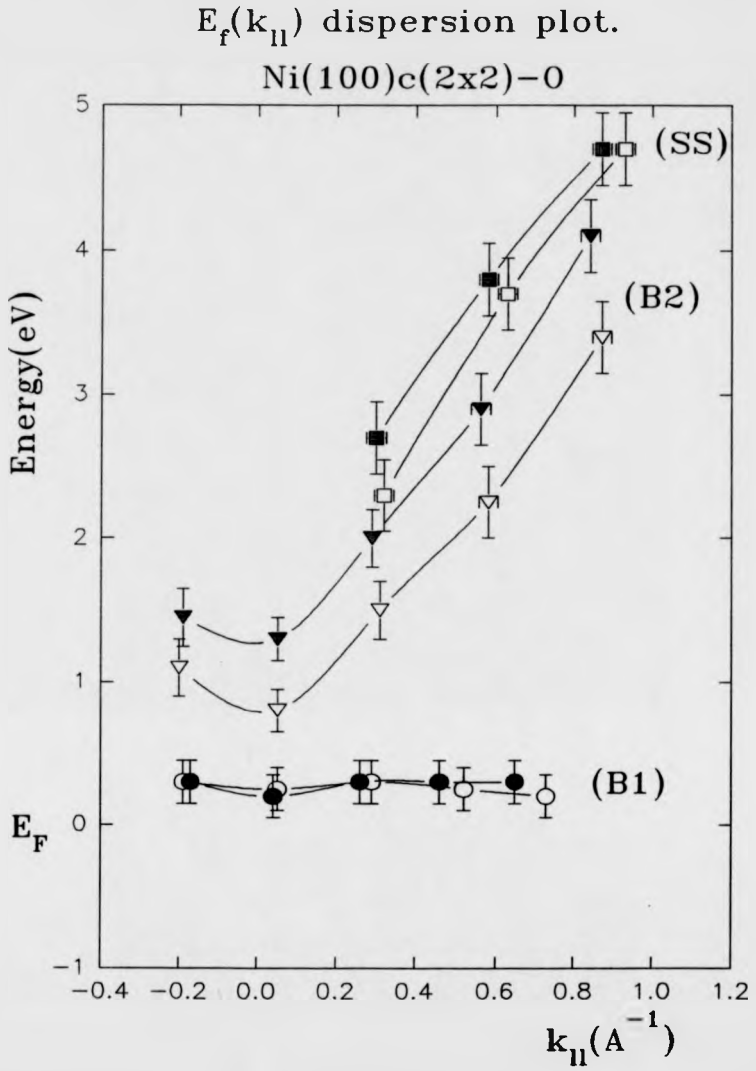

Fig(4.20) : $E_f(k_{||})$ dispersion of the experimentally observed states from the Ni(100)$c(2\times2)$-O surface (see Figs(4.16-17)). Filled and empty symbols represent experimental points obtained at $\hbar\omega = 11.5eV$ and $\hbar\omega = 10eV$ photon energies respectively. The features **B1** and **B2** are previously assigned features observable in clean spectra. Feature **SS** represents the O-induced state.

4.7 Discussion and conclusions

The results of KRIPES experiments reported here on the clean Ni(100) and $c(2 \times 2)$-O adsorption phase provide new information on the electronic structures of these surfaces.

Firstly, the intensity enhancement of the feature near the Fermi level (B1) that has previously been observed [41, 45] with O adsorption does not, on the basis of our arguments (concerning surface Umklapp effects, and momentum conservation for a disordered surface) provide convincing evidence for a new O-induced state, although these same arguments do not exclude the possibility that such a state might exist. In the present study, no experimental evidence for the existence of this O-induced state was observed, as the intensity near the Fermi level was found to decrease on forming the $c(2 \times 2)$-O phase (in agreement with another study on this system [47]). We have also argued that the observed attenuation of the s-p band feature (B2) on O adsorption does not necessarily imply that a surface resonance exists on the clean surface at this energy. From the data obtained here at the higher photon energy ($\hbar\omega = 11.5eV$), no evidence for the existence of this surface resonance was observed, indicating that this state is either not present, or has a low KRIPES cross-section. Thirdly, the enhancement on the high energy side of the peak (B2) attributed to the bulk s-p band transition, seen here after forming the $c(2 \times 2)$-O overlayer, is difficult to understand other than in terms of a true O-induced state.

KRIPES data from the N and C adsorption structures also show evidence for adsorbate induced states, which is now discussed with respect to the O-adsorption

data. The results from the three adsorption phases can be briefly summarised. Firstly, adsorbate 2p-induced states a few eV above the Fermi level have been identified, produced by the adsorption of C and N on Ni(100). Secondly, similar O 2p-induced states a few eV above the Fermi level have also been identified at a similar energy to those seen on other low index Ni surfaces. Thirdly, a clear distinction in behaviour of these adsorbate induced states is observed between the C and N phases, and the O adsorption phase. Perhaps the most important observation concerns the dispersion in energy of these features with $k_{||}$. Both C and N-induced states show an essentially flat dispersion while the O-induced state disperses quite strongly with parallel momentum. Considering the difference in the surface structure between the simple O overlayer in comparison with the N and C induced reconstructions, it is difficult to believe that there is not some connection between the structural effects and the electronic interaction. These results do not however, allow us to make any clear assignment as to the nature of the adsorbate induced states, and their relationship to the nature of the reconstruction, and to why O behaves so differently to C and N. To arrive at any clear conclusion, it would be necessary to 'unpick' the structure of a sophisticated total energy calculation which correctly predicts the observed structural and electronic properties. Some speculation concerning these different adsorption systems is however possible.

Perhaps the most obvious and simplest interpretation of the results can be obtained from the dispersion of these adsorbate induced states. For N and C , a flat dispersion of the adsorbate-induced states could be attributed to an interaction

of the 2p states with the localised Ni d-band states. For the O-induced states. the dispersion in energy with change in $k_{||}$ could be attributed with an interaction with the Ni s-p band. This description does offer an explanation for the very different dispersive properties, and is broadly in agreement with earlier ARUPS investigations which showed modifications to the occupied d-states for the N and C structures, but not for the $c(2\times 2)$-O phase. It is also clear that any changes to the electronic structure close to the Fermi level are likely to have implications for the total energy of a structure and would therefore offer a possible 'fingerprint' for the reconstruction.

A further important distinction between C and N adsorption sites and O adsorption sites concerns the adsorbate to top Ni layer distance. The C and N atoms occupy sites that are almost coplanar with the top Ni atoms as a consequence of the reconstruction [12], whereas the O atoms occupy sites 0.8Å above this layer [24]. A simple approach towards understanding the adsorbate-induced band structure for ordered chemisorbed overlayers is to seperate the adsorbate and substrate band structures. This approach considers firstly the two-dimensional band structure produced by adsorbate-adsorbate interaction and then includes the influence of the adsorbate-substrate bonding on that band structure. This formed the basis of early discussion of the Ni(100)c(2 × 2)-O system [49] and more recent discussion of experimental results for all three adsorption systems [10, 18]. The effect of the substrate on adsorbate-adsorbate interactions is likely to be strong even for O, as would be expected when the nearest neighbour Ni-O distances are significantly shorter than the O-O distances (1.9Å[23] compared

with 3.5Å). For the O overlayer however, it is still possible to consider direct adsorbate-adsorbate interactions, but the N and C adsorbate atoms that are coplanar with the top Ni layer can only effectively interact through metal atoms, an interaction which is closely linked to the N-Ni and C-Ni bonding specifically. Additionally the N-Ni and C-Ni nearest neighbour distances are smaller than the O-Ni nearest neighbour distance (≈ 1.80Å [12]) which would give further support to the C and N adsorbate interaction with Ni involving a hybridisation with the relatively localised Ni 3d-band.

References

[1] S.Andersson and J.B.Pendry, J. Phys. C: Sol. St. Phys. **5**, pL41 (1972)

[2] J.E.Demuth, D.W.Jepson and P.M.Marcus, Phys. Rev. Lett. **31**, p540 (1973)

[3] S.Andersson, B.Kasemo, J.B.Pendry and M.A.Van Hove, Phys. Rev. Lett. **31**, p595 (1973)

[4] S.Andersson and J.B.Pendry, Sol. St. Comm. **16**, p563 (1975)

[5] J.E.Demuth, D.W.Jepson and P.M.Marcus, J. Phys. C **8**, pL25 (1975)

[6] R.D.Kelly and D.W.Goodman, in *The Chemical Physics of Solid Surfaces and Heterogenous Catalysis, Vol.4* eds. D.A.King and D.P.Woodruff. (Elselvier, Amsterdam. 1982)

[7] Y.Gauthier, R.Baudoing-Savois, K.Heinz and H.Landskron, Surf. Sci. **251/252**, p493 (1991)

[8] J.H.Onuferko, D.P.Woodruff and B.W.Holland, Surf. Sci. **87**, p357 (1979)

[9] M.Grunze, P.A.Dowben and C.R.Brundle, Surf. Sci. **128**, p311 (1983)

[10] C.F.McConville, D.P.Woodruff, S.D.Kevan, M.Weinert and J.W.Davenport, Phys. Rev. **B34**(4), p2199 (1986)

[11] S.Reindl, A.A.Aligia and K.H.Bennemann, Surf. Sci. **206**, p20 (1988)

[12] A.L.D.Kilcoyne, D.P.Woodruff, A.W.Robinson, Th.Lindner, J.S.Somers and A.M.Bradshaw, Surf. Sci. **253**, p107 (1991)

[13] D.P.Woodruff in *The Chemical Physics of Solid Surfaces and Heterogenous Catalysis Volume 7*, eds D.A.King and D.P.Woodruff. (Elselvier, Amsterdam. 1993)

[14] M.Bader, C.Ocal, B.Hillert, J.Haase and A.M.Bradshaw, Phys. Rev. **B35**, p5900 (1987)

[15] L.Wenzel, D.Arvanitis, W.Daum, H.H.Rotermund, J.Stöhr, K.Baberschke and H.Ibach, Phys. Rev. **B36**(14), p7689 (1987)

[16] K.H.Rieder and H.Wilsch, Surf. Sci. **131**, p245 (1983)

[17] J.Szeftel, F.Mila and A.Khater, Surf. Sci. **216**, p125 (1989)

[18] A.L.D.Kilcoyne, D.P.Woodruff, J.E.Rowe and R.H.Gaylord, Phys. Rev. **B39**(17), p12604 (1989)

[19] C.R.Brundle and J.Q.Broughton in *The Chemical Physics of Solid Surfaces and Heterogenous catalysis Volume 3A*, eds. D.A.King and D.P.Woodruff. (Elselvier, Amsterdam. 1990)

[20] R.Berndt, J.P.Toennies and Ch. Woll, Surf. Sci. **244**, p305 (1991)

[21] W.Oed, H.Lindner, U.Starke, K.Heinz, K.Müller and J.B.Pendry, Surf. Sci. **224** p179 (1989)

[22] K.G.Lloyd and J.C.Hemminger, Surf. Sci. **143**, p509 (1984)

[23] W.Oed, H.Lindner, U.Starke, K.Heinz, K.Müller, D.K.Saldin, P.deAndres and J.B.Pendry, Surf. Sci. **225**, p242 (1990)

[24] K.Heinz, W.Oed and J.B.Pendry, Phys. rev. **B41**(14), p10179 (1990)

[25] T.D.Pope, S.J.Bushby, K.Griffiths and P.R.Norton, Surf. Sci. **258**, p101 (1991)

[26] J.Stöhr, R.Jäger and T.Kendelewitz, Phys. Rev. Lett. **49**, p142 (1982)

[27] D.Norman, J.Stöhr, R.Jäger, P.J.Durham and J.B.Pendry, Phys. Rev. Lett. **51**, p2052 (1983)

[28] T.S.Rahman, D.L.Mills, J.E.Black, J.M.Szeftel, S.Lehwald and H.Ibach, Phys. Rev. **B30**(2), p589 (1984)

[29] J.Colin de Verdiere, J.Szeftel and P.Soukiassian, Phys. Rev. **B42**(11), p7234 (1990)

[30] D.H.Rosenblatt, J.G.Tobin, M.G.Mason, R.F.Davis, S.D.Kevan, D.A.Shirley, C.H.Li and S.Y.Tong, Phys. Rev. **B23**, p3828 (1981)

[31] S.Y.Tong, W.M.Kang, D.H.Rosenblatt, J.G.Tobin and D.A.Shirley, Phys. Rev. **B27**, p4632 (1983)

[32] J.W.M.Frenken, J.F.Van de Veen and G.Allen, Phys. Rev. Lett. **51**, p1876 (1983)

[33] J.W.M.Frenken, R.G.Smeenk and J.F.Van de Veen, Surf. Sci. **135**, p147 (1983)

[34] E.Kopatzki and R.J.Behm, Surf. Sci. **245**, p255 (1991)

[35] P.H.Holloway and J.B.Hudson, Surf. Sci. **43**, p123 (1974)

[36] D.Taylor and R.Park, Surf. Sci. **125**, pL73 (1983)

[37] C.R.Brundle and H.Hopster, J. Vac. Sci. Technol. **18**, p663 (1981)

[38] J.E.Demuth, N.J.DiNardo and G.S.Cargil III, Phys. Rev. Lett. **50**, p1373 (1983)

[39] U.Starke, P.L.deAndres, D.K.Saldin, K.Heinz and J.B.Pendry, Phys. Rev. Lett. **46**, p12277 (1988)

[40] F.Jenson, I.Stensgaard, F.Besenbacher and C.Klink, Vacuum **41**, p337 (1990)

[41] H.Scheidt, M.Glöbl and V.Dose, Surf. Sci. Lett. **123**, pL728 (1982)

[42] P.R.Norton, R.L.Tapping and J.W.Goodale, Surf. Sci. **65**, p13 (1977)

[43] C.Benndorf, C.Nöbl and F.Thieme, Surf. Sci. **126**, p265 (1983)

[44] D.Jepson, C.Noguera, D.Spanjaard, C.Guillot, Y.Ballu and P.Thiry, Sol. St. Comm. **28**, p741 (1978)

[45] V.Dose, M.Glöbl and H.Scheidt, J. Vac. Sci. Technol. **A1**(2), p1115 (1983)

[46] K.Desinger, V.Dose, A.Goldmann, W.Jacob and H.Scheidt, Surf. Sci. **154**, p695 (1985)

[47] L.E.Klebanoff, R.K.Jones, D.T.Pierce and R.J.Celotta, Phys. Rev. **B36**(15), p7849 (1987)

[48] N.V.Smith and D.P.Woodruff, Progress in Surf. Sci. **21**(4) p295 (1986)

[49] A.Liebsch, Phys. Rev. **B17**(4), p1653 (1978)

[50] C.W.Bauschlicher and P.S.Bagus, Phys. Rev. Lett. **52**, p200 (1984)

[51] S.P.Weeks and E.W.Plummer, Sol. St. Comm. **21**, p695 (1977)

[52] W.Altmann, K.Desinger, M.Donath, V.Dose, A.Goldmann and H.Scheidt, Surf. Sci. **151**, p185 (1985)

[53] H.Conrad, G.Ertl, J.Küppers and E.E.Latta, Sol. St. Comm. **17**, p497 (1975)

[54] W.Daum, S.Lehwald and H.Ibach, Surf. Sci. **178**, p528 (1986)

[55] D.P.Woodruff and N.V.Smith, Phys. Rev. Lett. **48**(4), p283 (1982)

[56] G.Denninger, V.Dose, M.Glöbl and H.Scheidt, Sol. St. Commun. **42**(8), p583 (1982)

[57] V.Dose, M.Glöbl and H.Scheidt, Phys. Rev. **B30**(2), p1045 (1984)

[58] W.Reimer, Th.Fink and J.Küppers, Surf. Sci. **186**, p55 (1987); Surf. Sci. **193**, p259 (1988)

[59] N.V.Smith and D.P.Woodruff, Phys. Rev. **B25**(5), p3400 (1982)

[60] D.P.Woodruff, N.V.Smith, P.D.Johnson and W.A.Royer, Phys. Rev. **26**(6), p2943 (1982)

[61] P.D.Johnson and N.V.Smith, Phys. Rev. **27**(4), p2527 (1983)

[62] K.Desinger, V.Dose, M.Glöbl and H.Scheidt, Sol. St. Comm. **49**(5), p479 (1984)

[63] A.Goldmann, M.Donath, W.Altmann and V.Dose, Phys. Rev. **B32**(2), p837 (1985)

[64] R.F.Garrett and N.V.Smith, Phys. Rev. **B33**(6), p3740 (1986)

[65] R.Schneider, K.Starke, K.Ertl, M.Donath, V.Dose, J.Braunt, M.Graßand G.Borstel, J. Phys. Cond. Matter **4**, p4293 (1992)

[66] D.W.Jepson, F.J.Himpsel and D.E.Eastman, Phys. Rev. **B26**, p4039 (1982)

[67] D.P.Woodruff, S.L.Hulbert, P.D.Johnson and N.V.Smith, Phys. Rev. **B31**(6), p4046 (1985)

Chapter 5

Core-level photoemission study on the sodium-promoted oxidation of Al(111)

Contents

5 Core-level photoemission study on the sodium-promoted oxidation of Al(111) 147

5.1 Introduction 149

5.2 Theory 151

5.2.1 Background 151

5.2.2 Core level photoemission 154

5.2.3 Chemical shifts of core-levels 158

5.2.4 Energy Reference level 159

5.3 Sodium-promoted oxidation of Al(111) studied by core- level photoemission. 160

5.3.1 Previous Work 160

5.3.2 Experimental system 163

5.3.3 Experimental Results 164

5.3.4 Discussion 183

5.3.5 Conclusions 185

5.1 Introduction

The effects of alkali metal adsorption on metal surfaces have been extensively studied since the first pioneering work of Langmuir and co-workers in 1923 [1, 2] who observed large work function decreases with alkali metal coverage, and fast surface migration of the alkali metal. Later, they extended the research to coadsorption with oxygen observing a further decrease in the work function of the metal substrate [3]. The amount of interest in alkali metal adsorption and coadsorption has increased with the diversity of industrial applications. Alkali metals are used as promoters and modifiers in heterogenous catalysis in many industrially important reactions such as the Fischer-Tropsch synthesis of hydrocarbons from CO/H_2 mixtures [4] and the synthesis of ammonia from N_2/H_2 [5]; by promoting the catalyst with alkali metal containing additives, a superior selectivity and/or reactivity of the catalyst can be achieved [6]. In the development of photocathodes (the original aim of Langmuir), the use and effect of alkali metals is still the subject of intense research activity such as in the production of spin polarised electron sources (GaAs for example, when dosed with Cs and O can attain a negative electron affinity and when irradiated with circularly polarised light becomes a concentrated source of polarised electrons)[7]. The possible use of alkali metal additives in the dry oxidation of semiconductor surfaces through the promotion of the surface oxidation is also of current interest, although the difficulty in removing the alkali following the oxidation together with the effects of the alkali metal on the electronic properties of the material, may prevent practical exploitation. The industrial applications of the oxidation of metals are also

numerous, with the interaction of O with Al surfaces being a good example of protective oxide formation (this being important in structural applications such as the bonding of aluminium parts in the airplane industry [8]). In addition to alkali metal promoted oxidation of metal surfaces, work has been pursued on other metal adsorbate promoted oxidation including the use of rare earth additives. The adsorption of alkali metals on metals and semiconductors has produced a number of interesting effects in addition to those observed by Langmuir; these include the two dimensional ordering of alkali adatoms, charge transfer, altered surface reactivity and bond energy changes. The effect of the alkali metal adsorbate on the electronic structure of the surface has significance in electron emission, substrate bonding, local bonding and reactive properties [6].

In experimental studies aiming to clarify the mechanism of catalytic reactions on transition metal surfaces, one of the chief problems has been to separate the contributions of the s, p and d states. In order to simplify the problem, other simpler metal substrates have been used, in particular aluminium (polycrystalline and single crystal surfaces). Aluminium has no occupied d states, and has a free electron like valence band made up by mainly s and p symmetric states [9]; the electronic structure can be adequately modelled with the jellium model [10]. In this chapter, the influence of pre-adsorbed sodium on the early stages of oxidation of Al(111) has been investigated using synchrotron radiation photoemission measurements of the Al and Na 2p states. A strong promotion of the rate of oxygen dissociation and formation of three-dimensional oxide has been observed that is induced by the presence of the sodium. At a sodium coverage of $\theta_{Na} \approx 0.33$

monolayers (corresponding to the Al(111)($\sqrt{3} \times \sqrt{3}$)$R30°$-Na phase), the Al 2p chemically shifted states characteristic of the chemisorption precursor to oxidation seen on the Na-free surface are no longer seen. A state of intermediate chemical shift is however seen in the Na 2p photoemission spectrum at much lower oxygen exposures, and is characteristic of a new oxidation precursor.

Section(5.2) discusses the photoemission process and the implications concerning chemically shifted core-level states with Section(5.3) presenting and discussing the experimental results together with conclusions obtained.

5.2 Theory

5.2.1 Background

The photoelectric effect was originally observed by Hertz in 1887, when it noticed that material exposed to electromagnetic radiation of high enough energy (or short enough wavelength) would emit electrons [11]. The photoelectric or photoemission effect is defined by the Einstein relation [12] (see eqn(5.1)) which equates the maximum kinetic energy of the emitted electron to the quantised amount of light energy ($\hbar\omega$) minus the minimum work necessary for an electon to escape the emitter (i.e the work function ϕ).

$$E_{kin} = \hbar\omega - \phi \tag{5.1}$$

Equation(5.1) does not however, account for all the observed features in the photoemission spectrum; this is discussed in this section. Although the process of photoemission is not a new concept, it was not until the early 1970's that

photoemission spectroscopy (PES) became intensely used for the study of solids and surfaces [13].

The early work in photoemission was conducted at low energies using ultra-violet radiation (UPS) typically from He gas discharge line sources (HeI and HeII line energies of 21.2eV and 40.8eV). In this low energy regime only the valence band is generally accessible, and in order to observe the highly localised core levels much higher incident photon energies (X-ray range) are required. The typical laboratory X-ray source for photoemission relies on the K_α emission of Mg or Al, with energies of 1253.6eV and 1486.6eV respectively. Because of the different available photon sources (ultra-violet or X-ray) the techniques were labelled ultra violet photoemission and X-ray photoemission spectroscopy (UPS and XPS), with the former regarded as valence band photoemission and the latter mainly used for core level photoemission spectroscopy [13, 14, 15], (Fig(5.1) shows the two processes). The development of synchrotron radiation sources with the ability to utilise a whole range of photon energies made the distinction superfluous (for example, the experimental results presented in this chapter arise from a core level study using photon energies in the range 90-110eV). Since the experimental photoemission work presented is a core level investigation, it is mainly aspects of XPS that are detailed here.

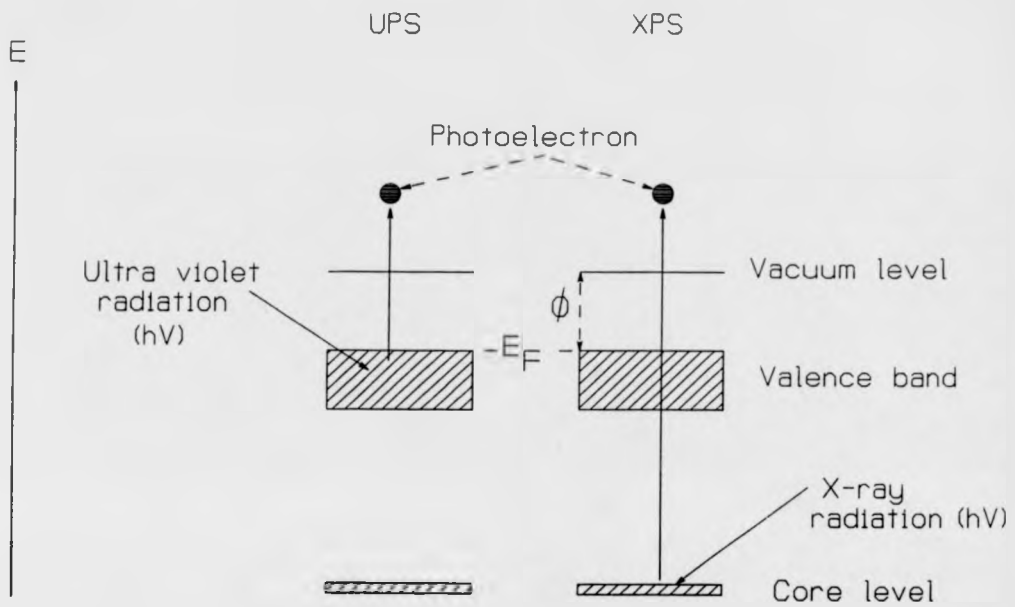

Fig 5.1 : Comparison of Ultra violet and X-ray photoemission processes (UPS and XPS).

5.2.2 Core level photoemission

An extension of Einstein's equation (5.1) that considers not only the highest energy electrons, but all of them is shown in eqn(5.2). In this case the total energy of the photon is absorbed by a single electron of binding energy $-E_b$. See [14].

$$E_K = \hbar\omega - E_b \tag{5.2}$$

The kinetic energy (E_K) and binding energy (E_b) are defined relative to the Fermi level. In the Hartree-Fock approximation [16, 17, 18], the binding energy of the electron is calculated by subtracting the total energy of the system in its ground state from the total energy after photoemission (i.e. in its ionised state) assuming that the system is 'frozen' (see eqn(5.3)).

$$E_b^{HF} = E^{HF}(N) - E^{HF}(N-1) \tag{5.3}$$

The energy E_b^{HF} (Koopmans energy) calculated in this manner is rather inaccurate when approximating to core level energies, but does have some success in calculating the energy of valence band states [17]. The reason for this inaccuracy is that when calculating the total energy of the systems it is assumed that there is no electron interaction, hence the electrons near the photoemitted electron are considered static during the process [16, 17, 19, 20, 21]. In reality, the surrounding electrons in the atom relax to screen the core hole left by the photoelectron (so called intra-atomic relaxation [22]). This has the effect of increasing the energy of the photoelectron by an amount E_a, therefore eqn(5.2) becomes

$$E_K = \hbar\omega - E_b + E_a \tag{5.4}$$

So far it has been assumed that the photoemission process occurs slowly, and a stable equilibrium is reached (the 'adiabatic' approximation). If, as is the case, the process is taken to be rapid (the perturbation to the system 'turned on' quickly), then the 'sudden' approximation provides a more realistic representation [14, 23]. In this case, the final state could be one where an electron (other than the photoelectron) occupies an excited bound state of the atom (shake up), or an electron is ejected into an unoccupied state above the vacuum level (shake off). These processes leave less energy for the photoelectron, and are responsible for lower energy satellites observed in the resulting spectra [13, 14, 20, 23], a schematic of these processes is shown in Fig(5.2).

A second relaxation effect beyond that of an isolated atom is the interatomic relaxation [13, 14, 23]. This is due to the screening by the weakly bound and highly mobile valence band electrons in the surrounding solid which also acts to increase the energy of the photoelectron by an amount E_r, see eqn(5.5)

$$E_K = \hbar\omega - E_b + E_a + E_r \tag{5.5}$$

The results of both the adiabatic and sudden approximation are shown schematically in Fig(5.2); the latter being closer to the truth than the former. In general, the loss mechanisms which give rise to structure at lower kinetic energy to the photoemission peak can be categorized as due to losses by intrinsic or extrinsic processes [13, 17].

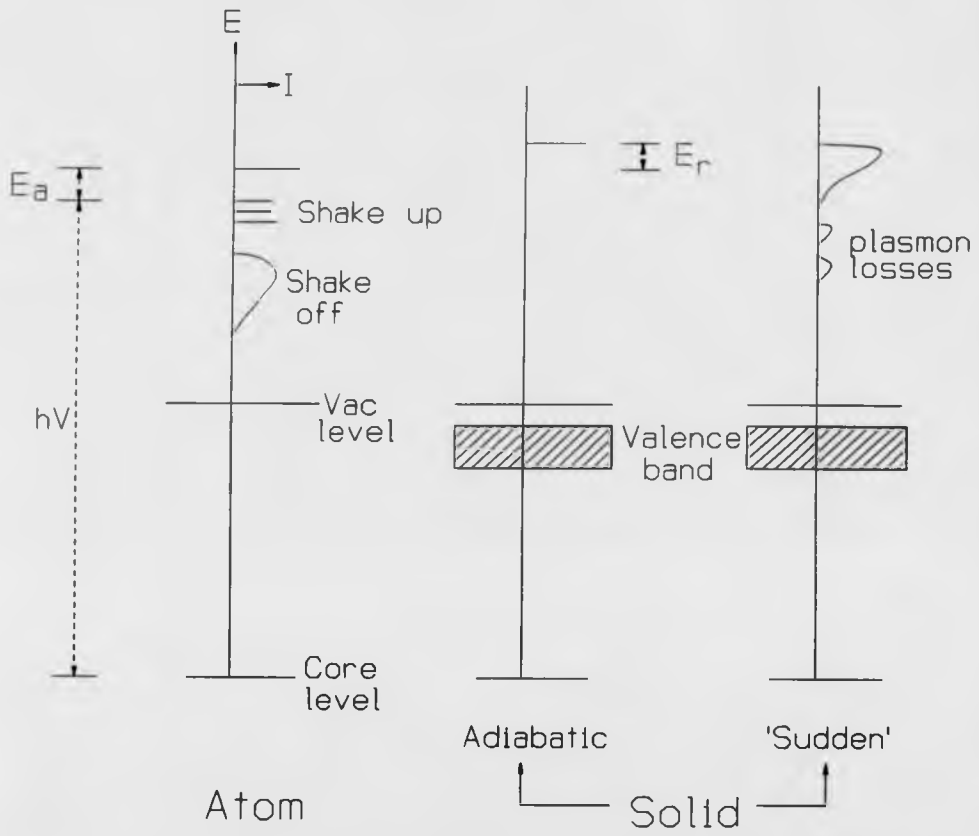

Fig 5.2 : Comparison of core level photoemission from an atom and a solid. For photoemission from a solid, both the adiabatic and sudden approximations are illustrated. E_a and E_r are the intra-atomic and interatomic relaxation energies respectively [14].

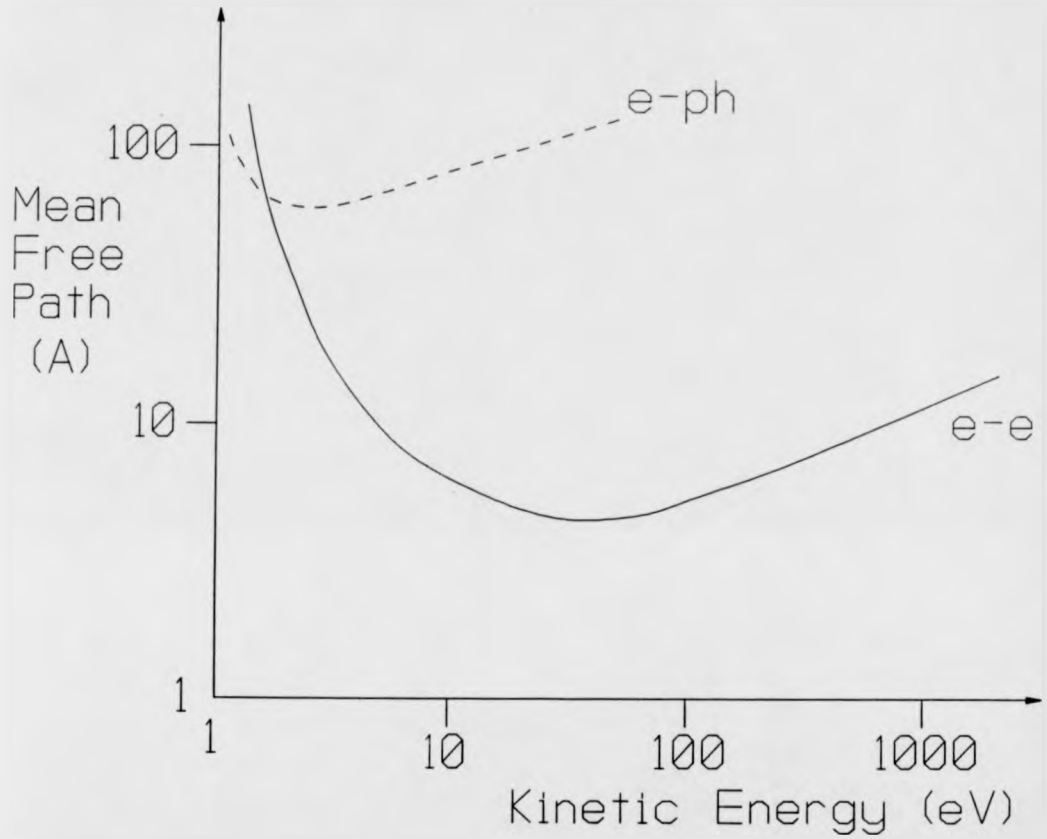

Fig 5.3 : Graph of electron mean free path ($\dot{A}$) versus kinetic energy (eV) for electron-electron and electron-phonon scattering [13].

Intrinsic losses are those that occur during the photoemission process, such as electron-hole pair creation around the Fermi energy which together with the 'shake up' and 'shake off' processes produce a characteristic inelastic tail to the main peak. Another intrinsic loss is produced by the creation of bulk and surface plasmons during excitation (plasmon losses), which give rise to plasmon loss features at kinetic energies below the inelastic tail (see Fig(5.2)) [14, 20, 24]. Extrinsic losses are due to inelastic collisions as the photoelectron follows it route to the surface; these also contribute to the electron-hole (e-h) and plasmon loss structure. Fig(5.3) shows the electron inelastic scattering mean free path as a function of E_K (for metals) for electron-electron and electron-phonon scattering. The photoelectrons that form the main peak therefore, have undergone little or no inelastic collisions and are generally from the top few monolayers, establishing the surface specificity of the process [13].

5.2.3 Chemical shifts of core-levels

The binding energies of the core level electrons observed using photoemission, are very sensitive to both the electronic environment and the relaxation energy changes that can occur with alteration of nearest neighbour separation, and/or chemical species [13, 14, 16, 17, 18, 20].

The observed chemical shifts are not due to one particular contribution, but rather from a combination of initial and final state effects. The final state effects have already been discussed, and consist of changes to the electronic environment induced by the creation of a core hole in the photoemission process (these are

the intra-atomic and interatomic relaxation effects). The initial state effects are due to changes in the electronic environment prior to the photoemission process (occurring for example, through adsorption and chemical interaction)[17, 18]. If the potential in the core of an atom is directly influenced by a variation in the initial state charge density, then a change in potential will shift the core level eigenvalues. This shift can be determined using the Hartree-Fock approach of calculating eigenvalues of the initial state charge densities (i.e for $E^{HF}(N)$ and $E^{HF}(N-1)$, see eqn(5.3)), and taking the difference [13]. Using this method assumes a static (or smeared) field of the other electrons in the system. The theory surrounding this technique of deriving the initial state contribution through the core level eigenvalue shift is well documented in theoretical studies [25].

In the methodology of the experiment presented in this chapter, the observed chemical shift of core level binding energies cannot be separated into initial and final state components, and it is the number of different chemically shifted states, and their relative intensities observed (together with other related information such as adsorbate coverage) that is used to provide a 'fingerprint' of the adsorbate-substrate interaction.

5.2.4 Energy Reference level

Conscious of the sensitivity of the peak position to these factors, it is necessary in a core level study (for example involving adsorption) to have knowledge of the absolute positions of peaks in the clean system of both substrate and adsorbate species before any comparison with observed shifted peaks (which may

subsequently be identified with certain stages in the interaction). The question of whether to reference these binding energies to the vacuum level or the Fermi level is much discussed [13, 14, 17, 16]. The vacuum level is generally not used due to variations in the work function of the substrate during adsorption, and also because of the complexities of accounting for the contact potentials in the experimental system. Referencing to the Fermi level (at least in metals) is much the favoured option, as the Fermi level can be defined as the energy cut off in the photoemission spectra (i.e. the limit of occupied states) and is actually observed in all of the spectra.

5.3 Sodium-promoted oxidation of Al(111) studied by core- level photoemission.

5.3.1 Previous Work

The general theory behind the adsorption of alkali metals on metal surfaces was first presented by Gurney [26]. In this model, the valence *s* electron of the alkali metal hybridises with the upper states of the valence band of the substrate metal broadening the *s* state and lowering it in energy such that the alkali metal loses part of its *s* electron to the substrate. As a consequence of this, the electrostatic potential around the alkali adatom will lower, leading to a work function decrease. This picture treats the alkali adatom as being partly ionic at low coverages, with the alkali atoms forming dipoles at the surface and having an even distribution (due to dipole-dipole repulsion and fast surface migration). After a certain alkali

coverage is reached, the dipole-dipole interaction causes a mutual depolarization effect that eventually cancels out the decrease in work function due to the increase in alkali adatoms (corresponding to the work function minimum), with further alkali adsorption resulting in an increase in substrate work function and formation of a metallic alkali layer [27]. This model has been refined by Lang and Williams [28], and by Muscat and Newns [29], with further corroboration through the calculations of Muscat and Batra [30]; Serana *et al* [31] and by Persson and Dubois [32].

The oxygen-aluminium system has been studied extensively in recent years with many conflicting results. Early work was conducted on polycrystalline aluminium and later on the single crystal surfaces [9]. Yu *et al* measured valence band photoemission after oxygen adsorption and found that the workfunction of the Al film did not change for small oxygen coverages, leading them to conclude that O penetrates into the Al surface resulting in a disappearance of the z-component of the O dipole moment [33]. In agreement with Yu*et al*, Eberhardt and Kunz concluded from photoemission experiments that O penetrates into the aluminium surface especially for the (100) surface [9]. Flodström *et al* measured the Al 2p photoemission for the (111) and (100) surfaces, and observed (in the (111) case) an intermediate oxidation state (with a chemical shift of 1.4eV) prior to final oxidation (shift of 2.7eV) and interpreted this as being due to O atoms sitting on the surface. For the (100) surface, no intermediate state was observed [34]. Flodström *et al* also presented evidence that this two step oxidation process was unique to the (111) surface, and showed for the first time that an ordered

oxygen overlayer exists on an fcc metal (the oxygen occupying a three fold hollow site on the (111) surface with no Al atom underneath in the second Al layer) [35]. By 1981, although adsorption on Al(100) and Al(110) seemed to be generally understood, the more complex Al(111) surface had acquired several models (from ordered overlayers to random overlayers and overlayer/underlayer combinations [36]) to explain the process. Soria *et al* using LEED and AES concluded that the interaction of oxygen with Al(111) was in fact a four stage process [36]. The intermediate chemisorption state that was observed originally by Flodström *et al* on the Al(111) surface [34] has been associated with an ordered (1×1) phase with the oxygen atoms occupying the three fold coordinated hollow site [35, 37]. From a room temperature study of O on Al(111) using synchrotron radiation photoemission measurements of the Al 2p state, McConville *et al* observed four chemically shifted Al 2p peaks [38] which were assigned to surface aluminium atoms bonding to one, two and three oxygen atoms, with the fourth peak (experiencing the greatest shift) assigned to the oxide. More recent O 1s X-ray photoelectron spectroscopy (XPS) [39] and scanning tunnelling microscopy (STM) [40] investigations have provided further confirmation of these assignments.

The promotion of the oxidation of metal and semiconductor surfaces by coadsorbing alkali metals is well known [6]. However, the actual interaction of the alkali metal with the substrate and the mechanism behind the increased oxidation rate are not completely understood. The alkali metal is known to reduce the work function of the substrate, and increase the dissociation rate of the oxygen molecules at the surface. It has been proposed that once a thin oxide layer exists

on the surface, electrons tunnelling through the layer from the substrate Fermi level to the affinity level of the adsorbed oxygen ion have the effect of reducing the barrier for oxygen penetration into the aluminium [41]. It has also been proposed that the work function decrease is not caused by charge transfer to the substrate, but by a strong polarisation of the alkali metal overlayer [41]. The main controversy surrounding the adsorption of alkali metals like sodium on metal surfaces such as aluminium occurs in the sub-monolayer regime. Gurney's original picture proposes that the alkali metal forms an ionic bond with the substrate (i.e charge transfer occurs from alkali metal to substrate to form local dipoles). There is plenty of evidence to support this theory from photoemission [42] and inverse photoemission [43] results, with the formation of two dimensional bands observed for Na [44] confirming the metallic character of the multilayer alkali adsorbate. However, Ishida and Terakura [45] have recently proposed that the bonding is initially covalent (or neutral), maintaining that there is a charge shift but not a charge transfer to the substrate. Using local-density-formalism pseudopotential calculations, they suggest a strong covalency of the alkali metal to substrate bond which is independent of the alkali metal coverage (with no change to the energy of occupied and unoccupied valence levels). The debate behind the ionic/covalent bonding is ongoing and is not dealt with in further detail here.

5.3.2 Experimental system

The experiments were performed on beam line 6.1 of the Daresbury synchrotron radiation source; the system having being described in Chapter(2). The Al(111)

crystal was prepared by a combination of X-ray Laue orientation, spark machining, mechanical polishing and *in situ* cycles of argon ion bombardment ($\approx 2keV$ for 30 mins) and annealing (650 K for similar time). A clean well-ordered surface was produced as established by Auger electron spectroscopy (AES) and low energy electron diffraction (LEED) (the clean surface showing a sharp (1×1) pattern). Sodium was deposited from a SAES getter source mounted approximately 5cm from the sample. Prior to deposition the getter source was thoroughly outgassed, with deposition effected at fixed heating currents (5 to 6 A) through the getter for various periods of exposure to the sample which allowed controlled amounts of sodium ($< 0.1ML$) to be deposited. The sodium coverage was estimated from the relative Al and Na 2p core level photoemission signals and Auger intensities, with the coverage of $\theta_{Na} \approx 0.33$ monolayers, corresponding to the ordered $(\sqrt{3} \times \sqrt{3})R30^{o}$ LEED pattern, used as calibration point.

Oxygen exposures were attained by exposing the sample to oxygen gas in the chamber via a leak valve at pressures in the range 1×10^{-8} to 1×10^{-7}mbar dependent on size of exposure required. For both sodium and oxygen dosing, the sample was maintained at room temperature.

5.3.3 Experimental Results

5.3.3.1 Oxidation of Al(111)

A series of Al 2p photoemission spectra were taken at a photon energy of 100eV from a clean Al(111) surface following different oxygen exposures. The spectra were normalised to the reference electron beam current of the storage ring and

set out in order of exposure in Fig(5.4). In the spectrum from the clean Al(111) surface the 2p spin-orbit split doublet is clearly visible. At the highest oxygen coverage ($\approx 1000L$) the original Al 2p doublet is no longer visible, the spectra being dominated by a broad peak (the spin-orbit splitting not observed) which is chemically shifted by approximately 2.6eV relative to the metallic (clean surface) peaks. This feature has been widely attributed to the surface oxide. At the intermediate exposures, several other peaks are observed which have undergone intermediate chemical shifts with respect to the final oxide chemical shift. Previous measurements have shown that there are in fact three intermediate states (having chemical shifts of approximately 0.5, 1.0 and 1.5eV) [38]. Since the difference between these chemical shifts is similar to the spin-orbit splitting, the $2p_{1/2}$ feature of one state overlaps the $2p_{3/2}$ peak of the next and so on, therefore it may appear that there are only one or two intermediate states present. The relative intensity of each of these peaks indicates a sequential filling of these states as the oxygen is taken up by the aluminium surface. This interpretation for the intermediate chemisorbed states has been supported by O 1s XPS [39] and STM [40] studies. It is also clear from Fig(5.4) that there is some intensity increase of the final oxide state occurring prior to the saturation of the chemisorption phase. The XPS and STM results indicate that saturated (1×1) chemisorption phase islands are formed on the surface in preference to a random filling of sites.

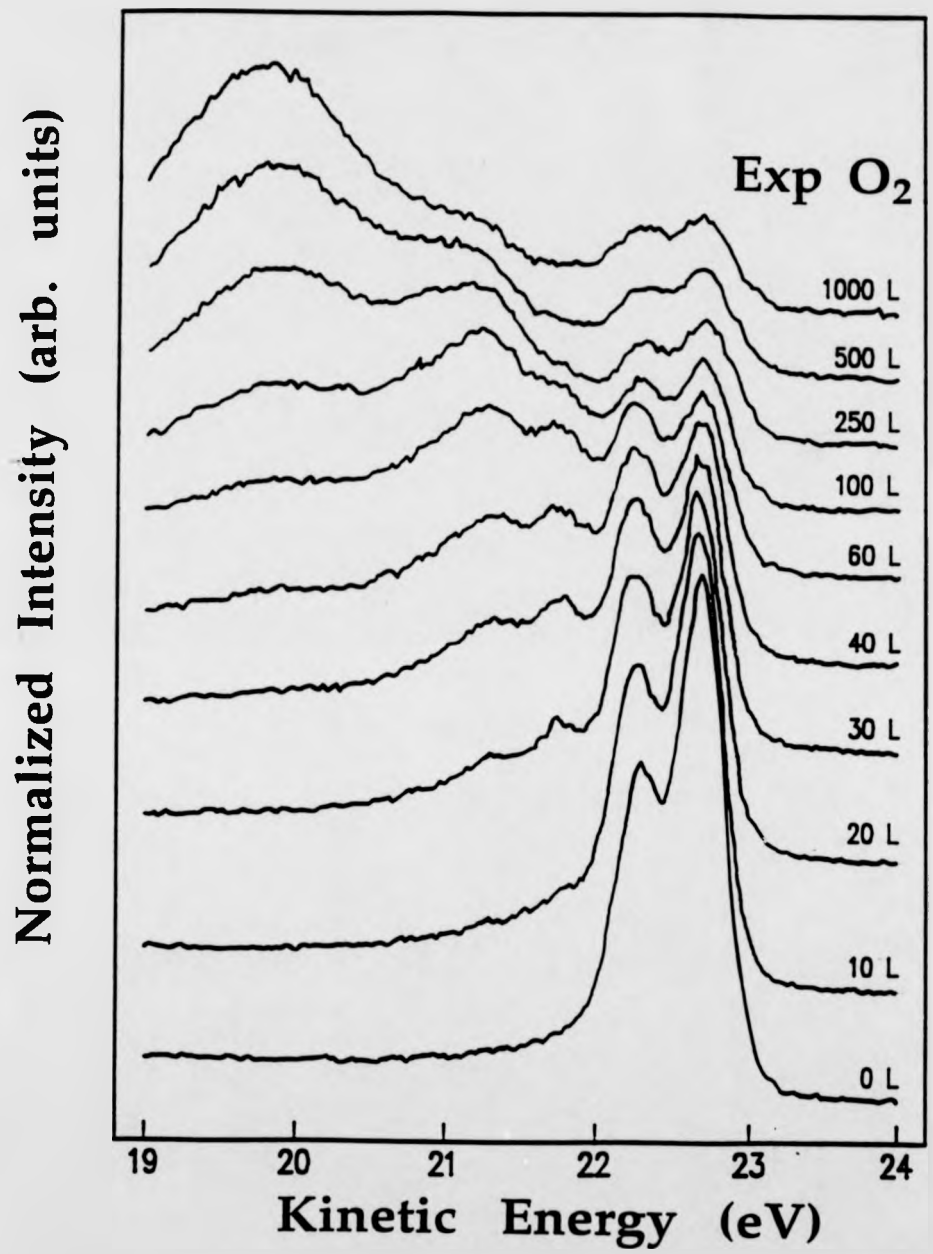

Fig 5.4 : Al 2p photoemission spectra from Al(111) with increasing oxygen exposure.

5.3.3.2 Oxidation of $Al(111)(\sqrt{3} \times \sqrt{3})R30^{o}$-Na surface

The clean Al(111) surface was predosed with sodium to a coverage of $\theta_{Na} \approx 0.33ML$, and subsequent LEED measurements showed a $(\sqrt{3} \times \sqrt{3})R30^{o}$ LEED pattern. Auger electron spectra were taken for later use in calibrating other sodium dosages. Al 2p and Na 2p photoemission spectra were taken for increasing oxygen exposures.

Fig(5.5) shows the Al 2p spectra for oxygen exposures from 0 to 1000 L. Comparing these spectra to the data in Fig(5.4), it can be seen that the intermediate chemically shifted peaks are no longer visible, and that the broad peak associated with the final oxide appears at a much lower exposure ($\approx 4 - 5L$). Comparison of the relative magnitudes of the oxide and metallic peaks for the 10 L exposure and the 1000 L exposure on the clean surface (Fig(5.4)) reveals a great similarity. From this, it can be estimated that the presence of the sodium enhances the oxidation rate by about a factor of 100. In the spectrum corresponding to the 1000 L exposure in Fig(5.5), the total area of the broad oxide peak is much greater than that of the metallic state peaks of the clean spectrum (Fig(5.4)). Since all the spectra are normalised to constant incident photon flux, this net increase in photoemission intensity can be attributed to the growth of surface oxide multilayers (the inelastic scattering mean-free-path being greater in the oxide than in the metal)[46].

In order to establish reasons for the disappearance of the intermediate chemisorbed states in the spectra of Fig(5.5), it is necessary to consider the structure of the $(\sqrt{3} \times \sqrt{3})R30^{o}$ phase associated with the $\theta_{Na} \approx 0.33ML$ coverage.

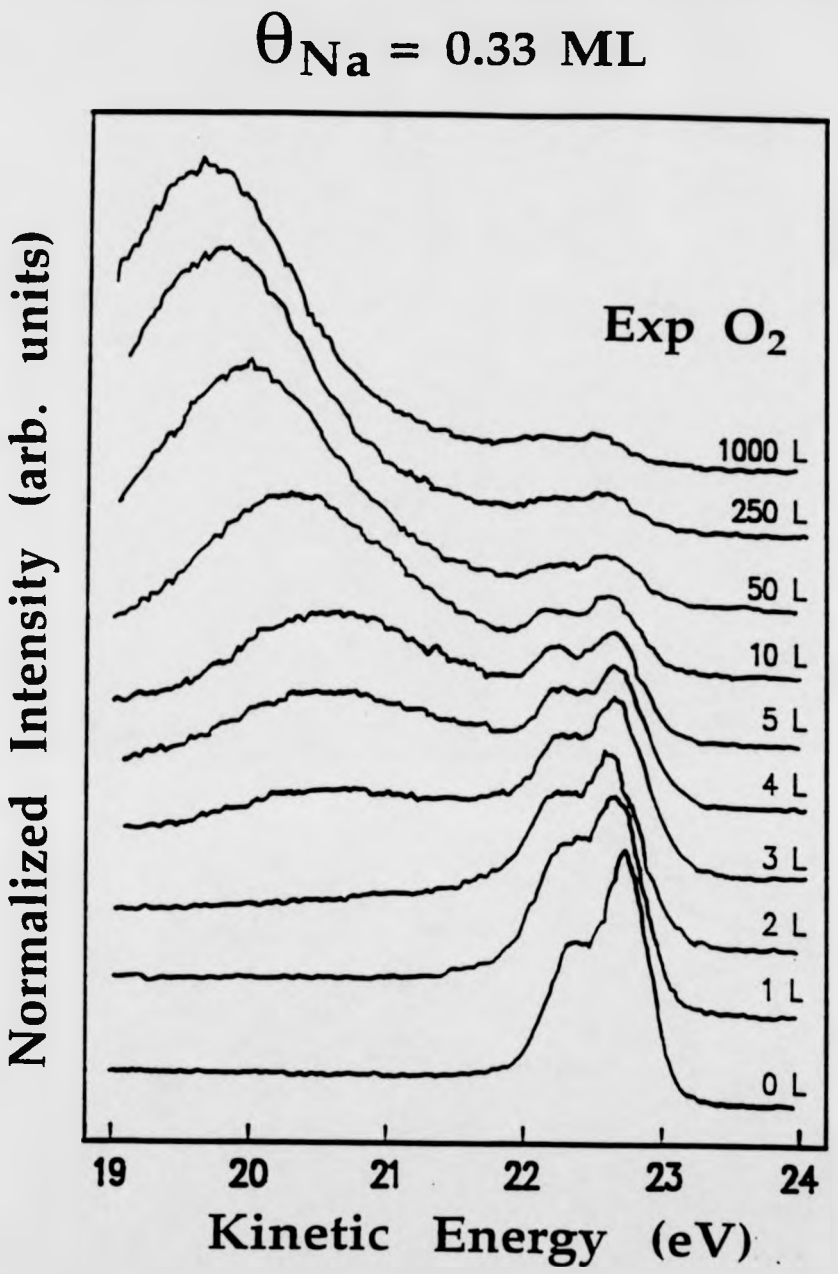

Fig 5.5 : Al 2p photoemission spectra from Al(111)($\sqrt{3} \times \sqrt{3}$)$R30°$-Na with increasing oxygen exposure.

This phase corresponds to a saturation of the surface layer (further sodium adsorption produces a (2×2) phase which appears to correspond to a double layer of mixed Al-Na alloy [47, 48]). For the $(\sqrt{3} \times \sqrt{3})R30^{o}$ phase, measurements using surface extended X-ray absorption fine structure (SEXAFS)[49] and normal incidence standing X-ray waves (NISXW)[48, 50] have indicated that the sodium atoms substitute top layer aluminium atoms such that each Al atom is surrounded by three Na atoms. This geometry is shown in Fig(5.6). If an oxygen atom adsorbs on this surface, adopting a surface site coordinated to 3 surface metal atoms, it would have 2 Al atom nearest neighbours and 1 Na atom neighbour making a very different environment from that of the clean surface. The missing intermediate chemisorption states in the Al 2p spectra of Fig(5.5) can therefore be assigned to adsorption site blocking by the Na atoms (see also section(5.3.4)).

For the same surface ($Al(111)(\sqrt{3} \times \sqrt{3})R30^{o}$-Na), Na 2p photoemission spectra were taken ($h\upsilon = 110eV$) for varying oxygen exposures (0 to 50 L), see Fig(5.7). With the increase of oxygen exposure, prior to the final oxide chemically shifted state of the 50 L exposure, there is evidence for an intermediate chemically shifted state. In Fig(5.8), the Na 2p photoemission spectra for the 4 L oxygen exposure is shown following analysis with a simple curve fitting program (the program allowing linear background subtraction and lineshape generation utilising Gaussian, Lorentzian and Doniach-Sunjic asymmetry functions). The original Na 2p contribution has virtually vanished (peak A), with the final oxide state shown chemically shifted by approximately 1.9eV (peak B).

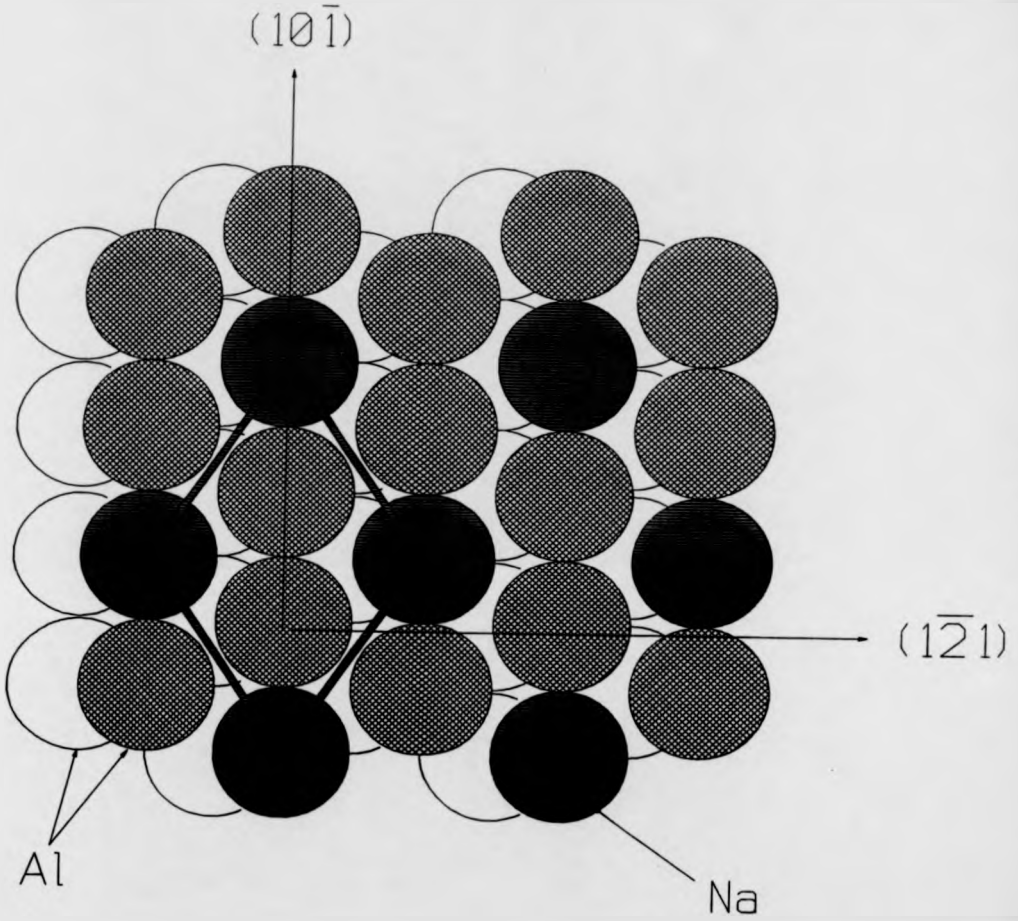

Fig 5.6 : Geometry of Al(111)($\sqrt{3} \times \sqrt{3}$)R30°-Na phase. The Na atoms substituting into the top Al layer.

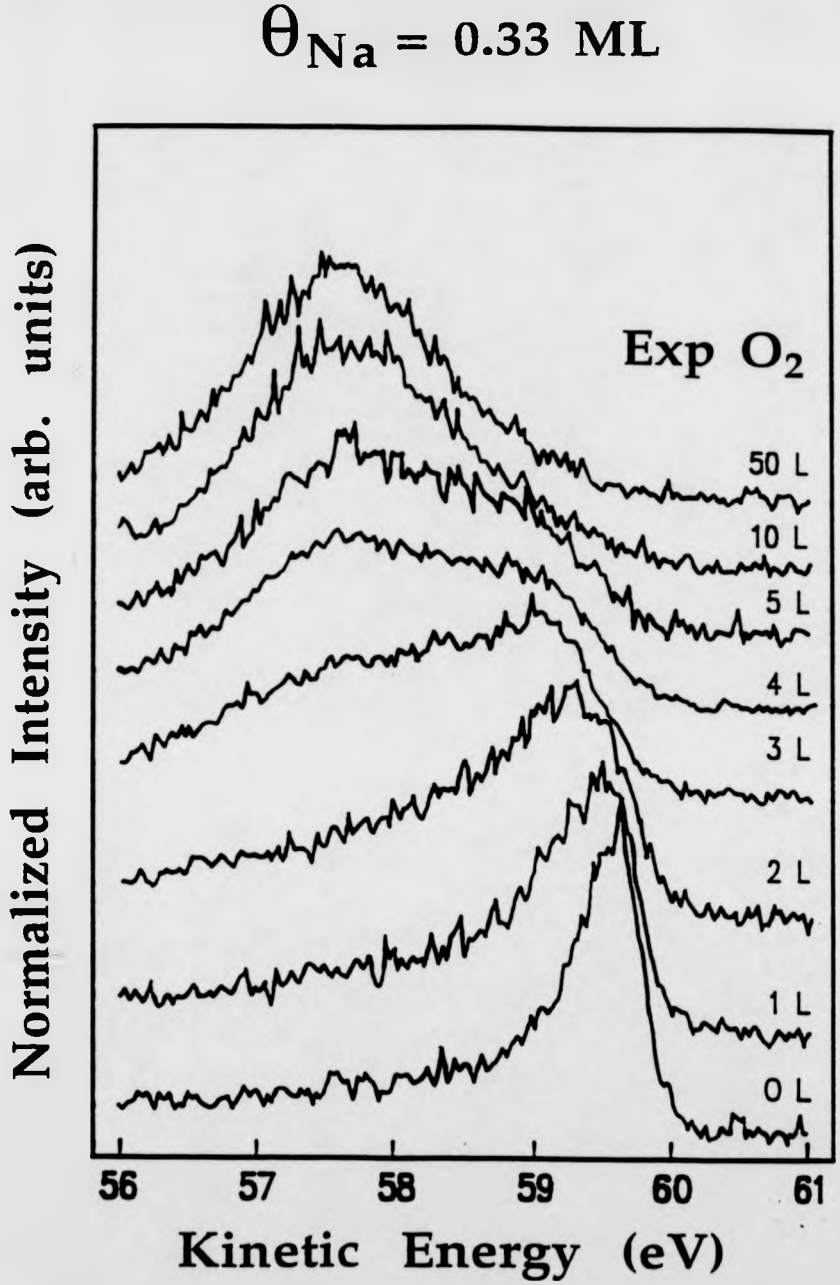

Fig 5.7 : Na 2p photoemission spectra from Al(111) $(\sqrt{3} \times \sqrt{3})R30°$-Na with increasing oxygen exposure.

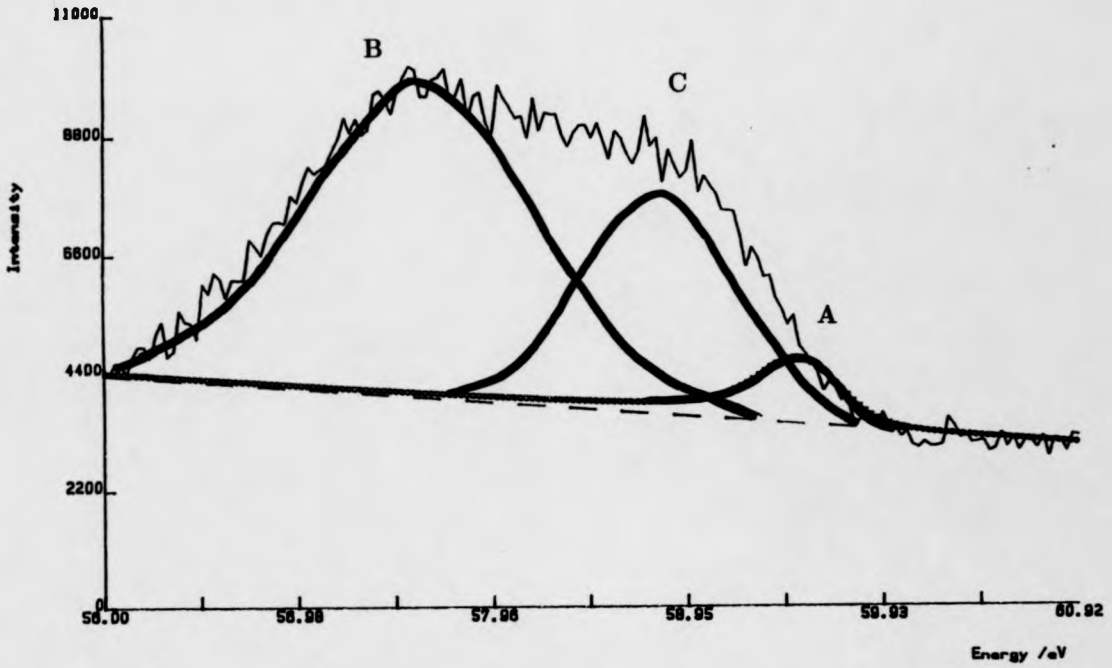

Fig 5.8 : Deconvolution of Na 2p photoemission spectra from Al(111)+($\sqrt{3} \times \sqrt{3}$)$R30°$− Na +5L oxygen.

The flat top of the original spectrum is seen as a signature of an additional peak, and in the case of the spectrum in Fig(5.8) is shown to be attributable to an intermediate chemically shifted peak (peak C), the chemical shift being approximately 0.7eV relative to the Na 2p energy prior to exposure to oxygen. This intermediate state observed in the Na 2p spectra passes through its highest intensity prior to the acceleration of the true oxidation state, in a similar way to the intermediate chemically shifted states in the clean Al 2p spectra of Fig(5.4). It would appear therefore that the chemisorption precursor to the final oxidation of Al(111) still exists, but with the local bonding (or charge transfer) now occurring between the O and Na atoms rather than the O and Al atoms.

5.3.3.3 Oxidation of Al(111) at intermediate Na coverages

Fig(5.9-10) show Al 2p photoemission spectra obtained following predosing of the clean Al(111) surface to 0.05 and 0.20ML of Na and various exposures of oxygen. For the $\theta_{Na} \approx 0.05ML$ predosed spectra, several of the chemically shifted intermediate chemisorption states are visible, comparing well with the unpromoted spectra in Fig(5.4). In the $\theta_{Na} \approx 0.20ML$ series of spectra, only the third intermediate chemically shifted state of the clean spectra is still visible. Both series of spectra (Figs(5.9-10)) show a great enhancement of the oxidation rate in comparison to those from the initially clean surface (Fig(5.4)); this is shown clearly in Fig(5.11) where a comparison of Al 2p spectra for various Na pre-doses and subsequent exposure to 10 L of oxygen are shown (the data taken from Figs(5.4-5) and Figs(5.9-10).

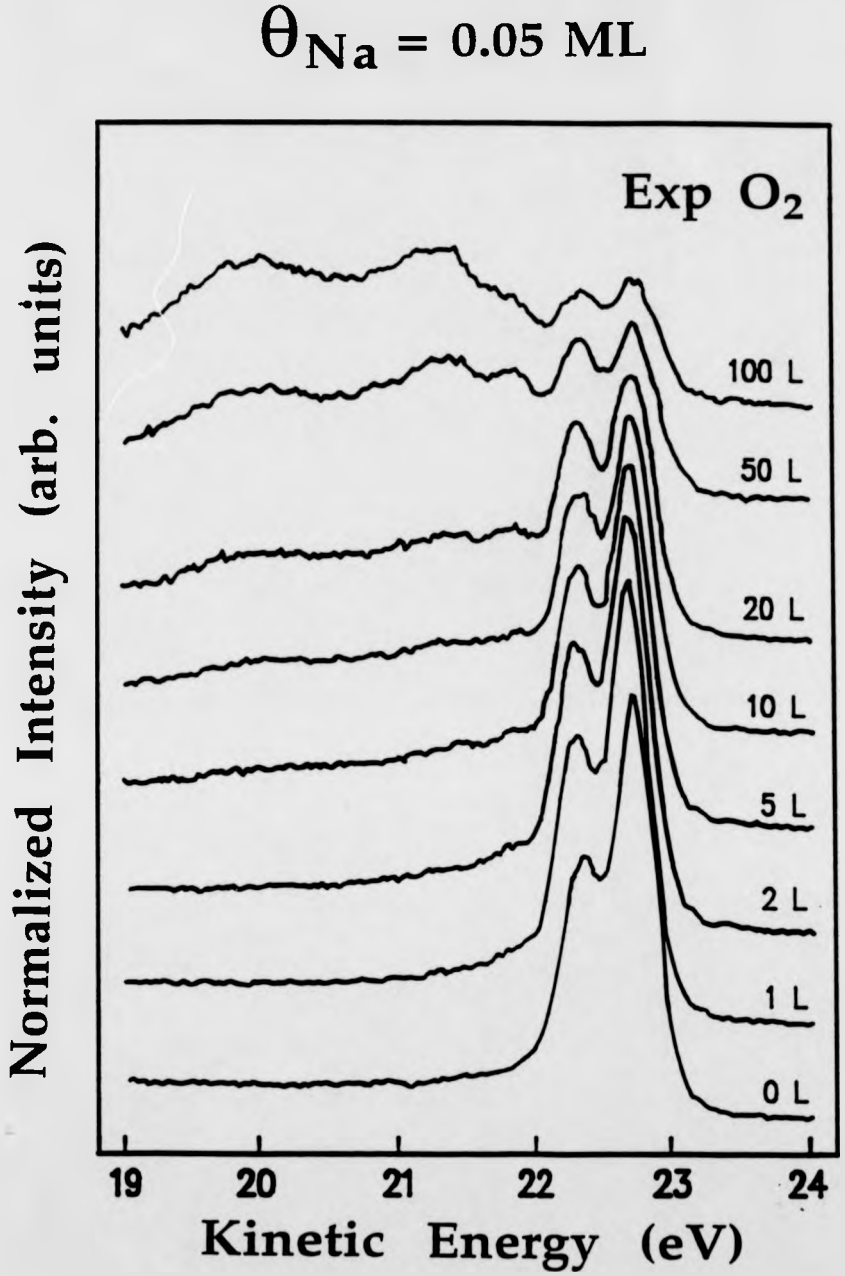

Fig 5.9 : Al 2p photoemission spectra from Al(111)+0.05MLNa with increasing oxygen exposure.

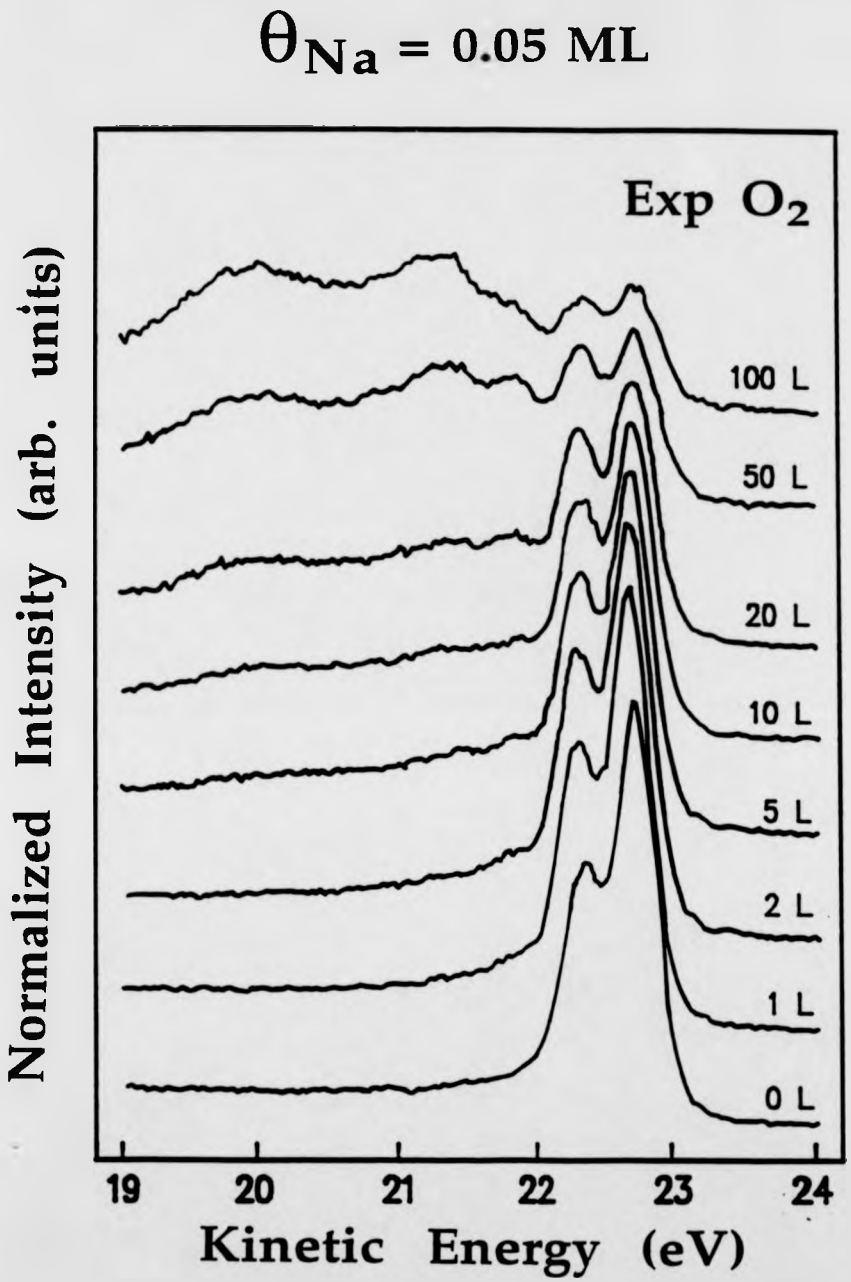

Fig 5.9 : Al 2p photoemission spectra from Al(111)+0.05MLNa with increasing oxygen exposure.

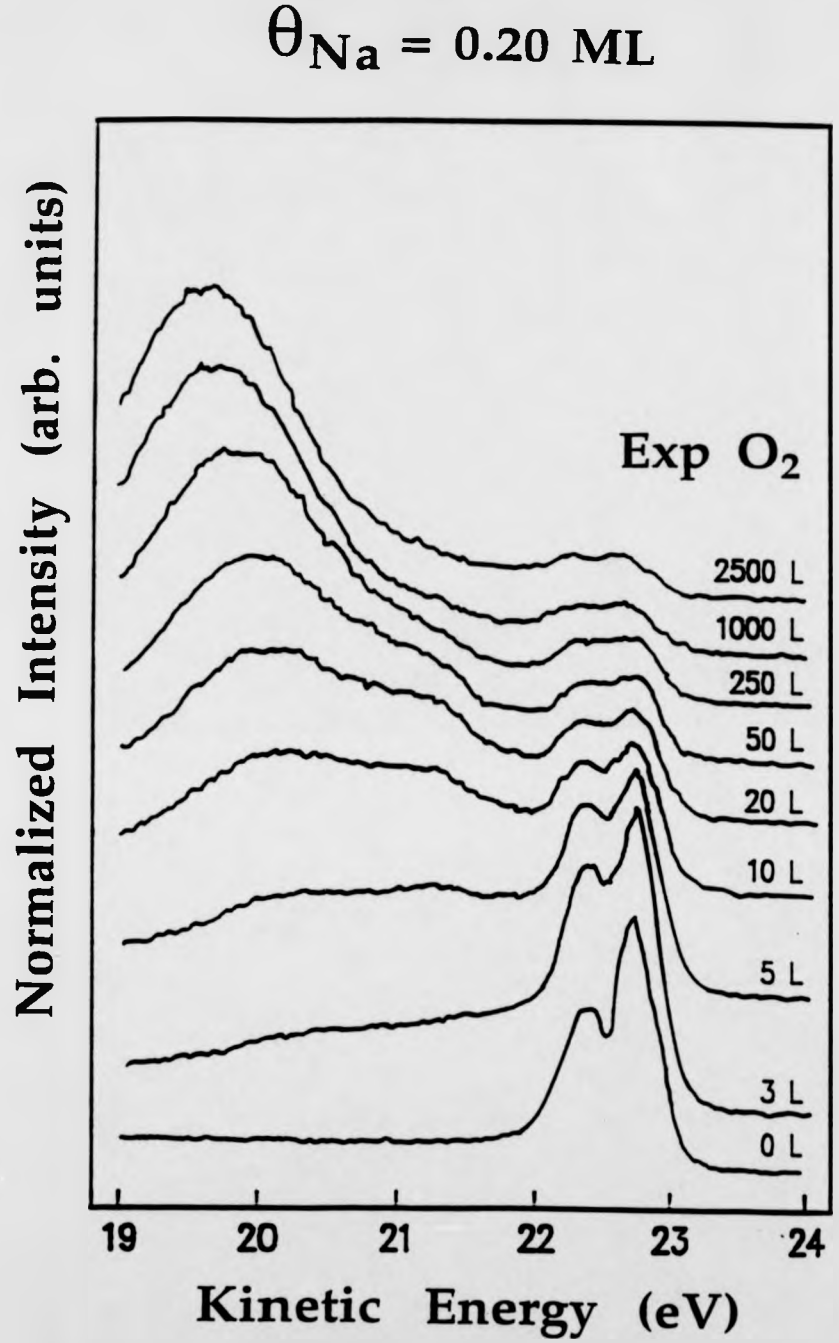

Fig 5.10 : Al 2p photoemission spectra from Al(111)+0.20MLNa with increasing oxygen exposure.

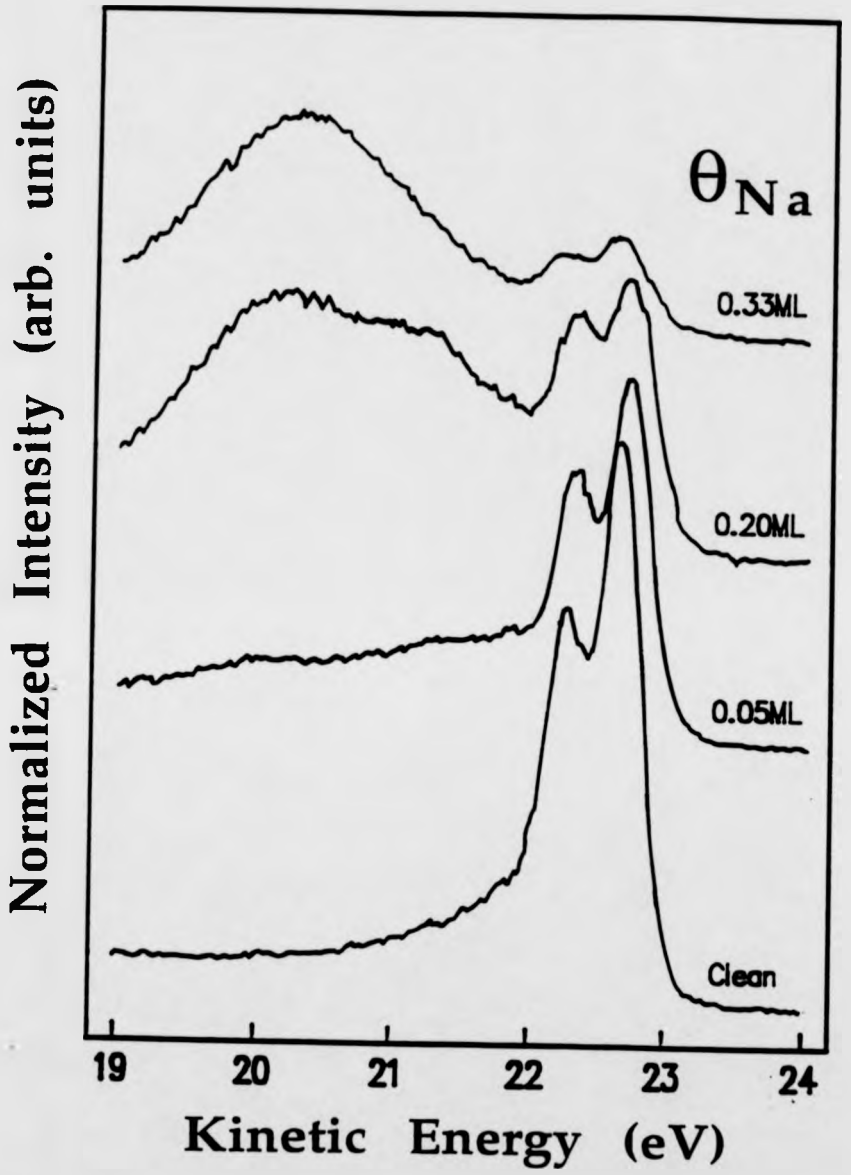

Fig 5.11 : Al 2p photoemission spectra from Al(111) with various predoses of Na prior to $10L$ oxygen exposure.

Fig(5.11) also shows evidence for enhanced oxygen uptake for the intermediate chemisorption states as well as the final oxide state in the intermediate Na pre-doses (ie $\theta_{Na} \approx 0.05$ and $0.20ML$).

The Na 2p photoemission spectra for the $\theta_{Na} \approx 0.05$ and $0.20ML$ pre-dosed Al(111) surface with varying oxygen exposures show a similarity to the $\theta_{Na} \approx 0.33ML$ spectra in Fig(5.7). Fig(5.12) shows the Na 2p spectra corresponding to the $\theta_{Na} \approx 0.20ML$ exposure with increasing oxygen exposure (0 to 2500 L). The spectra corresponding to an intermediate oxygen exposure (1 to 10 L) in which the Na 2p spectrum broadens and flattens, show the coexistence of the initial 2p state and the chemically shifted intermediate and final oxide state similar to those seen in Fig(5.7). The spectrum related to the 5 L oxygen exposure is shown in Fig(5.13) following the simple curve fitting procedure described earlier. The series of Na 2p spectra taken at a pre-dose coverage of $\theta_{Na} \approx 0.05ML$ had a very poor signal/noise ratio, but still showed evidence of a similar intermediate chemisorption state. Fig(5.14) shows spectra taken at oxygen exposures of 1 L, 5 L and 50 L; Despite the poor quality of the spectra, the slope in intensity from the clean surface to the oxide state, with an intermediate broadened flat peak, is clearly discernible.

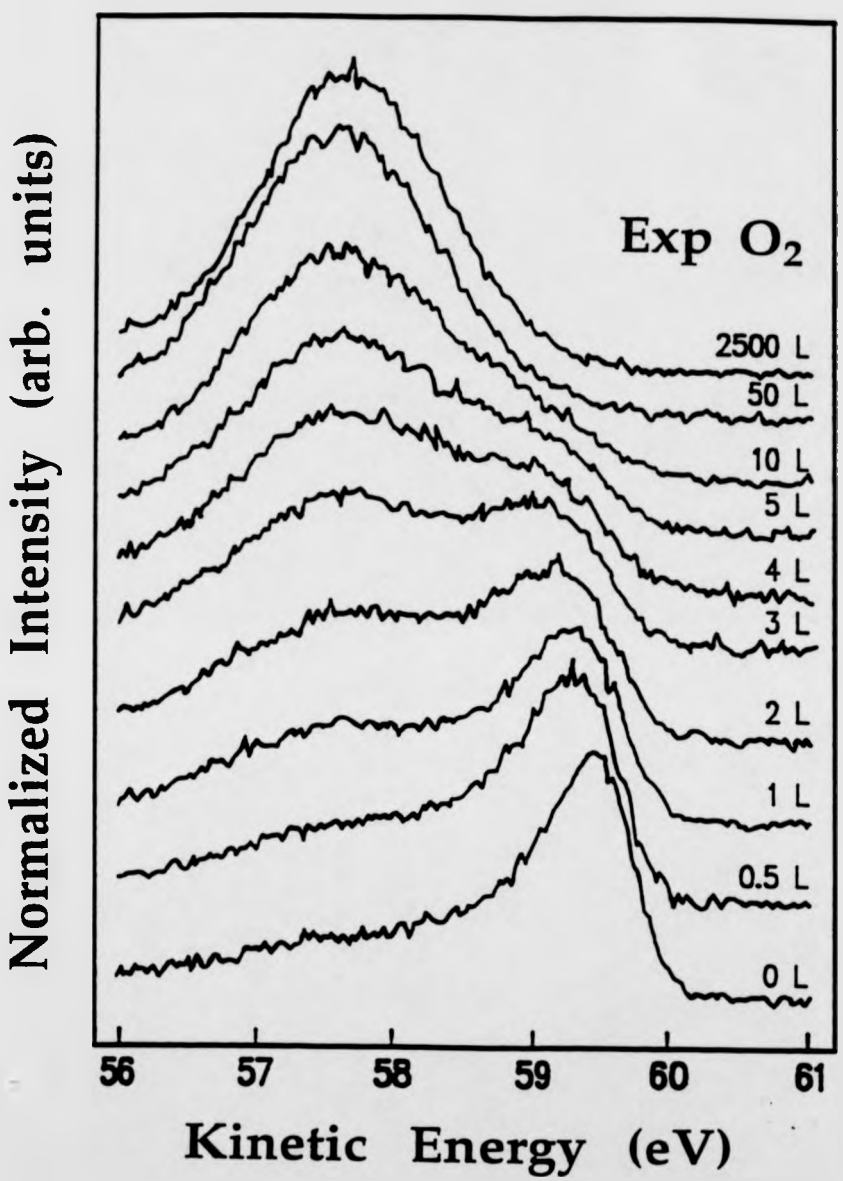

Fig 5.12 : Na 2p photoemission spectra from Al(111)+0.20MLNa with increasing oxygen exposure.

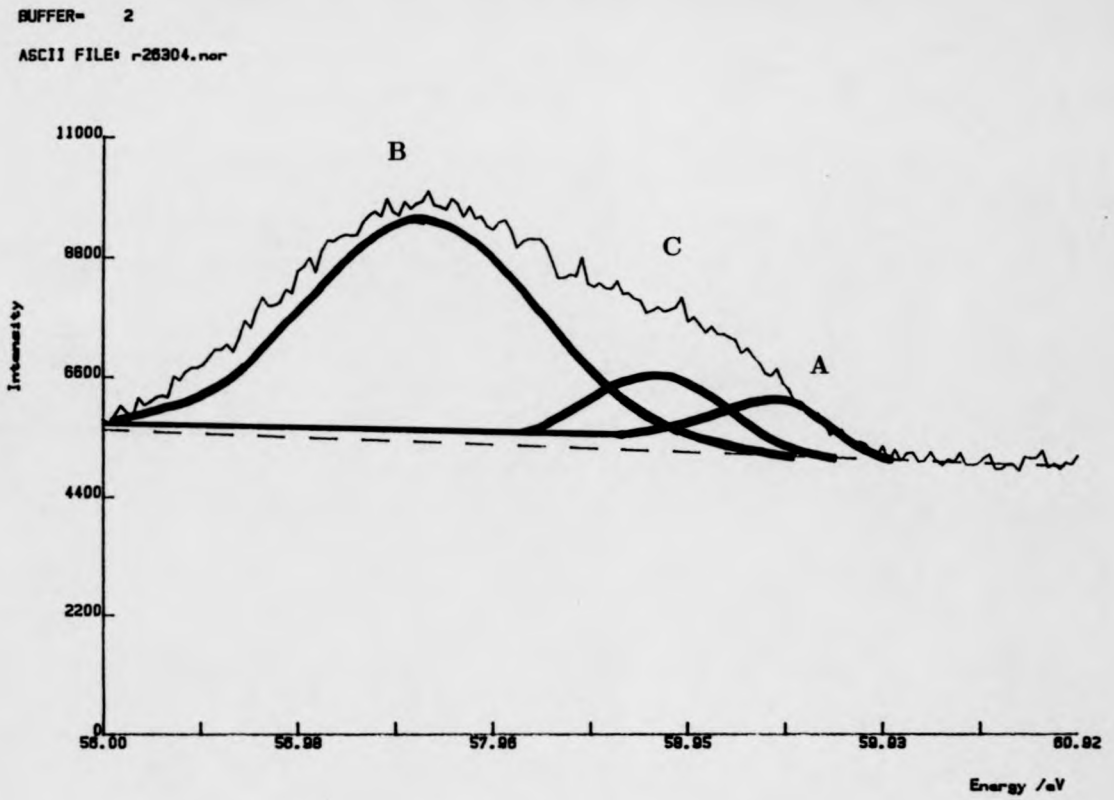

Fig 5.13 : Deconvolution of Na 2p photoemission spectra from Al(111)+0.20MLNa +5L oxygen.

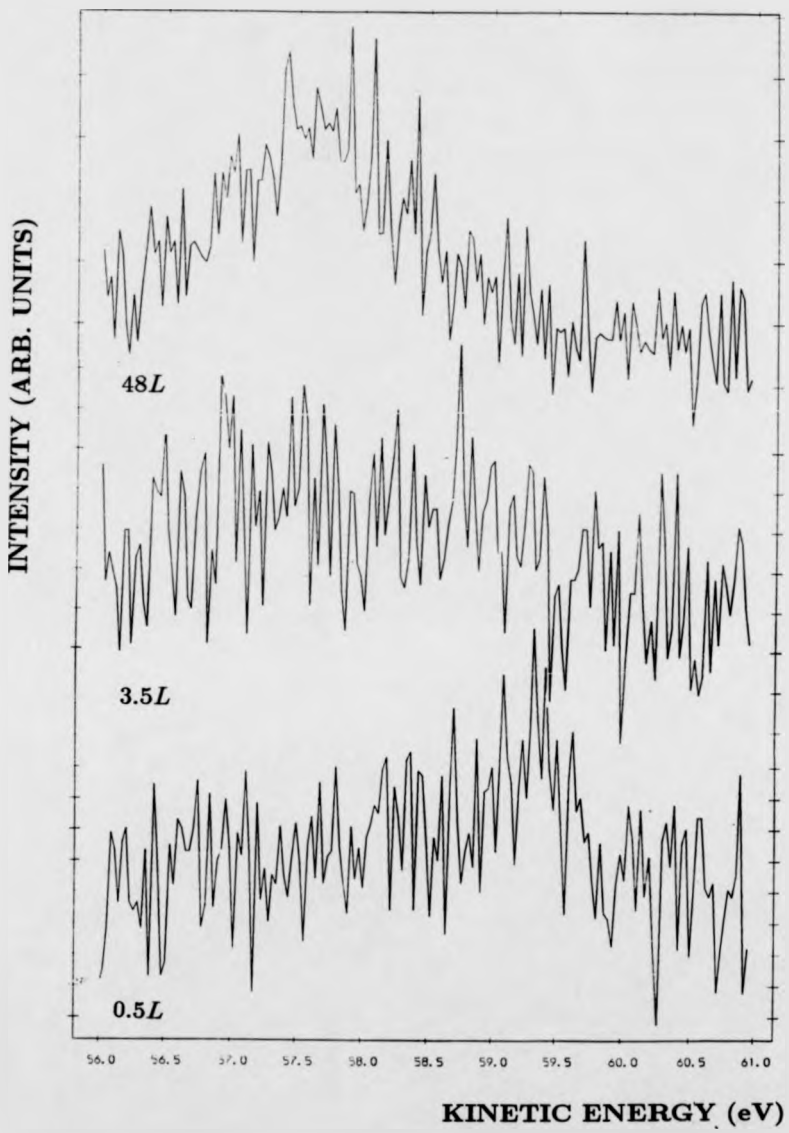

Fig 5.14 : Na 2p photoemission spectra from Al(111)+0.05MLNa +0.5, 3.5 and 48L oxygen

5.3.3.4 Na 2p photoemission from a thin Na film on Al(111) substrate following oxygen exposure

The Na 2p spectra shown in Fig(5.15) follow a Na pre-dose of 20 minutes exposure to the clean Al(111) substrate, and correspond to a thin Na film of approximately 10 to 20 layers. In comparison with the sub-monolayer Na pre-dosed spectra, there is no evidence for an oxygen chemisorption state of intermediate chemical shift; all that is observed are the metallic and oxide peaks. The broad oxide shifted state shows an enhancement of the total photoemission signal signifying that multilayer oxidation has occurred with an increase of the electron inelastic scattering mean-free-path [46]. The broad oxide shifted state is also shown to shift by a few tenths of eV prior to a final measured chemical shift of approximately 1.5eV. This chemical shift is significantly less than that seen in the sub-monolayer Na pre-dosed spectra of Fig(5.7) and Fig(5.12).

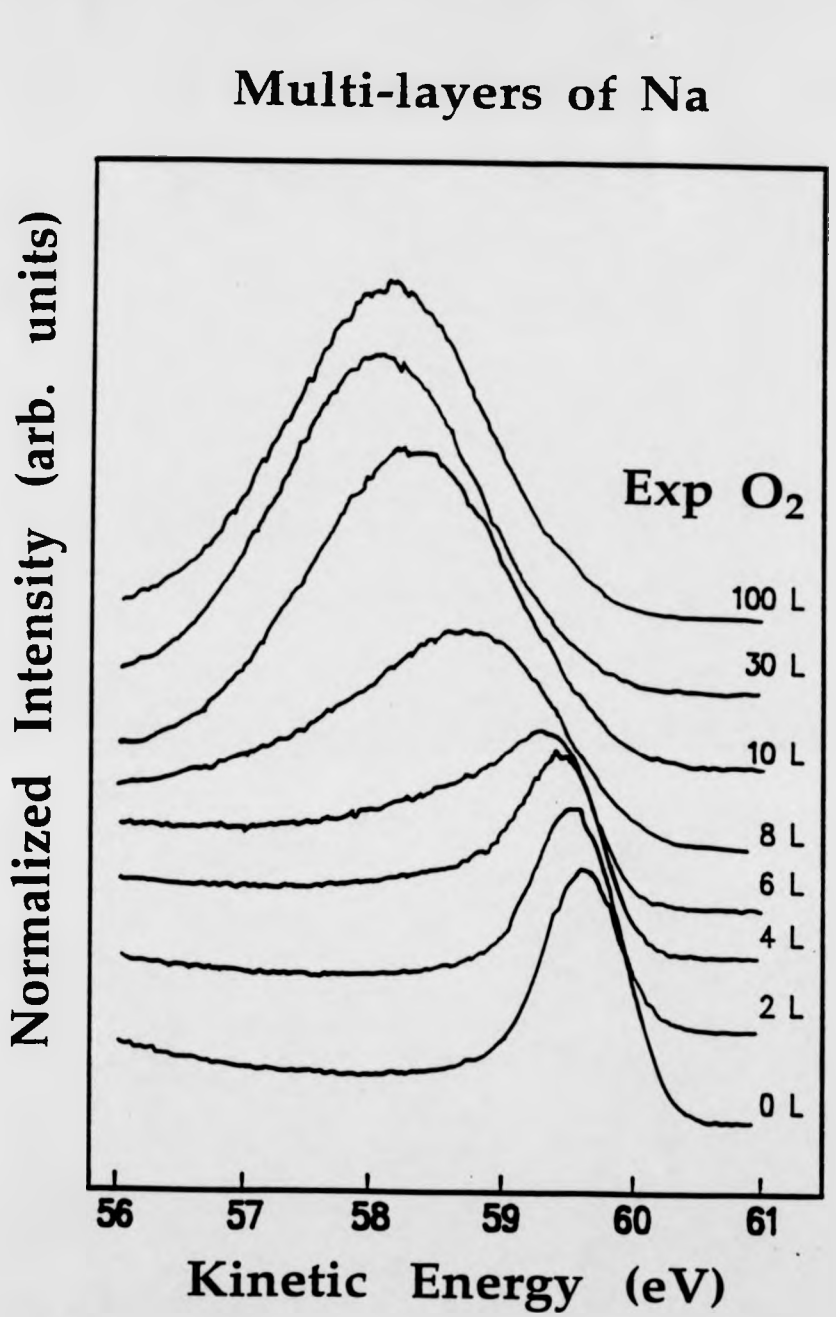

Fig 5.15 : Na 2p photoemission spectra from Al(111)+ multilayers Na with increasing oxygen exposure.

5.3.4 Discussion

The Al 2p and Na 2p photoemission results have cast light on two matters involved with the mechanisms behind the promoted oxidation of the Al(111) surface. Firstly, the oxygen dissociation mechanism is shown to be strongly promoted in the presence of sodium. The core level photoemission spectra however, only give information on the equilibrium state following the dissociation, and therefore do not give any direct information on the mechanism of promotion. Nevertheless, the spectra does provide information on the second issue, which is to understand the route to the formation of the three-dimensional oxide, and the question of the existence (and nature) of a chemisorbed precursor.

From the Na 2p photoemission spectra (Fig(5.7) and Fig(5.12)), there is clear evidence that an oxygen precursor does exist, but one in which the interaction of the oxygen is much stronger with the Na atoms than with the Al atoms. It is unfortunately not clear as to the precise distribution of the sodium atoms on the Al(111) surface at low coverages, so it is difficult to interpret accurately the results of experiments at these coverages. From Gurney's original picture of alkali adsorption [26], it is assumed that the dipole-dipole interaction between alkali atoms on the surface has a repulsion effect that would spread them out into an evenly spaced distribution. Recent evidence for Na clustering on Al(111) at low temperatures (100 K) [52] however, raises the question of whether similar clustering (or island formation) occurs at room temperature; which at present, no evidence exists. The local adsorption site for Na on Al(111) appears to differ for low temperatures and room temperature, with intermixing kinetically hindered at

100 K and Na atoms substituting top layer Al atoms (at low coverages) at room temperature. The effects of several possibilities can be considered in the absence of specific knowledge on Na atom distribution. If it is assumed that the Na atoms on the suface are able to form 2-dimensional islands of the $(\sqrt{3} \times \sqrt{3})R30^o$ phase at low coverages (contrary to the LEED pattern evidence seen), then the surface can be divided into a mixture of clean Al and ordered Na phase areas. Although this does not account for the increased rate of oxygen uptake of the Al intermediate chemically shifted states, it would account for the rate of production of the final oxide peak (Fig(5.11)). If these islands are formed, there could also be extra effects due to the island edges, which could take on a 'feeding' role of dissociated oxygen atoms onto the clean Al surface, possibly accounting for this increased uptake of the intermediate states.

If Gurney's model is correct, and there is an even Na atom distribution on the Al(111) surface, then the range of influence of the Na atoms needs to be clarified. If the promotional effect of the pre-dosed Na was non-local, then it would be related to the average potential change induced by the adsorbed Na, and hence may only show a significant effect at a critical coverage. Since there is a promotional effect at even the $\theta_{Na} \approx 0.05ML$ coverage, with an enhancement of the oxidation rate (at least initially) proportional to the Na coverage, a more local effect is more consistent with the data. The Na 2p data also support the picture that initial bonding of the oxygen atoms on the surface occurs at the Na sites, and if it is assumed that the appearance of the Al 2p oxide state is coupled to the Na 2p oxide chemically shifted state, then these Na sites are probably

also the nucleation centres for the true 3-dimensional oxidation of the Al(111) surface. The chemical shift of the Al 2p level on oxide formation is shown to be dependent on the progress of oxidation and whether the surface has been pre-dosed with sodium. In a similar experiment measuring the Al 2p photoemission peak following the interaction of water with the Al(111) surface, McConville *et al* observed no intermediate chemical shifts, but a final oxide shift of similar magnitude to that seen in this investigation [38].

In the Na 2p spectra following multilayer Na adsorption (Fig(5.15)), a smaller chemical shift for the final oxide was observed compared to the submonolayer coverages, suggesting that either the Na oxide state on the promoted surface (comprising a thin layer) is strongly coupled to the aluminium oxide, or that as has already been suggested, the oxide formed does involve both Al and Na atoms.

5.3.5 Conclusions

The influence of sodium (in the submonolayer range) on the oxidation of the Al(111) surface has been investigated using core level photoemission spectroscopy. The presence of sodium was found to greatly enhance the 3-dimensional oxide formation and increase the rate of oxygen dissociation.

The presence of sodium in the $(\sqrt{3} \times \sqrt{3})R30^o$ phase completely suppressed the Al 2p intermediate chemisorbed states seen on the clean surface as precursor states prior to final oxide formation. At the same time, the observation of a precursor state in the Na 2p spectra indicated that the initial chemisorption occurs strongly localised to the Na sites, with the accelerated oxidation being a

direct consequence of the enhanced filling of this precursor state by the increased oxygen dissociation rate. Some evidence is also shown that the final state is an intermixed Al and Na oxide.

References

[1] K.H.Kingdon and I.Langmuir, Phys. Rev. **21**, p380 (1923)

[2] J.B.Taylor and I.Langmuir, Phys. Rev. **44**, p423 (1933)

[3] D.S.Villars and I.Langmuir, J. Am. Chem. Soc. **53**. p486 (1931)

[4] H.P.Bonzel and H.J.Krebs, Surf. Sci. **117**, p639 (1982)

[5] P.H.Emmett, in *The Physical Basis for Heterogenous Catalysis* Eds. E.Drauglis and R.I.Jafree (Plenum, New York. 1975)

[6] H.P.Bonzel, Surf. Sci. Reports **8**, p43 (1987)

[7] J.Kirschner, in *Polarized Electrons in Surface Physics* Ed. R.Feder (World Scientific, Singapore. 1985)

[8] J.Stöhr, L.I.Johansson, S.Brennan, M.Hecht and J.N.Miller, Phys. Rev. **B22**(8), p4052 (1980)

[9] W.Eberhardt and C.Kunz, Surf. Sci. **75**, p709 (1978)

[10] M.Lannoo and P.Friedel, *Atomic and Electronic Structures of Surfaces* Ed. M.Cardona (Springer-Verlag, Berlin. 1991)

[11] H.Hertz. Ann. Physik **31**, p983 (1887)

[12] A.Einstein. Ann. Physik **17**, p132 (1905)

[13] *Photoemission and the Electronic Properties of Surfaces* ed. Feuerbacher, Fritton and Willis. (Wiley, 1978)

[14] D.P.Woodruff and T.A.Delchar, *Modern techniques of surface science* (Cambridge University Press, Cambridge. 1986)

[15] *Handbook of X-Ray and Ultraviolet Photoelectron Spectroscopy* ed. D.Briggs. (Heyden and Son Ltd. 1977)

[16] C.S.Fadley, in *Electron Spectroscopy: Theory, Techniques and Applications* ed. C.R.Brundle and A.D.Baker (Academic Press, London. 1978) Vol.2

[17] W.F.Egelhoff, Jr. Surf. Sci. Reports **6**, p253 (1987)

[18] D.A.Shirley. Advanc. Chem. Phys. **23**, p85 (1973)

[19] N.W.Ashcroft and N.D.Mermin *Solid State Physics*, (Saunders College Publishing, 1976)

[20] *Topics in Applied Physics, Vol 26: Photoemission in Solids 1* ed. M.Cardona and L.Ley (Springer-Verlag, 1978)

[21] T.A.Koopmans. Physica **1**, p104 (1933)

[22] A.Rosen and I.Lindgren, Phys. Rev. **176**, p114 (1968)

[23] M.A.Brisk and A.D.Baker. J. Elect. Spect. **7**, p197 (1975)

[24] *Practical Surface Analysis* ed. D.Briggs. (John Wiley and Sons, 1983)

[25] A.R.Williams and N.D.Lang. Phys. Rev. Lett. **40**, p954 (1978)

[26] R.W.Gurney, Phys. Rev. **47**, p479 (1935)

[27] G.A.Benesh and J.R.Hester, Surf. Sci. **194**, p567 (1988)

[28] N.D.Lang and A.P.Williams, Phys. Rev. **B18**, p616 (1978)

[29] J.P.Muscat and D.M.Newns, Surf. Sci. **74**, p355 (1978); **84**, p262 (1979)

[30] J.P.Muscat and I.P.Batra, Phys. Rev. **B34**, p2889 (1986)

[31] P.A.Serena, J.M.Soler, N.Garcia, and I.P.Batra, Phys. Rev. **B36**, p3452 (1987)

[32] B.N.J.Persson and L.H.Dubois, Phys. Rev. **B39**, p8220 (1989)

[33] K.Y.Yu, J.N.Miller, P.Chye, W.E.Spicer, N.D.Lang and A.R.Williams, Phys. Rev. **B14**, p1446 (1976)

[34] S.A.Flodstrōm, R.Z.Bachrach, R.S.Bauer, S.B.M.Hagstrōm, in Proc. 7th Intern. Vac. Congress, Vienna, (1977) p461, p869.

[35] S.A.Flodstrōm, C.W.B.Martinsson, R.Z.Bachrach, S.B.M.Hagström and R.S.Bauer, Phys. Rev. Letts. **40**(13), p907 (1978)

[36] F.Soria, V.Martínez, M.C.Muñoz and J.L.Sacedón, Phys. Rev. **B24**(12), p6926 (1981)

[37] W.Eberhardt and F.J.Himpsel, Phys. Rev. Letts. **42**, p1375 (1979)

[38] C.F.McConville, D.L.Seymour, D.P.Woodruff and S.Bao, Surf. Sci. **188**. p1 (1987)

[39] P.S.Bagus, C.R.Brundle, F.Illas, F.Parmigiani and G.Polzonetti, Phys. Rev. **B44**, p9025 (1991)

[40] J.Winterlin, H.Brune, H.Höfer and R.J.Behm, Appl. Phys. **A47**, p99 (1988)

[41] N.A.Braaten, J.K.Grepstad, S.Raaen and S.L.Qiu, Surf. Sci. **250**, p51 (1991)

[42] K.Horn, A.Hohlfield, J.Somers, Th.Lindner, P.Hollins and A.M.Bradshaw, Phys. Rev. Letts. **61**, p2488 (1988)

[43] K.-H.Frank, H.-J.Sagner and D.Heskett, Phys. Rev. **B40**(5), p2767 (1989)

[44] D.Heskett, K.-H.Frank, E.-E.Koch and H.-J.Freund, Phys. Rev. **B36**, p1276 (1987)

[45] H.Ishida and K.Terakura, Phys. Rev. **B38**, p5752 (1988)

[46] D.Norman and D.P.Woodruff, J. Vac. Sci. Technol. **15**(4), p1580 (1978)

[47] J.N.Anderson, M.Qvarford, R.Nyholm, J.-F.Van Acker and E.Lundgren, Phys. Rev. Letts. **68**, p94 (1992)

[48] M.Kerkar, D.Fisher, D.P.Woodruff, R.G.Jones, R.D.Diehl and B.Cowie, Surf. Sci. **278**, p246 (1992)

[49] A.Schmalz, S.Aminpirooz, L.Becker, J.Haase, J.Neugebauer, M.Scheffler, D.R.Batchelor, D.L.Adams and E.Bogh, Phys. Rev. Letts. **67**, p2163 (1991)

[50] M.Kerkar, D.Fisher, D.P.Woodruff, R.G.Jones, R.D.Diehl and B.Cowie, Phys. Rev. Letts. **68**(21), p3204 (1992)

[51] C.F.McConville, A.B.Hayden, J.Robinson and D.P.Woodruff, to be published.

[52] J.N.Anderson, E.Lundgren, R.Nyholm and M.Qvarford, Surf. Sci. in press.

Chapter 6

Normal incidence standing X-ray wave (NISXW) study of Methoxy on Al(111)

Contents

6 Normal incidence standing X-ray wave (NISXW) study of Methoxy on Al(111) 192

6.1 Introduction 194

6.2 Theory 197

6.2.1 Variation of incidence angle 198

6.2.2 Energy variation 200

6.3 NISXW analysis 200

6.3.1 Method of Triangulation 205

6.4 NISXW Study of Methoxy on Al(111) 207

6.4.1 Introduction 207

6.4.2 Experimental considerations 208

6.4.3 Experimental results 210

6.4.4 Oxygen atom location by triangulation 219

6.4.5 Discussion 222

6.4.6 Conclusions 227

6.1 Introduction

When X-rays are Bragg reflected from a series of lattice planes inside a crystal, the incident and reflected waves may interfere to produce standing waves. In the first experiments by Batterman in 1964, the standing waves were created by X-rays at grazing angle on highly perfect silicon crystals [1, 2]. A standing wave requires a reflected amplitude of equal magnitude to the incident wave, so the Bragg reflection has to be built up over many lattice planes thereby placing the experimental emphasis on using highly ordered crystals. An important effect of the Bragg condition, is that the Bragg planes of the crystal responsible for the diffraction are related to the standing wave in the sense that the nodal planes of the wave have the same periodicity as the plane spacing, and also lie parallel to them [3, 4]. When the Bragg condition is traversed from the low angle to the high angle side (at grazing incidence, the angular width or rocking curve of the Bragg condition is typically less than 10 secs of arc.), the phase of the standing wave shifts by $\pi/2$. This has the effect of moving the nodes and antinodes of the wavefield progressively by half the Bragg plane spacing. The X-ray absorption of the atoms in the scattering planes varies as the Bragg condition is traversed, so by monitoring the absorption (through Auger or photoemission measurements), a distinct absorption profile is obtained. Since the standing wavefield generated extends far from the crystal surface, the position of an adsorbed atom at the surface can be then located by measuring the X-ray absorption of the adsorbed atom as the wavefield is shifted; the shape of the adsorbate absorption profile changing for different scattering plane to adsorbate distances.

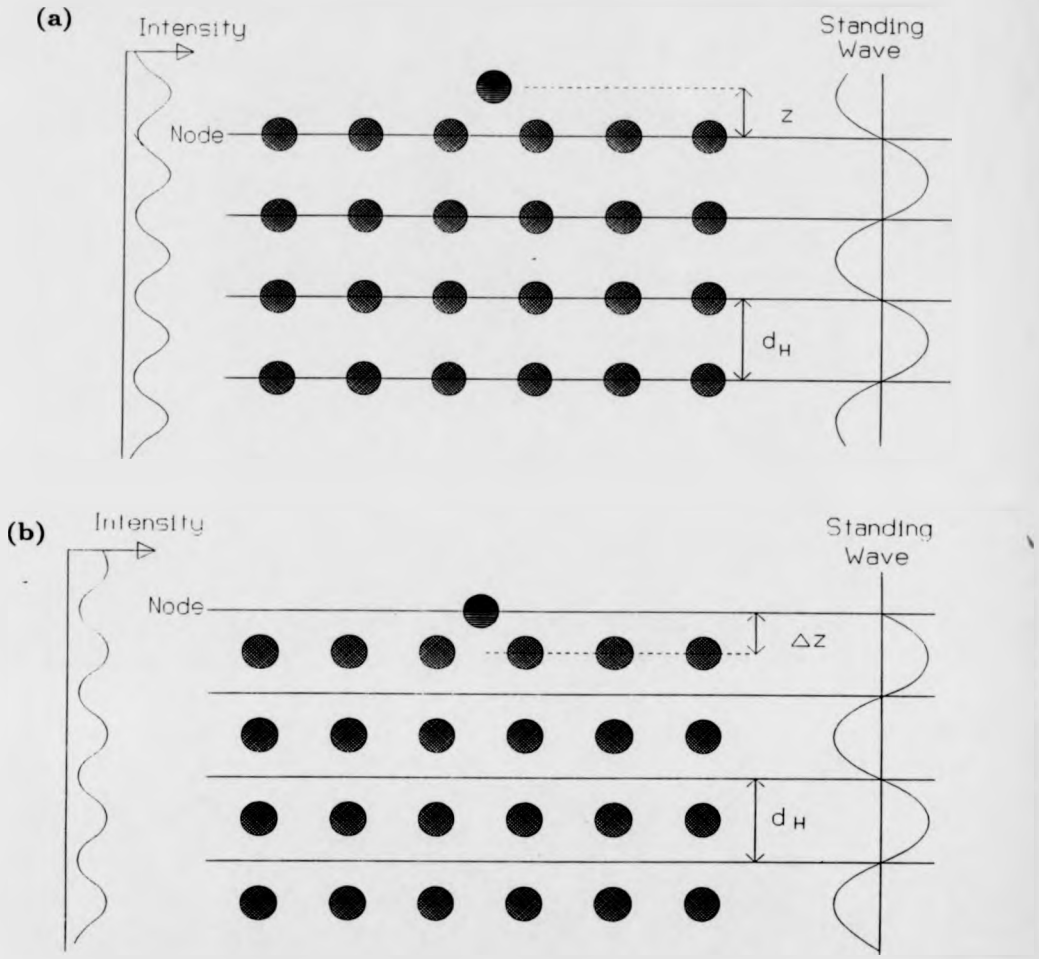

Fig(6.1) : Schematic of the NISXW process, showing the Bragg planes (seperation d_H) and the adsorbate atom position (located Δz) above the surface. **(a)** shows the nodal plane of the standing wave at the Bragg planes, and **(b)** shows the situation after the Bragg condition is swept (the nodal plane moving by half a lattice spacing).

Fig(6.1) is a schematic of the standing X-ray wave process for normal incidence, Fig(6.1a) showing the standing X-ray wavefield with the node (region of zero intensity) situated at the scattering planes (separation d_H) with the absorber atom a distance Δz from the surface, and Fig(6.1b) shows the wavefield after energetically sweeping through the Bragg condition. In the early experiments, the technique was used to determine the relative position of impurity atoms to the atomic planes in semiconductors, by monitoring the X-ray fluorescence from impurity atoms as a function of Bragg angle [2, 5]. These experiments were limited to grazing incidence studies due to the laboratory X-ray source energy used, and the small angular range of the resultant rocking curve placed great emphasis on highly accurate goniometers. By conducting the experiment in ultra high vacuum (UHV) conditions, the studies were extended to adsorbates (such as bromine) on semiconductor surfaces [6, 7], and soon after (in 1985) the first SXW expriments using synchrotron radiation were achieved. The first few of these studies used grazing variable incidence angle SXW on semiconductor materials [8, 9, 10]; following advances in monochromator design, the Bragg condition could be swept in energy which removed the problems associated with using accurate sample mounted goniometers in UHV conditions [11, 12, 13, 14].

The observation of standing wave effects in experiments designed for surface extended X-ray absorption fine structure (SEXAFS) in near normal incidence measurements was remarked upon by Ohta *et al* in the early to mid 80's [15, 16], recognising their origin and potential for structural investigations. What was apparently not recognised however, was the insensitivity to crystal perfection and

beam collimation that occurs at normal incidence Bragg reflection, which allows a much greater range of applicability. This advantage was first successfully utilised by Woodruff *et al* in an investigation of a Cl adsorption phase on a non-perfect Cu(111) crystal [17, 18].

In this chapter, the general theory of NISXW and the technique of analysing NISXW data is described. Section(6.4) presents results from a NISXW study of methoxy on Al(111) conducted on beamline 6 (station 6.3) at the Daresbury synchrotron radiation source.

6.2 Theory

The theory of the standing X-ray wave (SXW) technique is well documented [1, 5, 7, 8, 9, 18, 19], being similar for both energy and angle scans through the Bragg condition.

The SXW equations can be derived by solving Maxwell's equations for the case of a periodic dielectric constant [20], which defines a region in the spectrum of travelling wave solutions to these equations in which only standing wave solutions are possible (this corresponding to the Bragg region)[11].

The basic equation defining the intensity of this standing wave field is

$$I = \mid 1 + (E_H/E_O)\exp(-2\pi i \boldsymbol{H}\cdot\boldsymbol{r}) \mid^2 \qquad (6.1)$$

(E_H/E_O) being the amplitude of the electromagnetic field, **H** is the reciprocal lattice vector associated with the Bragg reflection and **r** is the vector defining the relative position of the absorber (adsorbed atom) from the Bragg planes.

If Δz defines the perpendicular distance of the absorber atoms from the scattering planes which have a separation d_H, then the scaler product of equation(6.1) can be substituted by $\Delta z/d_H$.

The amplitude of the electromagnetic field is defined in terms of the geometrical structure factors (F_H and $F_{\bar{H}}$) for the corresponding H and $\bar{H}$ reflections [18].

$$E_H/E_O = -(F_H/F_{\bar{H}})^{1/2}[\eta \pm (\eta^2 - 1)^{1/2}] \tag{6.2}$$

η is the displacement parameter, and is associated with the angle of incidence or energy of the incident X-ray beam that is varied in order to scan through the Bragg condition.

6.2.1 Variation of incidence angle

If the angle of incidence is varied by an amount $\Delta\theta$ centered on the Bragg angle θ_B, then the displacement parameter in equation(6.2) is defined by:

$$\eta = \frac{(\Delta\theta \sin(2\theta_B) + \Gamma F_0)}{\mid P \mid \Gamma(F_H F_{\bar{H}})^{1/2}} \tag{6.3}$$

where F_0 is the structure factor for the (000) reflection, and P is fixed by the polarisation of the X-rays ($P = 1$ for σ polarisation and $P = \cos(2\theta_B)$ for π polarisation) The quantity Γ is dependant on the X-ray wavelength λ and the volume of the unit cell V, and is given by

$$\Gamma = \frac{(e^2/4\pi\epsilon_o mc^2)\lambda^2}{\pi V} \tag{6.4}$$

where ϵ_o is the permittivity of free space; e and m are the charge and mass of an electron and c is the velocity of light.

For the case of X-rays of σ polarisation ($P = 1$) that are Bragg reflected off a perfect crystal with no absorption, the region of total reflectivity is defined from equation(6.2) by the range $-1 < \eta < +1$. The range is not centered on θ_B, but is in actual fact offset by the term ΓF_o (corresponding to an angle of $\Gamma F_o / \sin(2\theta_B)$ The range of total reflectivity is then

$$\Delta\theta_{Tot} = \pm \left[\frac{\mid P \mid \Gamma (F_H F_{\bar{H}})^{1/2}}{\sin(2\theta_B)} \right] \tag{6.5}$$

This angular range is relative to the offset angle, and is typically only a few secs. of arc at grazing incidence Bragg angles [5], hence the necessity of using perfect crystals and the difficulties in using accurate goniometers in UHV conditions for this geometry.

If the incidence angle is close to normal incidence, then a different problem is encountered. From equation(6.5), it can be seen that the $\sin(2\theta_B)$ term decreases and the total reflectivity range increases as normal incidence is approached, until finally when normal incidence is reached, the $\sin(2\theta_B)$ term equals zero. The actual region of reflectivity (or rocking curve) is more complex in the close proximity of θ_B, since the displacement parameter is no longer linear in $\Delta\theta$ and two Bragg conditions (on either side of 90°) converge on each other [18, 21]. Graeff and Materlik showed that the shape of the rocking curve close to normal incidence could be determined using the dynamical theory of X-ray scattering (the rocking curve being approximately 1 deg. arc) [21].

6.2.2 Energy variation

If the Bragg condition is swept energetically (using synchrotron radiation to tune the X-ray wavelength to match the Bragg plane spacing), then the displacement parameter η becomes

$$\eta = \frac{[-2(\triangle E/E)\sin^2\theta_B + \Gamma F_o]}{\mid P \mid \Gamma(F_H F_{\bar{H}})^{1/2}} \tag{6.6}$$

As opposed to the variable angle case, η remains linear in $\triangle E$ even at $\theta_B = 90°$, but still shares an offset in the centre of the total reflectivity range from the nominal Bragg Energy [18], in this case by $\Gamma F_o E/(2\sin^2\theta_B)$, the energy range of the reflectivity region given in equation(6.7).

$$\triangle E = \pm\frac{E \mid P \mid \Gamma(F_H F_{\bar{H}})^{1/2}}{2\sin^2\theta_B} \tag{6.7}$$

The energy width (typically $\sim 1eV$, although for higher energy reflections it can be much less than this) produces an energy resolution ($\triangle E/E = 3 \times 10^{-4}$) which is similar to the double crystal monochromators used on synchrotron beam lines designed for Extended X-ray Absorption Fine Structure (EXAFS) experiments (see chapter(2)).

6.3 NISXW analysis

If the absorption of the absorber atom is monitored through the 'rocking' curve associated with the Bragg condition (through X-ray flourescence, Auger emission etc.), then the emitted signal would rise or fall dependent on the atoms position

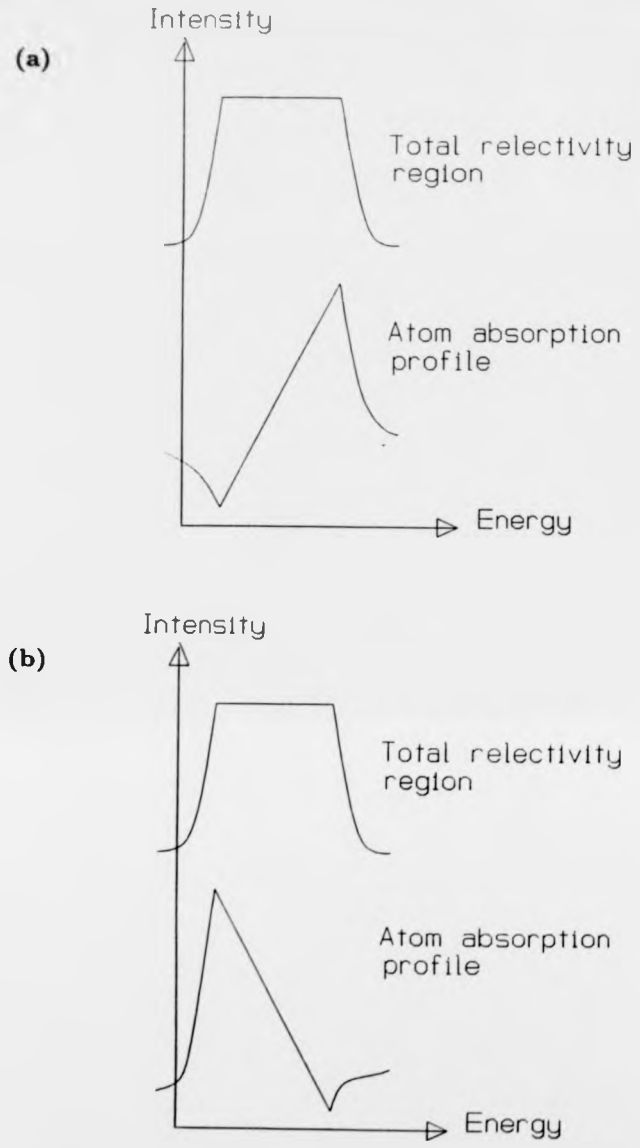

Fig(6.2) : (a) shows the absorption profile expected for an adsorbate located either in the lattice plane, or at a distance of a lattice spacing above the surface. The total reflectivity region shows the width of the Bragg condition. (b) shows the absorption profile expected if the adsorbate is located half a lattice spacing from the surface.

-with respect to the standing wave nodes and antinodes. Fig(6.2a) shows the signal expected if the absorber atom is located in the atomic scattering plane, against the reflectivity curve (Darwin-Prins curve) associated with the Bragg condition. The tails on either side of the Bragg condition are associated with the loss of the standing wave and a return to the general x-ray absorption background. If the absorber atom were to be located at a distance from the surface corresponding to half the lattice spacing, then the absorption curve for the atom would be as shown in Fig(6.2b). For each position of the absorber atom from the scattering planes, there is a particular absorption profile. Therefore, if the profile can be theoretically modelled and compared with the measured profile to obtain a match, the distance of the atom from the scattering planes can be determined. In order to model the profiles, a FORTRAN program written by D.P.Woodruff has been used. Fig(6.3) shows the absorption profiles for several adatom positions for the geometry corresponding to normal incidence Bragg reflection from Al(111) planes, obtained using this program. The analysis technique of the NISXW data can be divided into four main parts: normalisation, background subtraction, substrate profile fitting and adsorbate profile fitting.

Since there can be slight drifts in the energy calibration of the monochromator and in the intensity of incident radiation, normalisation of the data is necessary. Although the energy drift is typically less than one eV, the analysis procedures are dependent on the accurate measurement of energy differences between the experimental peaks, in order to obtain an accurate layer spacing. Since the energy differences of interest are of the same order as the monochromator drift, the need

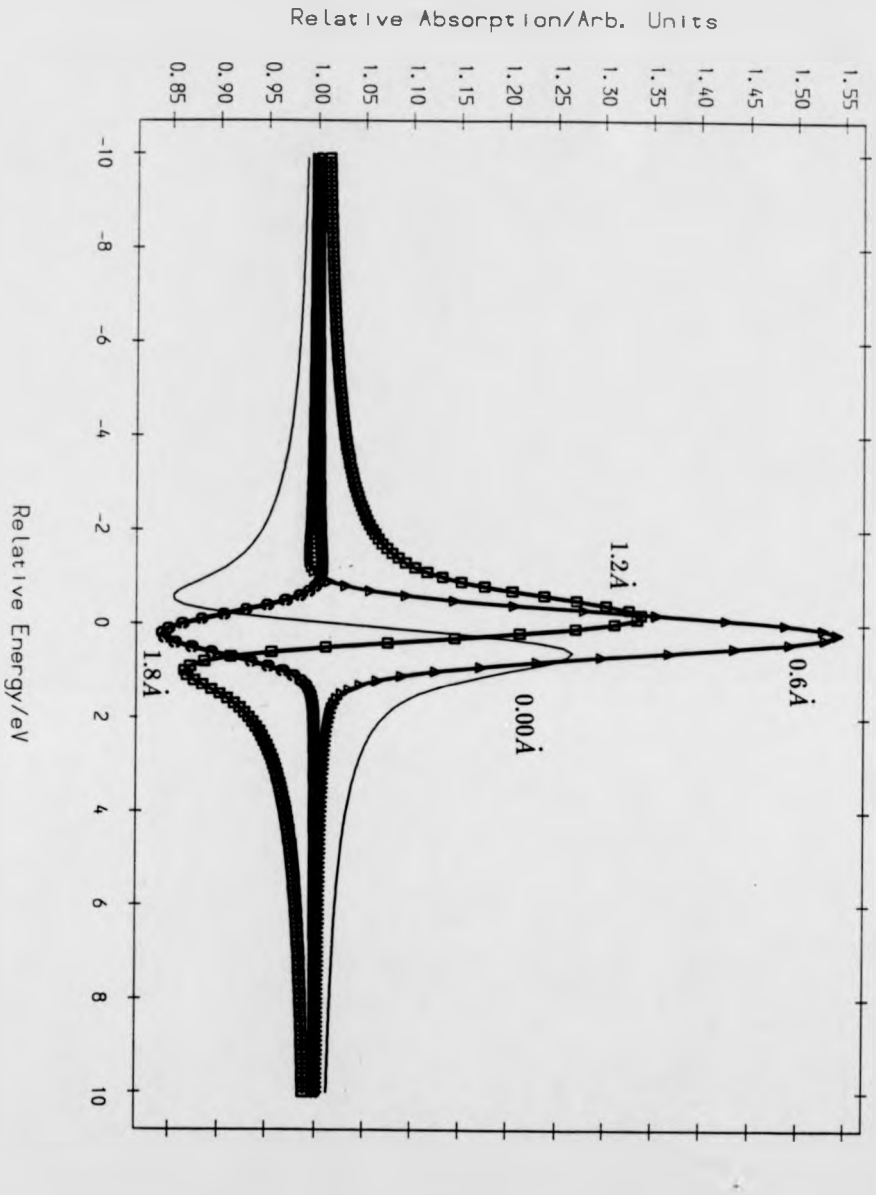

Fig(6.3) : Showing the calculated absorption profiles for adsorbate atoms located at various Δz distances from the surface. The profiles are calculated using the Al(111) Bragg plane spacing.

-for good calibration is paramount. To this end, the total electron yield signal from the crystal during the experiment is measured (either by monitoring the crystal current or the current arriving at the 'spoon' detector) for all scans. It is assumed that the line shape of the total yield signal is constant for all scans, so the energy of the peak in the total yield was used as a reference to normalise the energy of all measurements (total yield and the simultaneous Auger signal scans).

Following energy calibration of the spectra, a background must be subtracted. To achieve this, electron emission signals also measured at 50 eV above the Auger or core level photoemission peaks were monitored from both substrate and adsorbate species. These background signal spectra were then simply subtracted from spectra recorded 'on' the auger or photoemission peaks. In the case of a peak superimposed on a sloping background, the subtraction involved an appropriate scaling factor.

Structure determination then proceeded by modeling the absorption profiles using different structural parameters, but it is also necessary to add the effects of disorder to the standing wave intensity equation(6.1) to simulate the experiment. Firstly, the vibration of the substrate atoms (which have an effect of reducing the standing wave field by decreasing the amplitude of the reflectivity) is accounted for by multipying F_H (the geometrical structure factor) by a Debye Waller factor ($\exp(-M)$). In a similar way the vibration of the absorbers also acts to reduce the apparent coherent fraction by $\exp(-M)$ (strictly the two M values for the adsorbate and substrate may differ). Including these parameters, equation(6.1)

becomes

$$I = \mid 1 + f_{co}(E_H/E_O)\exp^{(-2\pi i\Delta z/d_H)} \mid^2 + (1 - f_{co}^2) \mid E_H/E_O \mid^2 \qquad (6.8)$$

where the apparent coherent fraction f_{co} is a product of the true (static disorder) value and the absorber and scatterer Debye-Waller factors.

The substrate profiles are modelled first in order to fix the main instrumental parameters, making the assumption that $\Delta z = 0.0\mathring{A}$. As the signal is collected over greater than six atomic layers and only the top one or two layers can be expected to experience any layer spacing change from their normal bulk values, this is thought a good assumption.

The coherent fraction and Debye-Waller factor, and the energy broadening of the monochromator output (assumed to be Gaussian) are then varied to match the modelled profile to the experimental profile.

Following the fitting of the substrate absorption profiles, the non-structural parameters are then fixed and the modelling of the absorption profile of the adsorbed atom can be attempted. This is then done by varying the Δz parameter and the adsorbate coherent fraction to provide a match to the experimental profile.

6.3.1 Method of Triangulation

In order to determine the actual location of the adsorbed atom on the surface, the experiment needs to be repeated using a second set of scattering planes that are at an angle to the initial set. Fig(6.4) shows a schematic of the triangulation principle. When the distance of the adsorbed atom from each set of Bragg planes

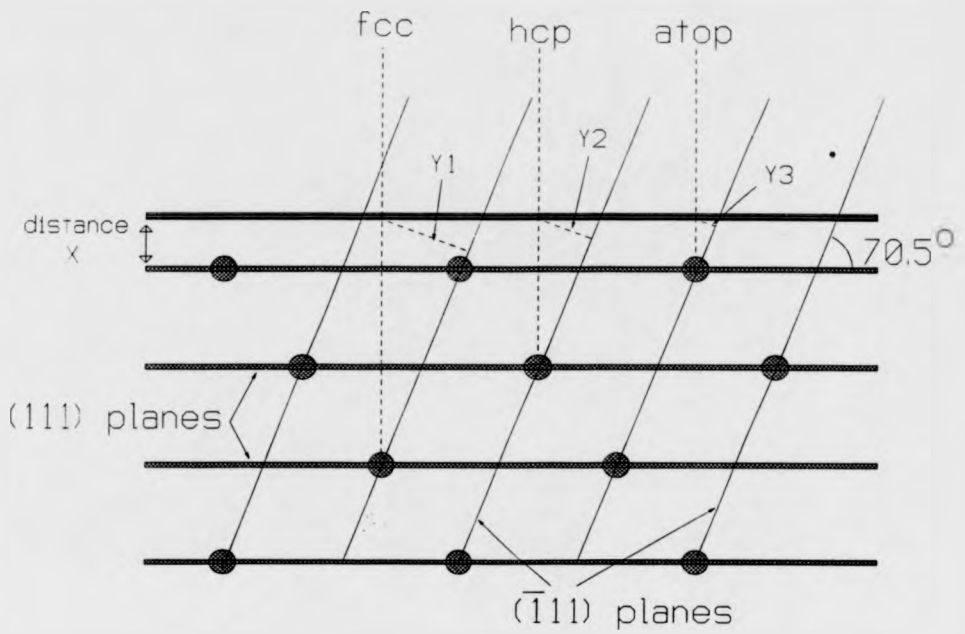

Fig(6.4) : Schematic of the triangulation technique. The distances **X** and **Y** of the adsorbate atom from the (111) and ($\bar{1}$11) Bragg scattering planes are determined from NISXW measurements. In this model, three likely adsorbate sites are modelled on the (111) surface with the adatom at a distance **X** above the surface plane. The distance of each of these possible sites to the ($\bar{1}$11) plane are then calculated (i.e **Y1, Y2** and **Y3**) and compared with the experimentally determined **Y** value to deduce the actual adsorption site.

-has been determined, then the actual location can be calculated by triangulation [7, 22, 23]. Modelling of the possible sites can then be attempted in order to determine the most likely bonding site for the absorbed atom on the surface.

6.4 NISXW Study of Methoxy on Al(111)

6.4.1 Introduction

In the experiment reported here, the local adsorption structure of the O atom in methoxy (CH_3O) adsorbed on Al(111) has been determined using NISXW triangulation using the Al(111) and ($\bar{1}11$) Bragg reflections.

Methanol, the smallest member of the alcohol organic compounds, has great importance in many industrial applications; being a building block ('feedstock') for some important synthetic reactions, as well as being used as a fuel, or mixed with petrol to improve engine performance [24].

CH_3O (methoxy) is a catalytic intermediate formed by the deprotonation of methanol at many metal surfaces. The majority of studies have been on the Ag and Cu surfaces, zinc oxide/copper catalysts being used in the industrial production of Methanol [25]. The formation of methoxy on aluminium surfaces as a result of methanol decomposition has been inferred from several electron spectroscopic and desorption studies over polycrystalline surfaces [24, 26, 27], and more importantly it has been identified on Al(110)[28] and Al(111)[29] using vibrational spectroscopy.

CH_3OH is molecularly found to be intact on Al(111) at 90 K [29]. On heating

to 143 K the OH bond is broken and the methoxy surface species is formed, with methoxy bonding to the Al surface through the O atom (mainly by the donor contribution of the oxygen lone pair electrons). When the methoxy species is absorbed on the Al(111) surface, there is an absence of any other oxygen containing product (such as CO and CO_2) on the $CH_3O/Al(111)$ layer. Further heating to 700 K leads to the removal of the methoxy species from the surface leaving C and O on Al [29].

The mechanisms of heterogenous catalysis can be better understood if information (such as position of the molecular species on the surface to determine 'active' sites) can be obtained from these intermediates. hence the aim of this investigation is to understand the bonding geometry of the methoxy species to the Al(111) surface and compare with recent NISXW investigations of the bonding of oxygen to the Al(111) surface [30]. These results are discussed and compared with information from similar systems.

6.4.2 Experimental considerations

Prior to the experiment, the mode of detecting the absorption profiles for both substrate and adsorbate (i.e Al and O) needed to be decided. The question of whether to monitor the X-ray fluorescence, total yield, Auger signal or a core level photoemission signal is very dependent on the substrate and adsorbate used. X-ray fluorescence has been used in many previous SXW studies, mainly those using grazing incidence geometry conducted in air using hard X-rays. This method has been found to have high sensitivity to low concentrations, making it suitable

for investigation of impurity atoms in semiconductors [6]. The total electron yield (obtained by measuring the sample current or total photoemission current), monitors all the photoionisation events that occur due to the standing wave. This signal includes contributions from many atomic layers, and is therefore dominated by the substrate. The total yield signal is not, however, used to monitor the substrate absorption profile, since after comparing this signal with the Auger signal from the substrate (measured simultaneously), Woodruff *et al* found that the two profiles were slightly different [18]. This difference has been attributed to the large concentration of low energy secondary electrons (sampling a much greater depth) in the total yield signal; at greater depth, substantial distortion of the SXW profile occurs due to absorption.

The two energy selective modes of Auger electron and core level photoemission signals are also considered. The photoemission signal has been found to suffer from the competing process of photoelectron diffraction in SEXAFS studies [19], making this channel generally inappropriate for monitoring the adsorbate absorption at low kinetic energies (e.g below $\approx 500eV$ or even higher). Since in this experiment however, aluminium has few (widely spaced) core levels and the Bragg energy for the Al(111) planes is sufficiently high (2660 eV), that the O 1s photoelectron peak occurs at a kinetic energy for which the Al photoemission background signal is low and at which photoelectron diffraction is unimportant. Of course, a special problem for light elements is that in SXW the Bragg condition scans at an energy which is high relative to the adsorbate core level binding energy, leading to poor photo absorption cross sections. For Al(111) the Bragg

energy for this purpose is rather low; the lack of many substrate core levels therefore leads to a signal-to-noise ratio which is much greater than found in other light adsorption systems.

The other energy selective mode of detection, that of monitoring the Auger electron signal, is used to measure the substrate absorption profile in this experiment (the Al KLL auger peak measured at 1390eV kinetic energy). The question of whether surface reconstruction/relaxation effects distort the SXW profile relative to the true bulk absorption profile is of concern when using this surface sensitive signal. However, the Al(111) surface, in common with fcc metal surfaces in general, does not normally show any major layer spacing changes at the surface, and the surface layer contribution to the Auger signal is estimated to be only approximately 16%. The oxygen KLL Auger peak (510eV) lies on the inelastically scattered electron background from the Al 1s photoemission peak and offers a worse signal-to-noise ratio than that of the O 1s signal, which, as previously discussed, was used as the monitor of O absorption [31].

6.4.3 Experimental results

A general description of the synchrotron radiation beamline has been given in chapter(2).

The Al(111) crystal was prepared as described in chapter(5), with final cleaning *in situ* by argon ion bombardment and annealing cycles. The clean ordered surface was characterised by Auger electron spectrosopy (AES) and LEED, with the surface methoxy species being formed by cooling the clean Al crystal to 150

K, and exposing to 15L of methanol. The NISXW experiment was conducted with the sample held at 150 K, and also at room temperature (allowing the Al crystal to warm up after forming the methoxy species at 150 K). For both temperatures, the NISXW measurements were obtained from the Al(111) and ($\bar{1}11$) Bragg planes (the latter being at 70.53° to the (111) planes).

The parameters used to fit the aluminium substrate absorption profiles for the (111) and ($\bar{1}11$) reflections are summarised in table(6.1), and apply to both low temperature and room temperature measurements.

Fitting Parameter	**(111) Value**	**($\bar{1}11$) Value**
Debye-Waller factor	0.9	0.9
Coherent fraction	0.9	0.9
Gaussian width	0.7eV	0.7eV
Δz	0.00Å	0.00Å

Table 6.1:*Fitting parameters for Al substrate absorption profiles from NISXW measurements for (111) and ($\bar{1}11$) Bragg scattering conditions.*

6.4.3.1 Low temperature NISXW results (150 K)

Adsorbed methanol on Al(111) has been reported to dissociate to form the adsorbed methoxy with desorption of molecular hydrogen at 143 K [29]; the Auger electron spectra taken in our experiments following exposure to methanol at 150

K showed oxygen and carbon signals at an intensity in agreement with the stochiometry for methoxy on Al(111). Several spectra were taken, monitoring the total yield signal and the Al KLL Auger peak signal, whilst slight adjustments were made to the crystal position to optimise the standing wave absorption profile in the substrate. The measurements of the absorption profiles for both Al and O were made both at the appropriate peak electron kinetic energy, and at an energy 50 eV above to provide a subtractable background. Following NISXW measurements, Auger electron spectra were taken to check that the methoxy had not undergone any significant photodesorption during the experiment, and also to check the surface for other contaminants. No attenuation of the O and C Auger signals was observed, and the surface also remained free of other contamination.

Fitting Parameter	**(111) Value**	**($\bar{1}$11) Value**
Debye-Waller factor	0.9	0.9
Coherent fraction	0.9	0.9
Gaussian width	0.7eV	0.7eV
Δz	0.70Å	0.95Å

Table 6.2: *Fitting parameters for the O absorption profiles from NISXW measurements of methoxy on Al(111) at $T = 150K$ for both (111) and ($\bar{1}$11) Bragg scattering conditions.*

The parameters used to fit the measured oxygen absorption profile for both

(111) and ($\bar{1}11$) normal incidence Bragg scattering conditions are shown in Table(6.2). The analysed NISXW profiles due to NISXW from the Al(111) Bragg planes are shown in Fig(6.5). The absorption profile obtained from monitoring the Al KLL Auger peak is the low noise single line joining data points, with the theoretical fit displayed as a dash-dot line. The measured absorption profile obtained from the O 1s photoemission signal is shown in the same figure, depicted by the single line with greater noise levels than the Al absorption. The theoretical fit to this profile is shown as a continuous line between data points represented by empty squares. The determined random error in Δz from experimental and fitting techniques was $\pm 0.10\mathring{A}$.

The Al(111) crystal was then rotated by approximately 70.5°, so that the ($\bar{1}11$) planes were normal to the incident radiation. The same adjustments were undertaken to the crystal position using the substrate standing wave absorption profile to monitor the optimisation of the angle of incidence as close as possible to normal to the reflecting planes. The experiment was then repeated with the Al($\bar{1}11$) Bragg planes.

The experimental absorption profiles and the theoretical fits are shown in Fig(6.6). The figure uses the same line types as for Fig(6.5), with the exception of the theoretical O 1s photoelectron absorption profile which has data points depicted by empty circles. The parameters used to fit the Al KLL Auger profile are unchanged from the Al(111) fit. The theoretical fit to the O 1s photoelectron signal absorption profile was obtained with the parameters shown in Table(6.2).

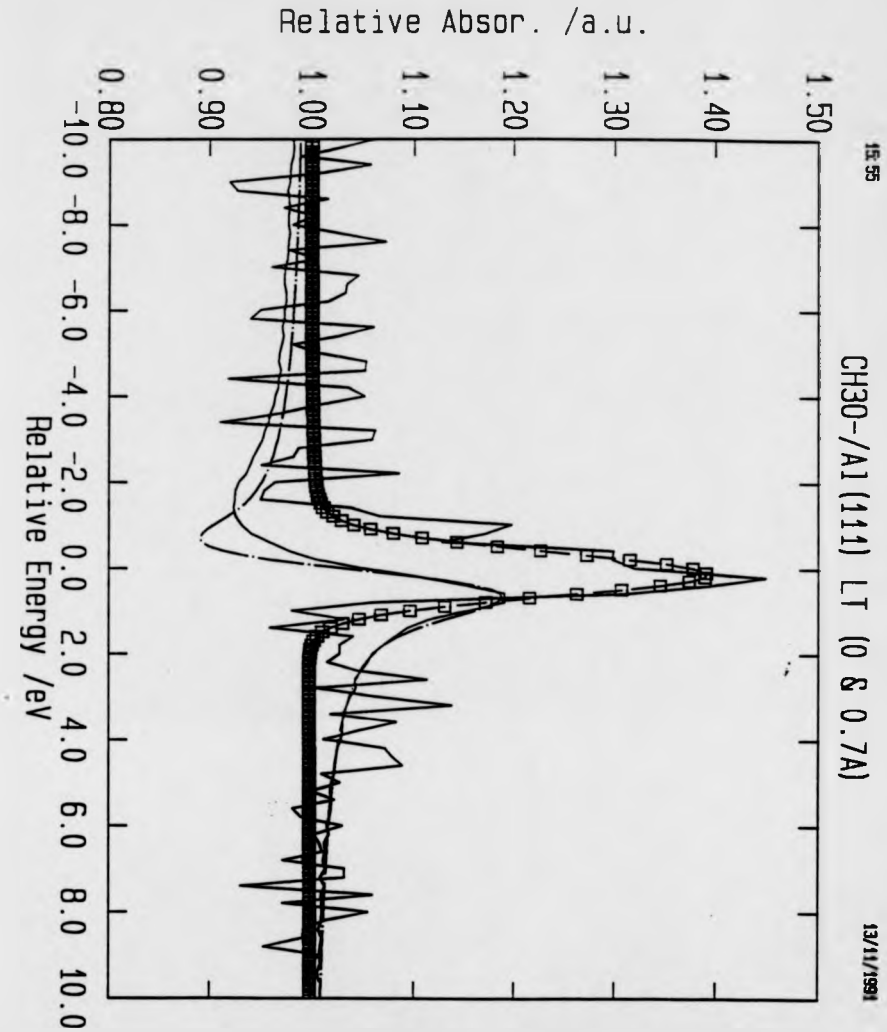

Fig(6.5) : Low temperature experimental NISXW absorption profiles for both Al and O X-ray absorption at the (111) normal incidence Bragg condition, for methoxy (CH_3O-) on Al(111), compared with best fit theoretical curves. The experimental data are shown as full lines joining the data points (the lower noise data being for Al absorption). The theoretical fits to the Al data are shown as dash-dot lines, with the fits to the O data shown as dashed lines joining theoretical data points denoted by empty squares.

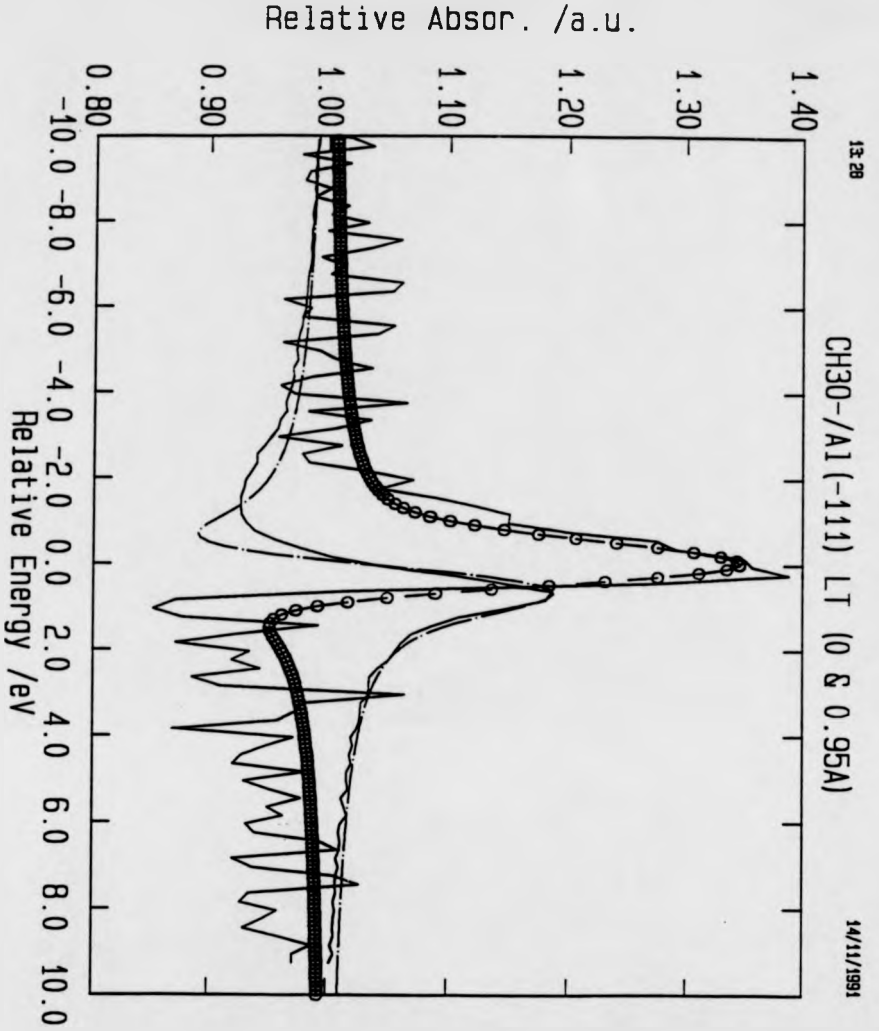

Fig(6.6) : Low temperature experimental NISXW absorption profiles for both Al and O X-ray absorption at the $(\bar{1}11)$ normal incidence Bragg condition, for methoxy (CH_3O-) on Al(111), compared with best fit theoretical curves. The experimental data are shown as full lines joining the data points (the lower noise data being for Al absorption). The theoretical fits to the Al data are shown as dash-dot lines, with the fits to the O data shown as dashed lines joining theoretical data points denoted by empty circles.

At 150 K, the oxygen atom of the methoxy molecule is therefore $0.70 \pm 0.10\dot{A}$ from the Al(111) planes and $0.95 \pm 0.10\dot{A}$ from the Al($\bar{1}11$) planes.

6.4.3.2 Room temperature NISXW results

Following the formation of the methoxy species on the Al(111) surface at 150 K, the crystal was allowed to warm to room temperature. As for the 150 K experiment, Auger electron spectroscopy and LEED were used to check the surface at room temperature prior to, and following, the NISXW data sets.

The process of obtaining absorption profiles for the Al(111) and Al($\bar{1}11$) Bragg plane geometries was then repeated. Table(6.1) shows the fitting parameters for the aluminium absorption profiles (the parameters used to fit the Al absorption profile being unchanged from the (111) Bragg plane fitting).

Fitting Parameter	**(111) Value**	**($\bar{1}11$) Value**
Debye-Waller factor	0.9	0.9
Coherent fraction	0.9	0.9
Gaussian width	0.7eV	0.7eV
Δz	0.75Å	1.00Å

Table 6.3: *Fitting parameters for the O absorption profiles from NISXW measurements of methoxy on Al(111) at room temperature, for both (111) and ($\bar{1}11$) Bragg scattering conditions.*

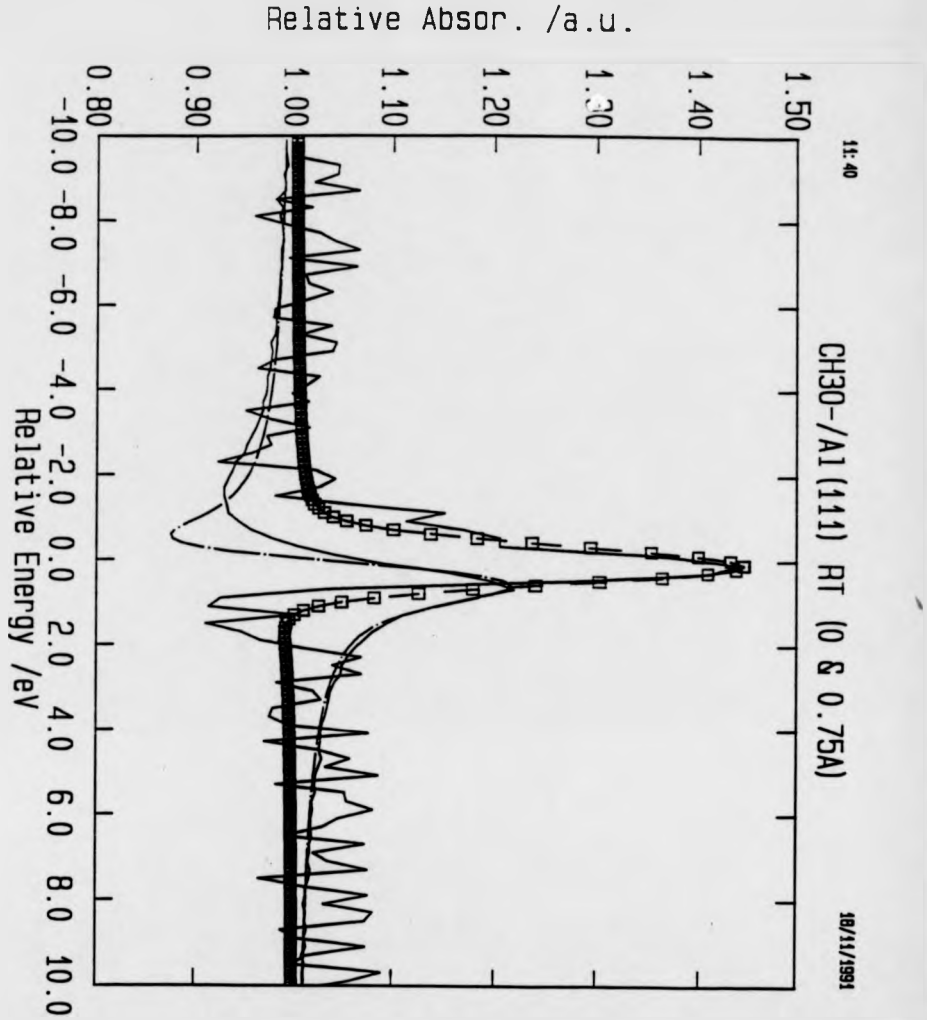

Fig(6.7) : Room temperature experimental NISXW absorption profiles for both Al and O X-ray absorption at the (111) normal incidence Bragg condition, for methoxy (CH_3O-) on Al(111), compared with best fit theoretical curves. The experimental data are shown as full lines joining the data points (the lower noise data being for Al absorption). The theoretical fits to the Al data are shown as dash-dot lines, with the fits to the O data shown as dashed lines joining theoretical data points denoted by empty squares.

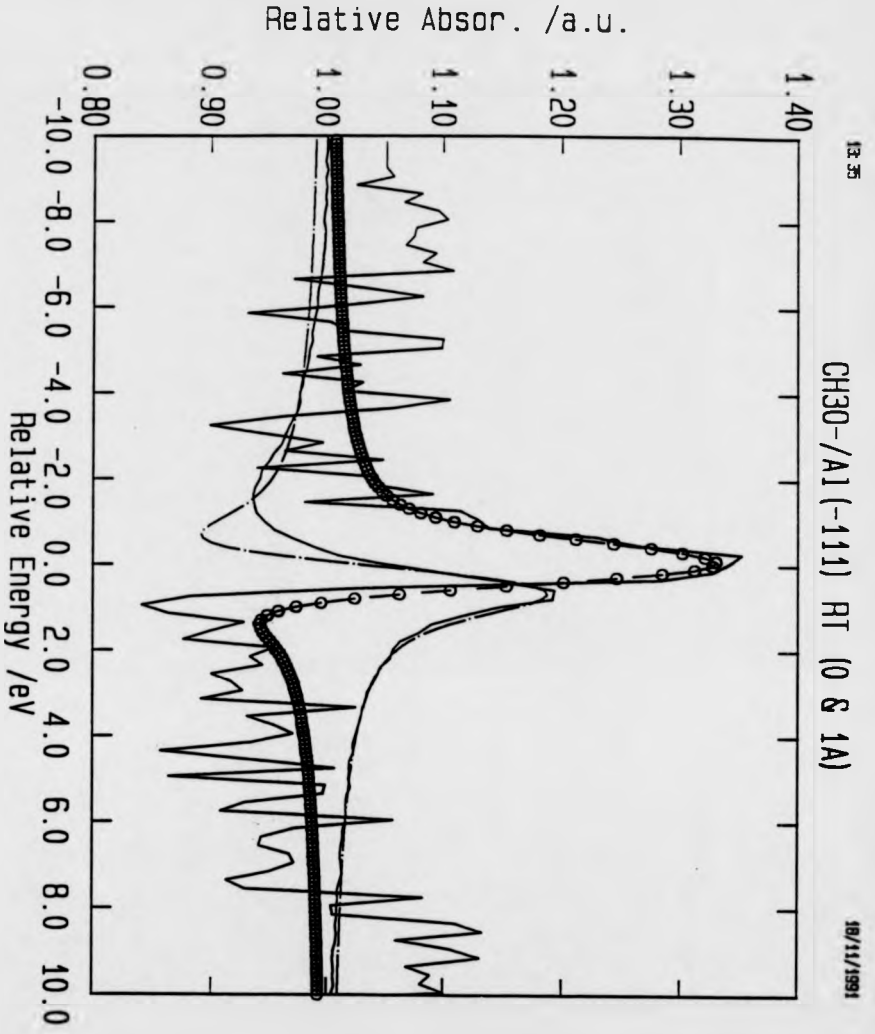

Fig(6.8) : Room temperature experimental NISXW absorption profiles for both Al and O X-ray absorption at the ($\bar{1}11$) normal incidence Bragg condition, for methoxy (CH_3O-) on Al(111), compared with best fit theoretical curves. The experimental data are shown as full lines joining the data points (the lower noise data being for Al absorption). The theoretical fits to the Al data are shown as dash-dot lines, with the fits to the O data shown as dashed lines joining theoretical data points denoted by empty circles.

Table(6.3) shows the parameters used to fit the measured oxygen absorption profiles for both (111) and ($\bar{1}11$) normal incidence Bragg scattering conditions. Fig(6.7) shows the experimental and theoretically fitted absorption profiles following NISXW measurements from the Al(111) Bragg planes. The smooth continuous line and the dash-dot line represent the Al 1s photoemission signal monitored, and theoretically fitted, absorption profiles. The noisy single line and dashed line (joining data points depicted by empty squares) represent the O 1s photoemission signal monitored and theoretically fitted absorption profiles.

Fig(6.8) shows the experimental and theoretically fitted absorption profiles for the Al($\bar{1}11$) Bragg plane geometry (the line types represent the same profiles as in Fig(6.6) except the calculated O absorption points are now denoted by empty circles).

At room temperature, the oxygen atoms were found to be $0.75 \pm 0.10\mathring{A}$ from the Al(111) planes, and a distance of $1.00 \pm 0.10\mathring{A}$ from the ($\bar{1}11$) planes.

6.4.4 Oxygen atom location by triangulation

In all the absorption profile analysis, a high coherent fraction was observed (CF$\approx$ 0.9). This would exclude the possibility of the oxygen (in the CH_3O- molecule) bonding at a low symmetry absorption site. Since the substrate has $3m(C_{3v})$ symmetry, adsorption in any site having a lower symmetry than this (a bridge site for example), would lead to the occupation of several sites, which are inequivalent in their distances to the ($\bar{1}11$) plane; the resulting NISXW profile would then only be generated by fitting more than one layer spacing (or by an average layer spacing

with a low coherent fraction) [31]. As this is not the case, just the three high symmetry adsorption sites (atop, fcc hollow above an Al atom in the third layer, and hcp hollow above an Al atom in the second layer) are considered.

The (111) layer spacing ($\Delta z = 0.70 \pm 0.10\mathring{A}$ low temperature, and $\Delta z = 0.75 \pm 0.10\mathring{A}$ room temperature) is defined in Fig(6.9), and the distance from the ($\bar{1}11$) layer for the three possible sites are calculated by triangulation and shown in Table(6.4).

Site	Distance (Å)
atop	0.23 ± 0.04
fcc hollow	1.79 ± 0.04
hcp hollow	1.01 ± 0.04

Table 6.4: *Calculated distances of three adsorbate sites from ($\bar{1}11$) layer by triangulation using adsorbate to (111) surface distances measured by NISXW at low and room temperature.*

Comparing these values with the experimental values of $0.95 \pm 0.10\mathring{A}$ and $1.00 \pm 0.10\mathring{A}$, it can be clearly seen that the hcp hollow site alone fits well, the other sites being far outside the estimated experimental errors.

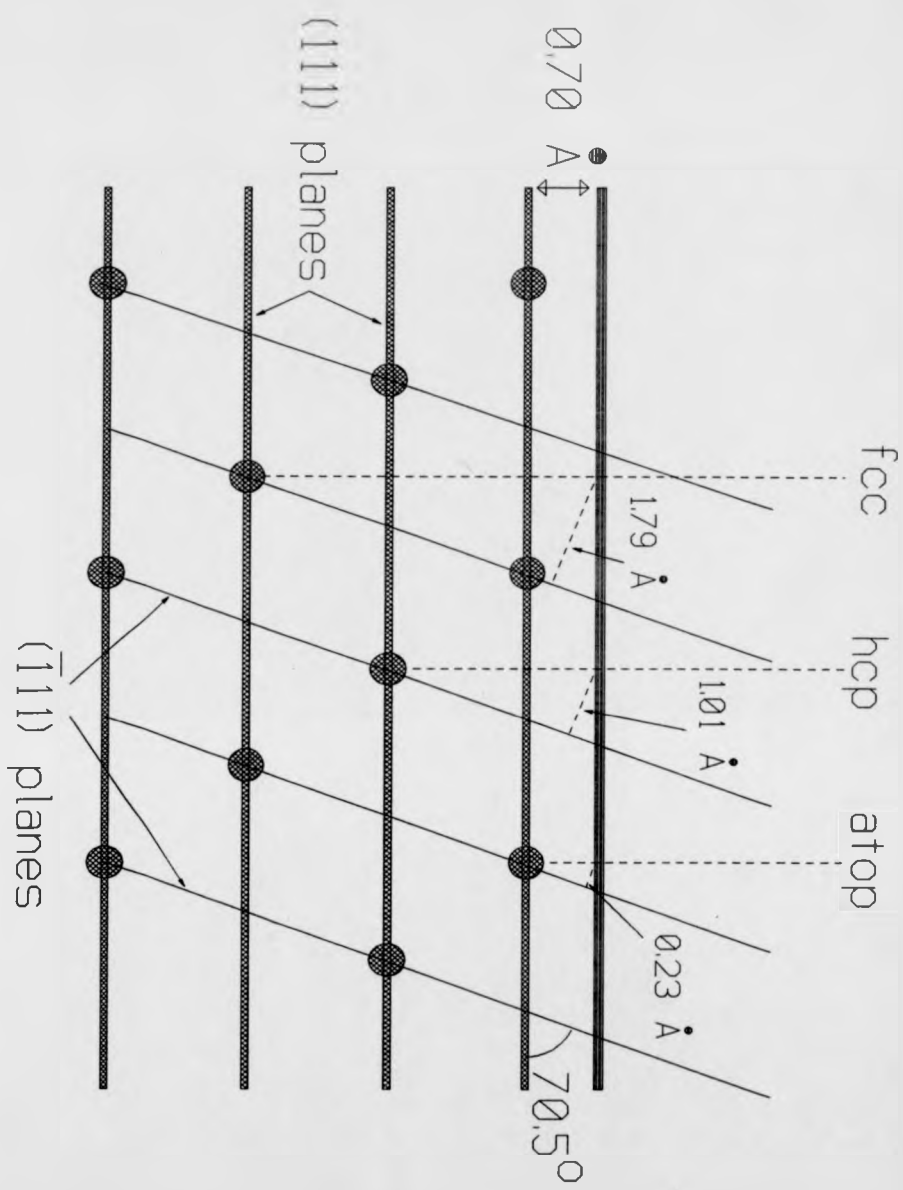

Fig(6.9) : Schematic sectional diagram of Al(111) showing the principle of real-space triangulation of (111) and ($\bar{1}11$) NISXW profiles to determine the absorption site of oxygen. The 0.70$\AA$ (111) layer spacing is shown to be consistant with three different ($\bar{1}11$) spacings for the FCC hollow, HCP hollow and atop sites.

6.4.5 Discussion

The oxidation of aluminium surfaces has been extensively studied (see section(**5.31**) for review), with the Al(111) surface being the one face where a chemisorption phase is clearly identified [32]. For the Al(111)(1×1)O phase. the oxygen atoms have been shown to occupy the fcc hollow sites using NISXW [30] in addition to LEED [33, 34, 35] and SEXAFS [36, 37, 38] measurements, with an O-Al top layer spacing of $\approx 0.70\dot{A}$. By comparing the NISXW results for O-Al(111) system that were aquired previously (using the same experimental set up) by Kerkar *et al* [30] (shown in Fig(6.10)), with the NISXW results obtained for the CH_3O-Al(111) (Figs(6.5-6), it can be seen that the profiles obtained for the (111) reflection are almost identical. The profiles obtained from the $(\bar{1}11)$ reflection are however, quite different. This implies that although the oxygen is at the same distance perpendicular to the surface, there is a difference of adsorption site between the two systems. The Al-O nearest neighbour distances calculated with values from the CH_3O-Al(111) NISXW experiment was found to be $1.79 \pm 0.04\dot{A}$ for the fcc hollow site, in comparison to SEXAFS measurements for the O-Al nearest neighbour bond length that yield $1.79\dot{A}$[37] and $1.76\dot{A}$ [38]. For this comparison, it must be stressed that the two techniques effectively measure different relative distances, with SEXAFS providing a direct measurement of the nearest neighbour distance. The NISXW technique on the other hand measures the relative distance of the adsorbate to the uniform lattice spacing of the bulk, where the standing wave is set up. Any contraction or expansion in the top surface layers will impart a systematic error in the calculated nearest neighbour distance.

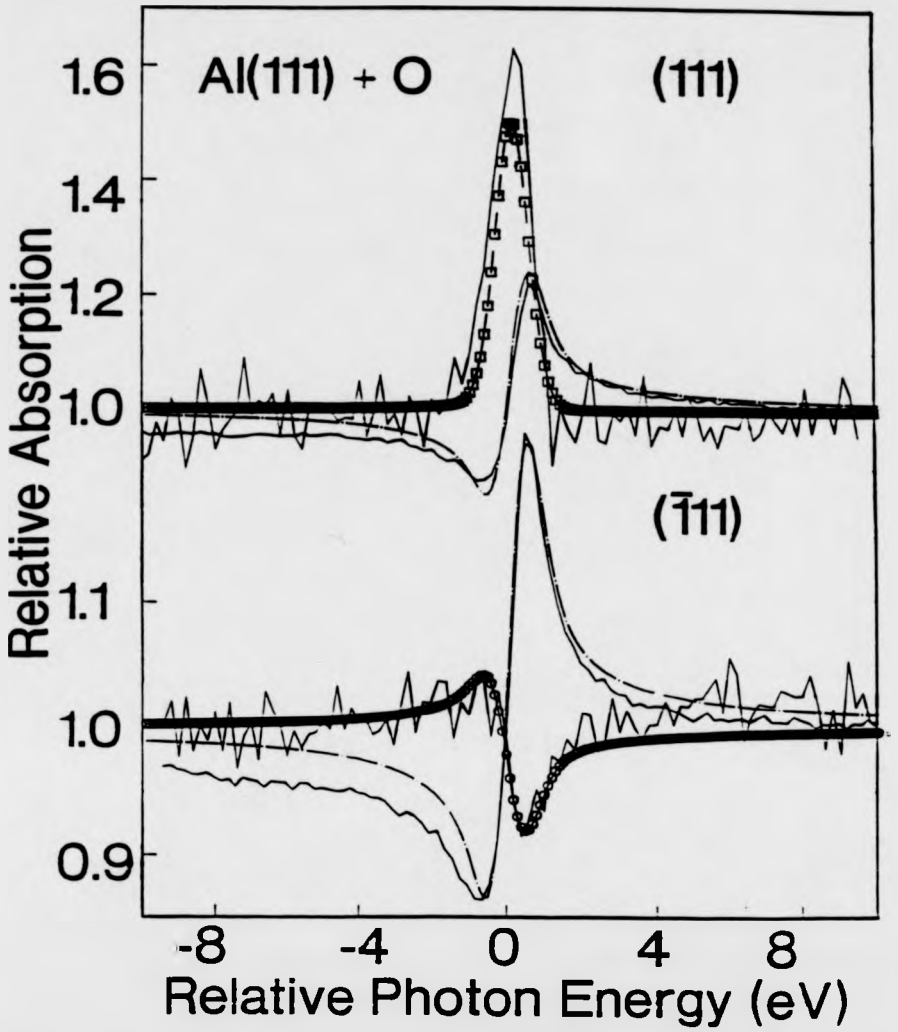

Fig(6.10) : Experimental and theoretical NISXW profiles for chemisorbed oxygen on Al(111)[30] (achieved by a 10L exposure to oxygen gas).The experimental data are shown as full lines joining the data points (the lower noise data being for Al absorption). The theoretical fits to the Al data are shown as dash-dot lines, with the fits to the O data shown as dashed lines joining theoretical data points denoted by empty squares and empty circles for the (111) and ($\bar{1}$11) Bragg conditions respectively.

While taking these factors into account, and comparing the closeness of the NISXW derived and SEXAFS measured distances, it can be assumed that the nearest neighbour distances obtained in this study are unlikely to be in serious error.

From adsorption studies (where an ordered overlayer structure exists) where only one site is occupied, it is generally the fcc hollow site that is prefered: in particular O on Al(111),Ni(111) and Ir(111), S on Ni(111),Rh(111),Pd(111),Ir(111) and Pt(111), Au on Pd(111), ethylidyne on Pt(111)[39], and the methoxy on Cu(111) [40]. In the low coverage regime, there are some adsorption systems (i.e I on Ag(111) [41]) in which both the fcc and hcp sites are occupied on an equal basis. Comparing the Al(111) system with methoxy and chemisorbed oxygen on copper surfaces in particular is of interest, since the Cu(111) surface provides a good comparison to Al(111) due to having a three-fold coordinated hollow adsorption site.

Methoxy and oxygen adsorption studies on copper surfaces using mainly the scanned energy mode photoelectron diffraction technique, have yielded information concerning bond lengths and adsorption sites (mainly for the Cu(100) and Cu(111) surfaces) [40, 42]. For the CH_3O−Cu(100) system, the adsorption site is between the hollow and bridge sites (although closer to the hollow site), with a nearest neighbour distance of $1.97 \pm 0.05\mathring{A}$ from SEXAFS [43] and a slightly larger value of $2.00 \pm 0.05\mathring{A}$ from photoelectron diffraction [42] (which may be longer due to the low symmetry adsorption site causing some coupling of the Cu-O distance and off-hollow distortion parameters in the structure determina-

tion by this method). The Cu-O spacing for O on Cu(100), determined using SEXAFS, has produced a range of values from $1.84\dot{A}$[44] to $1.94\dot{A}$[45] but the layer values may be inaccurate due to adsorbate induced reconstruction, and the Cu-O distance is probably close to or less than the $1.85\dot{A}$ value obtained for the bulk oxide [47, 48]. Studies of methoxy on Cu(111) have concluded that the methoxy adsorbs at the fcc hollow site with a Cu-O nearest neighbour distance of $1.88 \pm 0.05\dot{A}$ [40]. The oxygen on Cu(111) system (where no simple O chemisorption structure is known to exist), has shown (from SEXAFS measurements) a Cu-O nearest neighbour distance of $1.83 \pm 0.02\dot{A}$ [46]. The Cu-O distances in both the methoxy systems (Cu(100) and Cu(111)) are significantly greater than those of either the chemisorbed oxygen or bulk oxide systems. The Cu-O nearest neighbour bond lengths for methoxy and chemisorbed oxygen on copper surfaces are therefore broadly consistant with the behaviour observed for the Al(111) surface, although the actual bonding geometry for the methoxy species is different for the two substrate systems

In general there is no reason to expect that free oxygen atoms and oxygen in the methoxy molecule, should form similar bond lengths to a metal substrate (the comparitive chemistry being quite different). In aluminium oxides, a range of different Al-O nearest neighbour bond lengths are found, which are associated with various oxygen coordinations. For the Al(111)(1×1)O phase, there is a lower coordination number of surface Al atoms (3 compared to a value of 4 to 6 in bulk oxides), and a shorter Al-O distance than the bulk oxide; in this study, the methoxy coverage on Al(111) was less than a monolayer.

Following from the discussion of bondlengths, it is appropriate to discuss the actual bonding sites. The fcc and hcp hollow sites for an *fcc* surface, differ only in their third (or greater) nearest neighbour distances (the hcp site is above a second layer substrate atom, and the fcc above a third layer atom). The difference in binding energies between the two sites is therefore likely to be very small. The occupation of the hcp hollow site by methoxy on Al(111) is quite unique in comparison with most other *fcc*(111) metal adsorption systems; ethylidyne (C_2H_3-) does occupy this site on the Rh(111) surface, but this is thought to be due to site blocking by hydrogen in the fcc hollow sites[50].

One possibility we should consider is that a similar site blocking by hydrogen in the fcc sites is also the cause of the hcp hollow site occupation for methoxy on Al(111). At 143 K, methanol is believed to decompose on Al(111) to form chemisorbed methoxy and atomic hydrogen, with thermal desorption spectra showing the hydrogen desorbed as molecular hydrogen mainly at the decomposition temperature [29]. Although some molecular hydrogen is shown to desorb at higher temperatures in the desorption spectra, it is clear that all such desorption occurs far below room temperature [29]. The methoxy on Al(111) experiment was conducted both at room temperature, and at 150 K, with the same observed structure (i.e methoxy adsorbing at hcp hollow site), so a simple site blocking explanation based on chemisorbed hydrogen appears not to be viable.

Note, incidentally, that the hcp hollow site has a substrate atom directly below in the second layer, and thus offer the possibility of providing a higher coordination than the fcc site. However, for aluminium, the (111) plane spacing is

large, so a higher coordination could only be achieved if the adsorbate penetrated below the top aluminium layer (as is found for the surface oxide phase on Al(111) [30, 38]), but this is not observed.

6.4.6 Conclusions

The adsorption of methoxy (CH_3O-) on Al(111) has been investigated using the NISXW technique, both at low temperature (150 K) and at room temperature. In both instances, the adsorption occured in a three-fold symmetry hollow site with a Al-O layer spacing of $0.70 \pm 0.10\mathring{A}$. The adsorption site was determined using real space triangulation, to be the hcp hollow site above a second layer Al atom, and not the fcc hollow site (above an Al atom in the third layer) that is occupied by chemisorbed oxygen on Al(111). This would appear to be the first example of an adsorbate with a preference for this hcp hollow site on a clean *fcc* (111) surface. The reasons behind this geometry, and the significance of the Al-O bond length is at present unclear. The energetic distinction between the two hollow sites is thought to be quite subtle, and theoretical calculations are needed for a better understanding of this system.

References

[1] B.W.Batterman, Phys. Rev. **133**, A759 (1964)

[2] B.W.Batterman, Phys. Rev. Letts. **22**, p703 (1969)

[3] P.L.Cowan, J.A.Golovchenko, M.F.Robbins, Phys. Rev. Letts. **44**, p1680 (1980)

[4] J.R.Patel, J.A.Golovchenko, P.E.Freeland, H.-J.Gossman, Phys. Rev. **B36**, p7715 (1987)

[5] J.E.Golovchenko, B.W.Batterman and W.L.Brown, Phys. Rev. **B10**(10), p4239 (1974)

[6] P.L.Cowan, J.A.Golovchenko and M.F.Robbins, Phys. Rev. Letts. **44**(25), p1680 (1980)

[7] J.A.Golovchenko, J.R.Patel, D.R.Kaplan, P.L.Cowan and M.J.Bedzyk, Phys. Rev. Letts. **49**(8), p560 (1982)

[8] M.Bedzyk and G.Materlik, Surf. Sci. **152/153**, p10 (1985)

[9] N.Hertel, G.Materlik and J.Zegenhagen, Z. Phys. B :Cond. Matter **58**, p199 (1985)

[10] M.J.Bedzyk and G.Materlik, Phys. Rev. **B31** (6), p4110 (1985)

[11] S.M.Durbin, L.E.Berman, B.W.Batterman and J.M.Blakely, J. Vac. Sci. Technol. **A3**(3), p973 (1985)

[12] P.Funke and G.E.Materlik, Sol. St. Commun. **54**(11), p11 (1985)

[13] G.Materlik, Z. Phys. B :Cond. Matter **61**, p405 (1985)

[14] B.N.Dev, G.Materlik, R.L.Johnson, W.Kranz and P.Funke. Surf. Sci. **178**, p1 (1986)

[15] T.Ohta, H.Sekiyama, Y.Kitajima, H.Kuroda, T.Takahashi and S.Kikuta, Japan J. Applied Phys. **24**, pL475 (1985)

[16] T.Ohta, Y.Kitajima, H.Kuroda, T.Takahashi and S.Kikuta, Nucl. Inst. Meths. **A246**, p760 (1986)

[17] D.P.Woodruff, D.L.Seymour, C.F.McConville, C.E.Riley, M.D.Crapper and N.P.Prince, Phys. Rev. Letts. **58**(14), p1460 (1987)

[18] D.P.Woodruff, D.L.Seymour, C.F.McConville, C.E.Riley, M.D.Crapper and N.P.Prince, Surf. Sci. **195**, p237 (1988)

[19] C.Malgrange and D.Ferret, Nucl. Inst. Meths. **A314**, p285 (1992)

[20] R.W.James, *The Optical Principles of X-Ray Diffraction*, (Bell, London. 1962)

[21] W.Graeff and G.Materlik, Nucl. Inst. Meths. **195**, p97 (1982)

[22] G.Materlik, A.Frahm and M.J.Bedzyk. Phys. Rev. Letts. **52**(6), p441 (1984)

[23] L.E.Berman, B.W.Batterman and J.M.Blakely, Phys. Rev. **B38**(8), p5397 (1988)

[24] J.W.Rogers Jr., R.L.Hance and J.M.White, Surf. Sci. **100**, p388 (1980)

[25] K.Klier, Adv. Catal. **31**, p243 (1982)

[26] J.W.Rogers Jr. and J.M.White, J. Vac. Sci. Technol. **16**,p485 (1979)

[27] I.F.Tindall and J.W.Vickerman, Surf. Sci. **149**, p577 (1985)

[28] G.D.Waddi and L.L.Kesmodel, Surf. Sci. **182**, pL248 (1987)

[29] J.G.Chen, P.Basu, L.Ng and J.T.Yates Jr., Surf. Sci. **194**, p397 (1988)

[30] M.Kerkar, D.Fisher, D.P.Woodruff and B.Cowie, Surf. Sci. **271**(1-2), p45 (1992)

[31] M.Kerkar, A.B.Hayden, D.P.Woodruff, M.Kadodwala and R.G.Jones, J. Phys.: Condens. Matter **4**, p5043 (1992)

[32] C.F.McConville, D.L.Seymour, D.P.Woodruff and S.Bao, Surf. Sci. **188**, p1 (1987)

[33] F.Jona and P.M.Marcus, J. Phys. C **13**, pL477 (1980)

[34] F.Soria, V.Martinez, M.C.Muñoz and J.L.Sacedon, Phys. Rev. **B 24**, p6926 (1981)

[35] J.Neve, J.Rundgren and P.Westrin, J. Phys. C **15**, p4391 (1982)

[36] L.I.Johansson and J.Stöhr, Phys. Rev. Letts. **43**, p1882 (1979)

[37] J.Stöhr, L.I.Johansson, S.Brennan, M.Hecht and J.N.Miller, Phys. Rev. **B22**, p4052 (1980)

[38] D.Norman, S.Brennan, R.Jaeger and J.Stöhr, Surf. Sci. **105**, pL295 (1981)

[39] J.M.MacLaren, J.B.Pendry, P.J.Rous, D.K.Saldin, G.A.Somorjai, M.A.Van Hove and D.D.Vvedensky, *Surface crystollagraphic information service: A Handbook of Surface Structures* (Dordrecht: Reidel) (1987)

[40] D.Ricken, P.Gardner, A.W.Robinson, J.S.Somers, K.M.Schindler, A.M.Bradshaw, M.C.Asensio, A.L.D.Kilcoyne and D.P.Woodruff, Surf. Sci. submitted (1992)

[41] H.H.Farrell, M.M.Traum, N.V.Smith, W.A.Royer, D.P.Woodruff and P.D.Johnson, Surf. Sci. **102**, p527 (1981)

[42] Th.Lindner, J.Somers, A.M.Bradshaw, A.L.D.Kilcoyne, and D.P.Woodruff, Surf. Sci. **203**, p333 (1988)

[43] D.A.Outka, R.J.Madix and J.Stöhr, Surf. Sci. **164**, p235 (1985)

[44] U.Döbler, *Doctoral Thesis*, Freien Universität, Berlin. (1986)

[45] U.Döbler, K.Baberschke, J.Stöhr and D.Outka, Phys. Rev. **B31**, p2532 (1985)

[46] J.Haase and H@.-J.Kuhr, Surf. Sci. **203**, pL695 (1988)

[47] H.C.Zeng, R.A.McFarlane, R.N.S.Sodhi and K.A.R.Mitchell, Surf. Sci. **208**, pL7 (1989)

[48] M.C.Asensio, M.J.Ashwin, A.L.D.Kilcoyne, D.P.Woodruff, A.W.Robinson, Th.Lindner, J.S.Somers, D.E.Ricken and A.M.Bradshaw, Surf. Sci. **236**, p1 (1990)

[49] P.S.Bagus, C.R.Brundle, F.Illas, F.Parmigiani and G.Pozonetti, Phys. Rev. **B44**, p9025 (1991)

[50] R.J.Koestner, M.A.Van Hove and G.A.Somorjai, Surf. Sci. **121** p321 (1982)

Chapter 7

Summary and conclusions

The aim of this work has been to investigate the electronic and structural properties of adsorbates on nickel and aluminium surfaces, demonstrating the close relationship of structural and electronic behaviour in surface effects. In this final chapter the results and conclusions of the experimental work presented are summarised with some discussion in light of some very recent publications.

In Chapter 4, k-resolved inverse photoemission spectroscopy (KRIPES) has been applied to studying clean Ni(100) and the C, N and O half-monolayer adsorption systems. For the clean Ni(100) surface the results were found to be in agreement with earlier studies, although no evidence was found for the existence of a surface resonance state previously reported to be at the same energy (in $9.7eV$ isochromats) as a direct transition to the bulk s-p band [3]. Similarly, the previous observation of an increase in intensity just above the Fermi level (corresponding to the d-band related peak) following oxygen adsorption that was assigned to an oxygen induced state [1, 2] was not observed in this study. This intensity was observed to decrease with oxygen adsorption in agreement with other studies. For all three half-monolayer adsorption phases, KRIPES showed the existence of adsorbate-induced antibonding states. The C and N-induced states were shown to have a flat dispersion in energy with varying $k_{||}$, while the O-induced state showed a strong dispersion. The different character of these states are explained as being due to the p-states of the C and N interacting mainly with the Ni d-band (changes in the occupied d-band for these systems having previously been observed using photoemission), and the p-states of the O interacting principally with the Ni s-p band. Considering the strong reconstructions induced by the C

and N compared to the overlayer structure formed by O, these possible preferences for interaction may be seen as a 'fingerprint' of the different reconstructions. There are several experiments that would be of interest following the KRIPES studies of the three adsorption systems and which could not be conducted here due to geometrical limitations of the KRIPES system. By using a combination of channel plate detectors (with appropriate filters) arranged perpendicular and parallel to the sample surface, information on the symmetry of the unoccupied states could be obtained. This would be of value in further investigating the Ni(100)(2 × 2)-N ($p4g$) structure where some polarisation sensitivity of the N-induced state was observed. An investigation of the Ni(100)$c(2\times2)$-O adsorption structure using higher isochromat energies (in our case limited by the cut-off frequency of the LiF lens) would be beneficial in separating better the s-p band and O-induced antibonding state contributions observable in this study. A KRIPES study of the graphitic phase on Ni(100) would also be of interest in light of ARUPS results which show a rigid shift of the graphitic bands by up to $1.5eV$ relative to those of bulk graphite [4].

The strong promoting effect of alkali metals on metal oxidation has been investigated in Chapter 5 by a core-level photoemission study of the sodium promoted oxidation of Al(111). Core-level photoemission measurements of the influence of submonolayer coverages of Na on Al(111) on the uptake of oxygen by this surface show a strong promotion of both oxygen dissociation and the formation of the surface oxide. The Al(2p) spectra indicate the loss of intermediate chemically shifted states characteristic of a chemisorbed precursor to oxidation; the Na(2p)

spectra however, indicate that such a state is still present but the bonding of the surface oxygen is now strongly localised to the Na atoms. The results of this investigation have been discussed in relation to recent structural information on the adsorption site of sodium on Al(111). The role of the Na atoms in the promotion is found to be local, with the increased oxidation rate resulting from a more rapid filling of the precursor state by enhanced oxygen dissociation rates. There is some evidence that the final oxide state involves the intermixing of Al and Na metal atoms. Recent photoemission measurements (obtained with a better resolution than used in this study) on the oxidation of Al(111) have implied that there is a fourth intermediate chemically shifted state (in addition to the previously observed three), and this has been attributed to Al atoms at the interface of the multilayer oxide that are not directly involved with the oxygen bonding [5]. This new result does not affect the conclusions of this study, although a further study of the sodium promoted oxidation of Al(111) at this resolution would be of interest especially for the investigation of the intermixing of Al and Na metal atoms in the final oxide state.

Chapter 6 presented results of a normal incidence standing X-ray wave study to determine the adsorption site for methoxy on Al(111). By recording the X-ray absorption in the O atom of the methoxy species at both the (111) and ($\bar{1}11$) normal incidence Bragg scattering conditions (at normal and 70.5° to the surface), the adsorption site was obtained by the process of real space trianguation. The species was found to adsorb in a three-fold symmetric hollow site with an O-Al layer spacing of 0.70 ± 0.10Å, (as found for oxygen in a previous NISXW study

References

[1] H.Scheidt, M.Glöbl and V.Dose, Surf. Sci. Lett. **123**, pL728 (1982)

[2] V.Dose, M.Glöbl and H.Scheidt, J. Vac. Sci. Technol. **A1**(2), p1115 (1983)

[3] L.E.Klebanoff, R.K.Jones, D.T.Pierce and R.J.Celotta, Phys. Rev. **B36**(15), p7849 (1987)

[4] C.F.McConville, D.P.Woodruff and S.D.Kevan, Surf. Sci. Letts. **171**, pL477 (1986)

[5] C.Berg, S.Raaen, A.Borg, J.N.Anderson, E.Lundgren and R.Nyholm, Phys. Rev. **B47**(19), p13063 (1993)

[6] M.Kerkar, D.Fisher, D.P.Woodruff and B.Cowie, Surf. Sci. **271**(1-2), p45 (1992)